Synthesis of Large-Grained Polycrystalline Silicon by Hot-Wire Chemical Vapor Deposition for Thin Film Photovoltaic Applications

Thesis by

Maribeth Swiatek Mason

In Partial Fulfillment of the Requirements
for the Degree of
Doctor of Philosophy

California Institute of Technology
Pasadena, California

2004
(Submitted January 14, 2004)

© 2004
Maribeth Swiatek Mason
All Rights Reserved

Acknowledgements

After a number of misadventures, I've finally been tapped by the Blue Fairy to become a Real Scientist. My success in this endeavor is largely a result of being lucky enough to meet the right people, each of whom gave me something useful to help me along the journey. I hope that I have given each of them something useful in return.

For direct contributions to the content of this thesis, I am grateful to Carol Garland, a model of true kindness and patience, who helped perform TEM analysis; Dick Ahrenkiel, who performed RCPCD lifetime measurements; Eric Schiff and Steluta Dinca, who performed time-of-flight mobility measurements; Matt Dicken, who performed RHEED measurements; John Venables, with whom I engaged in valuable discussions of nucleation kinetics; and Richard Mason, who helped with MATLAB and Mathematica syntax.

A fortuitous choice of desk in 1997 gave me the Best Officemates Ever, who shared in the joys of Good Science Days and made even the worst of Bad Science Days a little brighter. Many thanks to Julie Biteen, who mailed my samples, checked out library books for me, and provided wise advice on grammar and everything else; Luke Sweatlock, who crimped, hammered and tightened most of the parts on the HWCVD reactor and gave me a good reason to take up the piano again; Christine Richardson, who provided SNSPE templates and introduced me to the joys of Paradise Hotel; Claudine Chen, who taught me the art of TEM and SNSPE and generously gave good counsel and true friendship; Jason Holt, who made it almost as much fun to build that wretched manipulator as it was to spend the generous Denver-area per diem; and Jimmy Zahler (who really should just move in to 244 for all the time he spends gossiping in there), who helped me "change the tone" when science made me grumpy.

I am privileged to have been a member of the Atwater group, who continually gave me support, fun and friendship. For this I thank (in no particular order) Julie Casperson, Tao Feng, Pieter Kik, Mark Brongersma, Albert Polman, David Boyd, Robb Walters, Jen Ruglovsky, Rhett Brewer, Stefan Maier, Kyu Min, Liz Boer, Regina Ragan, Cecily Ryan, Matt Norman, Anna Fontcuberta i Morral, John Hartman, Torsten Bistritschan, Brendan Kayes, Young-Bae Park, Aditi Risbud, Katsu Tanabe, Beth Lachut and Jen Dionne.

Throughout my studies I was fortunate to find the best of mentors. Each of them had so many

good qualities which I wish to emulate in my career, and I hope to honor them with my future success. Many years ago, Mark Kirk told me I would make a good scientist, which still keeps me going when things seem impossible. John Abelson's ongoing help, kindness and encouragement have been priceless; it's thanks to his efforts I began this at all. Finally, I have been inspired by the creative vision of Harry Atwater. I will always be thankful that he did not make me move to Harvard, and more importantly, that he never gave up on me even through my worst failures.

I am of course forever grateful to my family, who trusted me to seek my fortune in California and always said they would still love me even if I quit my Ph.D. Finally, thanks to my dearest love, Richard, who from the beginning carried me, sometimes kicking and screaming, through this experience. He's right, as usual – I'm happy I found the strength to finish this, and I hope I've made him proud.

Abstract

In this study, we investigate the fabrication of large-grained polycrystalline silicon by hot-wire chemical vapor deposition (HWCVD) and its suitability for thin-film photovoltaic applications. We have devised two strategies for the fast, low-temperature growth of thin polycrystalline silicon films on glass substrates. The first is the direct growth of polycrystalline silicon on SiO_2 by HWCVD. We use atomic force microscopy (AFM) to characterize fully continuous polycrystalline silicon films grown by HWCVD on SiO_2, as well as the nucleation density of silicon islands formed in the early stages of HWCVD growth, as a function of temperature and hydrogen dilution (H_2:SiH_4). Our observations of the nucleation kinetics of Si on SiO_2 can be explained by a rate-equation pair-binding model, from which we derive an estimate for the prefactor and activation energy for surface diffusion of Si on SiO_2 during HWCVD growth and assess the viability of this method for the rapid growth of large-grained polycrystalline silicon on SiO_2.

The second strategy uses large-grained ($\sim$100 μm) polycrystalline silicon layers fabricated by selective nucleation and solid-phase epitaxy (SNSPE) on SiO_2 substrates as templates for epitaxial growth by HWCVD. Using reflection high-energy electron diffraction (RHEED) and transmission electron microscopy (TEM), we have derived a phase diagram for Si on Si(100) consisting of epitaxial, twinned epitaxial, mixed epitaxial/polycrystalline, and polycrystalline phases of growth on Si(100) in the 50 nm–2 μm thickness regime. Evidence is also presented for epitaxial growth on SNSPE templates, which use nickel nanoparticles as nucleation sites for the solid-phase crystallization of phosphorus-doped amorphous silicon on SiO_2. Minority carrier lifetimes for films on Si(100), as measured by resonant-coupled photoconductive decay experiments, range from 5.7 to 14.8 μs while those for films on SNSPE templates range from 5.9 to 19.3 μs. Residual nickel present in the SNSPE templates does not significantly affect the lifetime of films grown on SNSPE templates, making the growth of epitaxial layers by HWCVD on SNSPE templates a possible strategy for the fabrication of thin-film photovoltaics.

Contents

Acknowledgements **iii**

Abstract **v**

1 Introduction **1**

1.1 Photovoltaics as a renewable energy source 1

1.2 Photovoltaics past 1

1.3 Photovoltaics present—current technology 3

1.3.1 Device operation 3

1.3.2 Materials for photovoltaics 3

1.3.3 Crystalline silicon technologies 4

1.4 Photovoltaics future—thin-film polycrystalline silicon? 5

2 Hot-Wire Chemical Vapor Deposition **7**

2.1 Advantages for thin-film photovoltaics 7

2.2 Development of HWCVD 8

2.3 Recent work in HWCVD 9

2.4 Thin-film HWCVD-deposited solar cells 10

2.5 Outline of the thesis 10

3 Nucleation on SiO_2 **11**

3.1 Introduction 12

3.2 Experiment 12

3.3 Quantitative modelling 16

3.4 Microstructural control 20

3.5 Conclusions 21

4 Epitaxial Growth by HWCVD **23**

4.1 Introduction 23

4.2 Low-temperature epitaxy 24

4.3 Epitaxy on Si (100) . . . 24
4.3.1 Initial experiments . . . 24
4.3.1.1 Growth conditions . . . 24
4.3.1.2 Results . . . 25
4.3.2 Further experiments . . . 27
4.3.2.1 Growth conditions . . . 27
4.3.2.2 Results . . . 28
4.3.3 Discussion . . . 33
4.4 Epitaxy on large-grained polycrystalline templates . . . 40
4.4.1 Selective nucleation and solid phase epitaxy . . . 40
4.4.2 Results . . . 42
4.5 Conclusions . . . 43

5 Minority Carrier Lifetimes of HWCVD Films 46
5.1 Introduction . . . 46
5.2 Recombination in semiconductors . . . 47
5.3 Resonant-coupled photoconductive decay . . . 48
5.4 Experiment . . . 49
5.5 Results . . . 51
5.6 Conclusions . . . 54

6 Conclusions and Future Work 56

Bibliography 58

A The HWCVD Reactor 64

B Nucleation Model Code 68

C Hydrogen Surface Coverage Model Code 72

List of Figures

1.1 (a) Energy spectrum of solar radiation. The large absorption peaks are due mainly to water and CO2 in the atmosphere. (b) Ideal cell efficiency as a function of band gap energy, assuming no losses. The band gaps of several semiconductors used in photovoltaics are labeled. [1] . . . 4

2.1 Schematic of the HWCVD process. . . . 8

2.2 Number of papers on HWCVD published since its introduction in 1979. Matsumura resurrected the technique in 1986. The First International Conference on Cat-CVD (Hot-Wire CVD) was held in 2000, with the Second International Conference following in 2002. . . . 9

3.1 Schematic of hot-wire CVD experiments. . . . 13

3.2 Net deposition rate and SiH_4 mole fraction as a function of H_2 partial pressure in 100 mTorr of dilute SiH_4 1% in He. . . . 14

3.3 (a)AFM of the HWCVD nucleation phase. This image was taken after a growth time of 90 seconds at 20:1 H_2 dilution. Bright features are ≥35 nm in height. (b) Post-coalescence 1 μm^2 image of a continuous poly-Si film grown at zero H_2 dilution; grain size is 40 nm. (c) Post-coalescence 1 μm^2 image of a continuous poly-Si film grown at 20:1 H_2 dilution; grain size is 85 nm. . . . 15

3.4 Nucleation data as a function of H_2 dilution at 300° C. The lines are a guide to the eye. 15

3.5 Temperature-dependent nucleation measurements. The lines are a guide to the eye. The initial slope of the data were used to estimate the activation energy for surface diffusion of Si on SiO_2. . . . 16

3.6 Comparison of simulated (lines) and experimental (dots) temperature-dependent cluster density measurements. . . . 18

3.7 Comparison of simulated and experimental H_2 dilution-dependent cluster density measurements at (a) 300°C and (b) 400°C. . . . 19

3.8 Adatom stay time as a function of H_2 dilution. . . . 19

3.9 Two-stage growth experiment, as compared to undiluted growth and growth at 60:1 H_2. The lines which fit the data at 0 H_2 and 60:1 H_2 are guides to the eye. 20

3.10 Pair-binding model simulations of growth at 60:1 H_2 dilution, two-stage growth, and ramped dilution. 21

4.1 Cross-sectional TEM of HWCVD-grown Si on Si (100) at 300°C. The epitaxial films display a periodic array of stacking faults. 25

4.2 (a) Cross-sectional TEM of HWCVD-grown Si on Si (100) at 300°C. The films become highly twinned after a thickness of approximately 240 nm. Labels b, c, and d refer to areas from which selected-area diffraction patterns were obtained. (b) Selected area diffraction from HWCVD film and amorphous glue layer. (c) Selected area diffraction from HWCVD film and Si (100) substrate. (d) Selected area diffraction from Si (100) substrate. Higher-order spots in (b) and (c) are due to the periodic array of stacking faults in the epitaxial film and twinning in the uppermost regions of the film. 26

4.3 Cross-sectional TEM of HWCVD-grown Si on Si (100) at 400C°, which displays mixed epitaxial/polycrystalline growth. Hydrogen-induced defects are present in the substrate. 27

4.4 Cross-sectional TEM of 350 nm-thick film grown at 300°C. (a) 50 nm-thick epitaxial layer before twinned growth begins. Inset: diffraction pattern from twinned region; (b) Twinning continues throughout film growth. 29

4.5 Cross-sectional TEM of 15 μm thick film grown at 300°C. (a) Stacking faults and twinning begin at interface. (b) Mixed twinned epitaxial/polycrystalline growth; twinned regions extend as far as 300 nm into film. (c) Grain size of polycrystalline film is on the order of 1 μm. 30

4.6 RHEED patterns of films of increasing thickness grown at 300°C. The beam is along the <110> direction. Two phases of growth are observed: twinned epitaxial growth [a-g] and polycrystalline growth [h]. 31

4.7 4x4 μm AFM topography (top panels) and error mode (bottom panels) images of films of increasing thickness grown at 300°C. 32

4.8 Phases of crystalline growth observable by RHEED. (a) 300°C, 60 nm thick twinned epitaxial film. (b) 300°C, 330 nm thick twinned epitaxial film; increased surface roughness is responsible for the differences from (a). (c) 475°C, 60 nm thick film of mixed phase; both spots (corresponding to twinned epitaxial growth) and rings (corresponding to polycrystalline growth) are evident. (d) 475°C, 330 nm thick polycrystalline film. 33

4.9 Phase diagram of HWCVD films grown at 50:1 hydrogen dilution. 34

4.10 Calculated equilibrium surface hydrogen coverages for HWCVD growth conditions (H_2:SiH_4=50:1, 25 mTorr 4% SiH_4 in He, wire 2.5 cm from substrate), with experimental temperature-programmed desorption data [2] for comparison. The shaded area represents the temperature regime in which HWCVD growth experiments were performed. . . . 37

4.11 Silicon to oxygen ratio in the first monolayer of growth as a function of dilution ratio R (H_2/SiH_4 at temperatures from 571 to 711 K. Pressure is held constant at 75 mTorr of a gas mixture of H_2 and 4% SiH_4 in He. . . . 39

4.12 Carbon, hydrogen, and oxygen concentrations in 2.2 μm thick film grown at 300°C, as determined by SIMS analysis. . . . 40

4.13 The SNSPE template fabrication process. . . . 41

4.14 Crystallization of SNSPE template layer [3]. The black dots are the nickel nanoparticles; the white areas are grains of crystalline silicon and the grey areas are amorphous silicon regions. . . . 41

4.15 Plan-view TEM of HWCVD epitaxial film (T=300°C) on SNSPE template. (a) Selected area diffraction pattern from underlying SNSPE template. (b) Selected area diffraction pattern from HWCVD film on SNSPE template. (c) Bright-field image indicating selected area diffraction regions. Inset: diffraction from entire area. . . . 42

4.16 (a) Bright-field image of HWCVD film (T=300°C) on SNSPE template showing selected area diffraction regions. (b) Selected area diffraction from HWCVD film on (100)-oriented grain. (c) Selected area diffraction from HWCVD film on a grain of different orientation. . . . 43

4.17 (a) Bright-field image of HWCVD film (T=300°C) on SNSPE template showing selected area diffraction region. Inset: selected area diffraction pattern showing areas of large-grained polcrystalline growth. (b) Dark-field image corresponding to region in (a). (c) Bright-field image of 3.5 μm thick film with high intragranular defect density. (d) Dark-field image corresponding to region in (b). . . . 44

5.1 Basic schematic of the RCPCD apparatus. . . . 50

5.2 W concentration, as determined by SIMS analysis, in 300°C HWCVD silicon films grown on Si(100) at wire temperatures of 1800°C and 1750°C. The higher W concentration at the surface of both films is due to exposure to the W wire before growth, which was necessary to heat the samples to 300°C. . . . 51

5.3 RCPCD voltage vs. time curves for HWCVD films of various thicknesses on Si(100). (a) 1.5 μm, (b) 3.5 μm, (c) 11.5 μm, (d) 15 μm. Straight lines indicate exponential decay fits to the data. . . . 52

5.4 RCPCD voltage vs time curves for HWCVD films of various thicknesses on SNSPE templates. (a) 1.5 μm, (b) 3.5 μm, (c) 11.5 μm, (d) 15 μm. Straight lines indicate exponential decay fits to the data. 53

5.5 LLI and HLI minority carrier lifetimes of HWCVD films on Si(100) as measured by RCPCD. The dashed and dotted lines represent the LLI and HLI lifetimes, respectively, of the bulk Si(100) substrate. 54

5.6 LLI and HLI minority carrier lifetimes of HWCVD films on SNSPE templates as measured by RCPCD. 55

A.1 Schematic of the HWCVD reactor. 65

A.2 Photographs of the HWCVD reactor. (a) Front view. (b) Side view. 66

A.3 Top view of the inside of the HWCVD reactor. The wire is on and is normal to the plane of the photograph. 67

A.4 Schematic of the inside of the HWCVD reactor during growth experiments. 67

List of Tables

3.1 Coalescence times and grain densities of continuous films under various H_2 dilution conditions, as predicted by the pair-binding model. 21

4.1 Parameters used in hydrogen surface coverage model. 36

5.1 Reported electrical properties of intrinsic films. 47

Chapter 1

Introduction

1.1 Photovoltaics as a renewable energy source

The increasing costs of oil and natural gas and their dwindling supplies as world demand continues to increase, as well as concerns over CO_2 emissions and global warming, have led to increased efforts in the development of renewable energy sources. One of the most promising techniques is the direct conversion of solar energy into electricity through photovoltaic devices. Given a global average solar irradiation of 1700 kWh/m^2/yr, solar energy is capable of producing 3×10^{24} J of energy each year [4]. By comparison, the global energy demand in the year 2000 was approximately 4×10^{20} J [5], making it possible that, along with other alternative energy sources such as wind power and geothermal energy, photovoltaics could be a solution to the energy crisis created by the eventual depletion of fossil fuel reserves.

1.2 Photovoltaics past

The development of photovoltaics began in 1839, when Edmund Becquerel discovered that the current through an electrolytic cell increased when exposed to light [6]. This result, along with Willoughby Smith's 1873 discovery of the photoconductivity of selenium, led to the first photovoltaic cell, fabricated by W. G. Adams and R. E. Day in 1877 [7]. Werner von Siemens called the discovery "scientifically of the most far-reaching importance [8]," although these selenium cells converted only one-tenth of one percent of the incident light into electricity.

It would be more than 75 years before Bell Laboratories scientist Gerald Pearson, while researching doping effects in silicon for electronics applications, accidentally fabricated a solar cell far more efficient than the early selenium cells. In the spring of 1953, Pearson and his colleagues, Daryl Chapin and Calvin Fuller, fabricated the first solar cell efficient enough to run electrical equipment [9]—a discovery praised by the *New York Times* as "the beginning of a new era, leading eventually to the realization of harnessing the almost limitless energy of the sun for the uses of civilization [10]."

Although *U.S. News and World Report* speculated that the silicon solar cells discovered at Bell Laboratories would "provide more power than all the world's coal, oil and uranium [11]," no applications of commercial significance immediately came to light. In fact, Chapin calculated that with a one-watt cell costing $286 a homeowner would have to pay $1,430,000 for an array of sufficient size to power the average American house. Solar cells doubled in efficiency in the ensuing eighteen months, but companies such as Hoffmann Electronics, still desperate to find commercial outlets for solar cells, only found them useful for powering toy boats and radios. However, Chapin's colleague, Gordon Raisbeck, was optimistic about the future of photovoltaics, speculating in 1955 that the new devices would first find use where power is needed "in inaccessible places where no lines go" and "in doing jobs the need for which we have not yet felt [12]."

Although commercial applications were difficult to find, the Air Force envisioned solar power as an ideal technology for a new top-secret project—an earth-orbiting satellite. The Navy initially rejected photovoltaics as an untested, unreliable technology, but finally allowed Vanguard, the first U.S. satellite, to be launched with dual power systems of photovoltaics and chemical batteries. The batteries died in nineteen days, but solar power kept Vanguard communicating with Earth for years [13]. By the 1960's photovoltaics had become the accepted power source for satellite applications, opening a huge market for solar cell manufacturers.

Although the primary concerns for space photovoltaics were mass, efficiency, and durability, cost was the limiting factor for terrestrial applications despite a drop in price from almost $300 per watt in 1956 to $100 per watt by 1970. In the early 1970s, Dr. Elliot Berman, an industrial chemist at Exxon Corporation, developed measures to reduce the cost of solar cells to $20 per watt by using wafers rejected by the semiconductor industry, as well as cheaper packaging materials. The fledgling terrestrial solar industry's first customers were the oil and gas companies, whose offshore rigs required warning lights and horns to prevent ships from running into them, and whose remote fields required small amounts of electricity to reduce corrosion in well heads and pipes.

Over the next twenty years, the number of applications for terrestrial solar power grew prodigiously. The Coast Guard realized that it cost more to maintain the batteries which powered its buoys than the buoys themselves, and replaced power systems in all of its buoys and lighthouses with solar power. Telecom Australia, faced with a mandate to provide long-distance service and television to every Australian citizen no matter how remote his location, developed a vast system of solar-powered repeaters that became the model for remote telecommunications applications. Photovoltaic systems were also increasingly used in rural villages to pump water and provide basic power needs, as well as on the rooftops and facades of urban buildings.

1.3 Photovoltaics present—current technology

1.3.1 Device operation

When light is incident upon a semiconductor material, photons with energy above the band gap of the material are absorbed, and their energy can excite electrons from the valence band to the conduction band of the semiconductor, creating electron-hole pairs. These carriers would normally diffuse throughout the bulk semiconductor until they recombine with one another, but the presence of a charge-separation structure such as a p-n junction, which can be created by doping the material, allows a current to be collected.

The magnitude of the current collected from the solar cell is limited by the rate of carrier recombination, which depends on the population of minority carriers in the device. These minority carriers diffuse to a carrier-depleted region created by the p-n junction, whose internal electric field accelerates them to the opposite side of the junction, where they become majority carriers. As electron mobility in semiconductors is generally larger than hole mobility, photovoltaics are usually designed such that most of the carrier generation occurs in a p-type layer, where electrons are the minority carriers.

1.3.2 Materials for photovoltaics

Since only photons with energies above the band gap of a semiconductor are absorbed, the band gap of the material used for a photovoltaic device must be engineered in order to produce the most power for a given illumination, given that the solar spectrum is close to that of a blackbody at 6000 K, as seen in Figure 1.1 (a). Semiconductors with larger band gaps produce higher photovoltages, but absorb and convert fewer of the incident photons, resulting in lower currents; semiconductors with smaller band gaps absorb most of the solar radiation, but convert most of the energy to heat. In general, the solar cells with the best efficiencies use materials with band gaps near the peak of the solar spectrum, between 1 and 2 eV [1]. The band gaps of many common semiconductors are superimposed on the solar spectrum in Figure 1.1 (b).

Both direct band gap materials, such as the compound semiconductors GaAs, InP, CdTe, and CIS (copper indium diselenide), and indirect band gap materials, like silicon, are used in the fabrication of solar cells. While cells made with direct band gap materials may have higher efficiencies, silicon is more abundant than the elements used to make compound semiconductors. The silicon photovoltaics industry is also able to take advantage of the rejected raw materials and well-established infrastucture for device processing provided by the microelectronics industry.

Both amorphous and crystalline (polycrystalline and monocrystalline) silicon are used in the manufacture of photovoltaic devices. However, amorphous silicon suffers from the Staebler-Wronski effect [14], in which dangling bonds are created under illumination, causing the efficiency to degrade

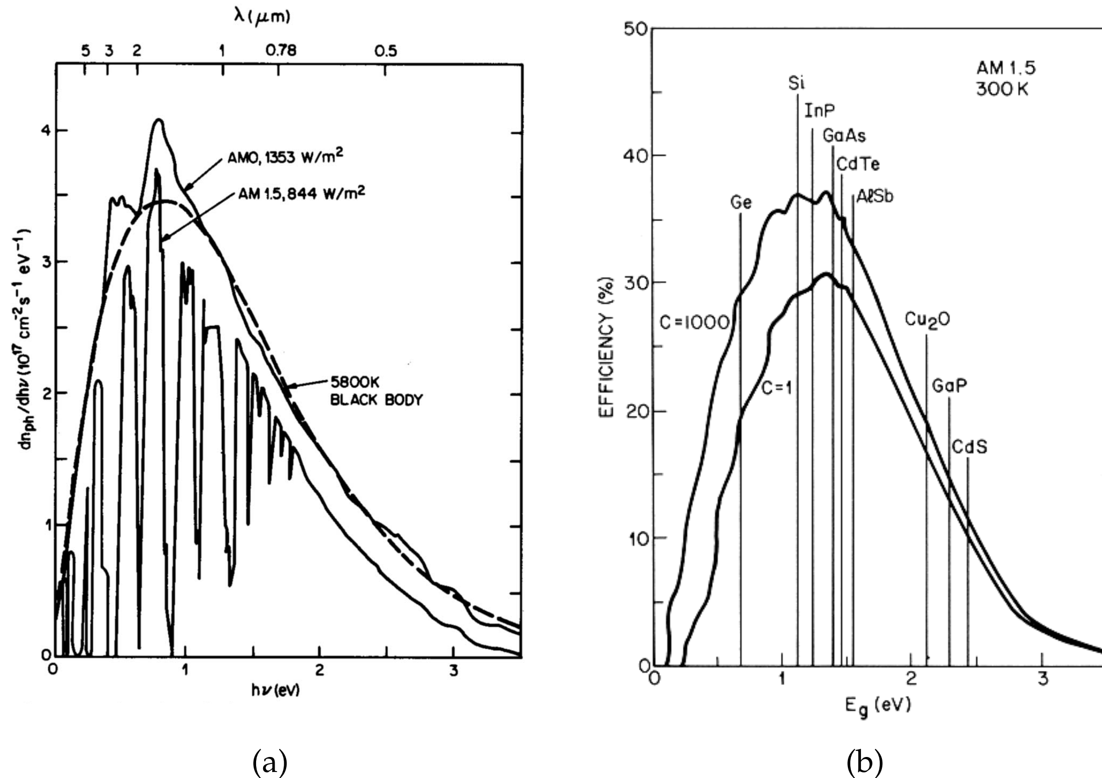

Figure 1.1: (a) Energy spectrum of solar radiation. The large absorption peaks are due mainly to water and CO2 in the atmosphere. (b) Ideal cell efficiency as a function of band gap energy, assuming no losses. The band gaps of several semiconductors used in photovoltaics are labeled. [1]

and capping the maximum efficiency at approximately 12%. We turn then to crystalline silicon technology, which is capable of providing efficiencies greater than 20% [15].

1.3.3 Crystalline silicon technologies

The world record monocrystalline silicon solar cell is the PERL cell fabricated at the University of New South Wales [16], which combines a passivated emitter, back surface field and front-side texturing to achieve an efficiency of 24.5%. Commercially available cells, however, cannot reach the efficiencies of laboratory cells, mostly due to the use of lesser quality substrates and limits imposed by the contact screen-printing process. The best commercial monocrystalline cell is the A-300 module manufactured by SunPower, which has contacts only on the back side, at 20.4% [17]. The Saturn cell manufactured by BP Solar has displayed 18.3% efficiencies and uses a laser-grooved buried contact on the front side [18].

Large-grained polycrystalline silicon material may be fabricated more cheaply than monocrystalline silicon by high-throughput processes such as casting or directional solidification to produce multicrystalline ingots [15]. Although the majority and minority carrier properties of large-grained

polycrystalline silicon are close to those of monocrystalline silicon, it has been shown that the presence of grain boundaries decreases the efficiencies of cells fabricated using this technology [19]. Commercial thick-film polycrystalline modules are available from Bayer, Sharp, and BP Solar; Kyocera's KC module is the cheapest multicrystalline module at $3.16/Wp with 14% efficiency and the Kyocera dBlue module is the most efficient at 15%.

Since approximately half the cost of a finished module comes from the material itself [20], thin-film (<100 μm) crystalline solar cell technology has the potential to substantially reduce cost because a smaller quantity of raw materials is used. Methods such as liquid-phase epitaxy (LPE) and chemical vapor deposition (CVD) have produced high efficiency solar cells through deposition of thin epitaxial films on crystalline silicon substrates. Werner et al. [21] report a 14.7% efficient cell with a 16.8 μm active layer grown by LPE and an efficiency of 17.3% with a 20 μm active layer grown by CVD [22]. However, these techniques are not suited for low-cost production since costly crystalline silicon wafers are still required as substrates and deposition rates are generally low (<5 Å/s). Evergreen Solar has achieved 15% efficient cells by using a string ribbon growth process, by which an edge-supported 100 μm thick silicon ribbon is continuously pulled from a melt, rather than crystalline silicon substrates [23].

1.4 Photovoltaics future—thin-film polycrystalline silicon?

The solar cell industry continues to grow, with worldwide production of solar modules increasing at an average of 18% per year [24] while consumer module prices have decreased to less than $6 per watt [25]. Power generation by photovoltaics, however, is still three to five times as expensive as existing power generation methods. Based on electricity costs of 6c/kWh, in order for a photovoltaic installation to be an attractive investment with a 10% after-tax return, a price of $1.50 per watt must be realized [26].

One of the most promising technologies for reduced-cost photovoltaic modules involves the growth of thin-film polycrystalline silicon on foreign substrates. Although the efficiencies of thin-film polycrystalline solar cells are lower than those of crystalline silicon cells, production costs are significantly lower. In 1997 Astropower Corporation produced the first commercially available polycrystalline silicon thin-film modules using a high-temperature process on a foreign substrate; although few process details are known, laboratory cells with an active layer 50 μm thick displayed efficiencies of 16.6% [27].

Thin-film polycrystalline cells also eliminate some of the quality constraints placed on monocrystalline material which may require costly processing steps, since the minority carrier diffusion length in the polycrystalline film need only be greater than its thickness. Thus even microcrystalline silicon produces cells of moderate efficiency provided the active layer is 1–10 μm thick. Processes which en-

able deposition on low-cost substrates such as glass are particularly desirable, although the processing temperature of the cell must then be kept below the glass transition temperature of the substrate. Yamamoto et al. of Kaneka Corporation [28] have reported a 10.1% efficient microcrystalline cell on glass with only a 2 μm thick active layer with a textured back reflector. Several low-temperature deposition methods for polycrystalline silicon have been studied, including very-high frequency glow discharge (VHF-GD) [29], plasma-enhanced chemical vapor deposition (PECVD) [28] and hot-wire chemical vapor deposition (HWCVD), which is the focus of this study.

Chapter 2

Hot-Wire Chemical Vapor Deposition

Hot-wire chemical vapor deposition (HWCVD) of silicon films involves the decomposition of gas precursors on a heated refractory metal filament producing radical species which react in the gas phase and deposit onto a heated substrate, as shown in Figure 2.1. The microstructure of the resulting films is determined by several reactor parameters, such as the filament temperature, growth pressure, gas flow rates, and substrate temperature.

2.1 Advantages for thin-film photovoltaics

Several aspects of the HWCVD process are especially suited to low-cost photovoltaic applications. High deposition rates for amorphous [30] and polycrystalline [31] silicon have been reported which can be up to one hundred times faster than PECVD. Deposition over a large area is possible with the use of multiple-wire arrays – Ledermann et al. of the University of Kaiserslautern have demonstrated uniform growth over a 20 × 20 cm area [32], and the ANELVA corporation has developed systems designed for 1 square meter deposition [33]. Doped layers have been fabricated with the addition of diborane or phosphine to the process [34].

Microcrystalline films grown by HWCVD display a columnar grain structure with <110> texture, which may be advantageous for photovoltaics since carrier transport occurs along the columns rather than across grain boundaries. Like PECVD, the HWCVD process produces great quantities of atomic hydrogen, which provides in situ passivation of grain boundaries and defects [35]. However, damaging ions that are produced by PECVD are not present in HWCVD. HWCVD-grown films also display a controlled surface roughness, which may enhance light trapping in a photovoltaic device.

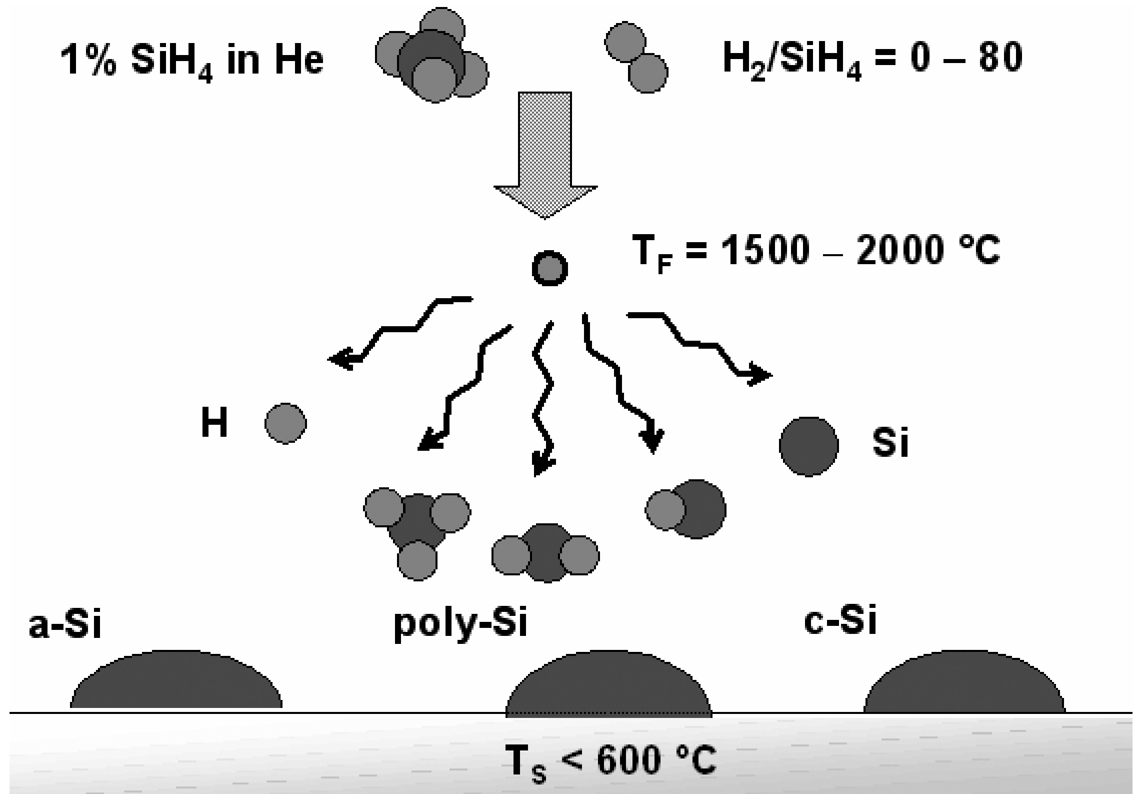

Figure 2.1: Schematic of the HWCVD process.

2.2 Development of HWCVD

In 1979, Wiesmann et al. [36] introduced HWCVD as a method which could produce hydrogenated amorphous silicon (a-Si:H) films at high deposition rates, but the resulting films had inferior electronic properties compared to films grown by plasma enhanced chemical vapor deposition (PECVD). Due to these poor results, the technique was virtually ignored until 1985, when Matsumura et al. [37] demonstrated hydrofluorinated amorphous silicon films of high electronic quality using silicon difluoride and hydrogen precursors; in 1986, Matsumura produced high-quality a-Si:H under similar deposition conditions [38]. They called the process "catalytic CVD" in the belief that the reaction of hydrogen with the heated tungsten filament was catalytic in nature. Doyle et al. [39] also grew high-quality a-Si:H under similar conditions in 1988, naming their process "evaporative surface decomposition" because the filament efficiently decomposed a low-pressure source gas, producing a large flux of deposition radicals. Due to doubts regarding the catalytic reaction of hydrogen with the filament, the process was renamed "hot-wire assisted CVD" in 1991 by Mahan et al.[40], whose thorough comparisons of a-Si:H grown by HWCVD with that grown by PECVD led to tremendous interest in the technique over the next ten years, as shown in Figure 2.2.

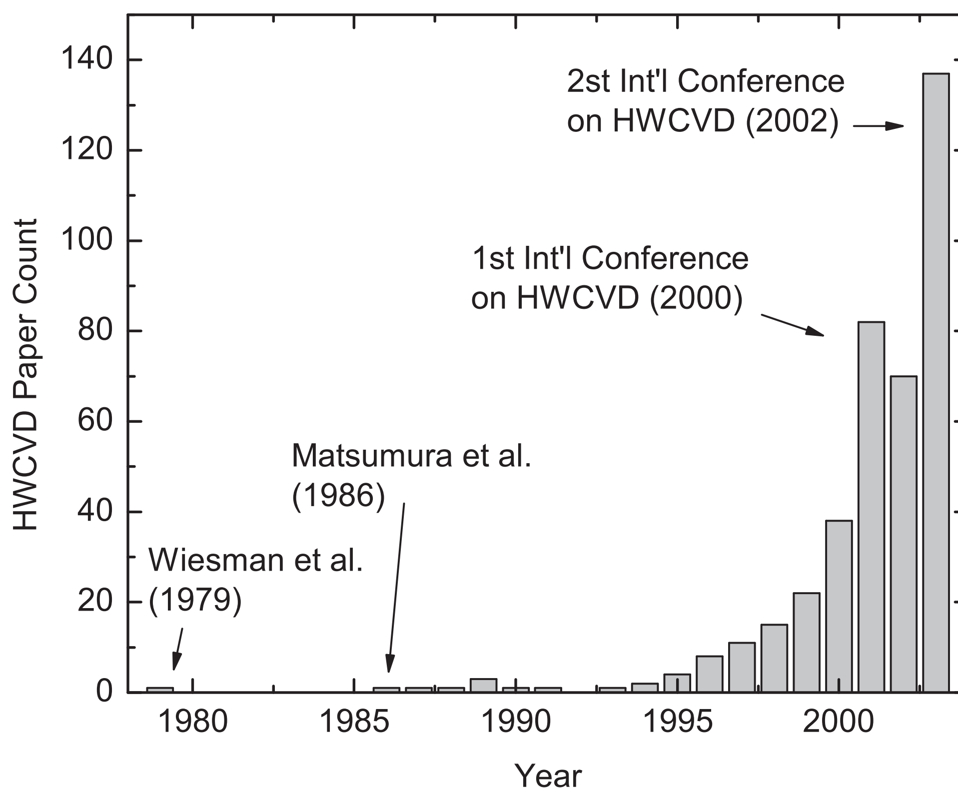

Figure 2.2: Number of papers on HWCVD published since its introduction in 1979. Matsumura resurrected the technique in 1986. The First International Conference on Cat-CVD (Hot-Wire CVD) was held in 2000, with the Second International Conference following in 2002.

2.3 Recent work in HWCVD

The a-Si:H films grown by Mahan et al. [40] were the first device-quality films to be grown by HWCVD. These films had low hydrogen content (<1 atomic percent), which is important as it is believed that hydrogen motion aids the formation of light-induced metastable defects via the Staebler-Wronski effect [14, 41]. This problem in a-Si:H led to interest in the growth of microcrystalline and polycrystalline films by HWCVD – Matsumura was the first to obtain polycrystalline films in 1991 [42], and in 1995 Heintze et al. [43] identified an amorphous-to-microcrystalline transition for HWCVD growth that occurs at a critical H_2:SiH_4 ratio. Several studies of the effects of various reactor parameters on the microstructural and electronic properties of microcrystalline silicon have been performed [43, 44, 45]. Recently, Thiesen et al. [46] demonstrated epitaxial growth on Si(100) by HWCVD at growth rates of up to 10 Å/s.

2.4 Thin-film HWCVD-deposited solar cells

The low hydrogen content of device-quality hot wire-deposited amorphous silicon films makes them useful for inclusion in photovoltaics. In 1998, Bauer et al. at the University of Kaiserslautern recorded an initial efficiency of 10.4% using a p-i-n structure on a glass substrate with the i-layer deposited by HWCVD at low-temperature, although these cells degraded by approximately 30% when exposed to light [47] . In 2000, Kaiserslautern reported 8.0% efficiency using hot-wire deposited p- and n-layers on ITO-coated glass [48]. Nelson et al. at NREL have reported initial efficiencies of 5.7% with i-layers deposited at growth rates of 130 Å/s [30].

Microcrystalline silicon deposited by HWCVD has also shown promise as a material for solar cells. Meier et al. [49] at the University of Neuchâtel have obtained 12% efficiency from a "micromorph" cell using tandem μc-Si:H-a-Si:H cells on ITO-coated glass substrates; the total device thickness is only 1.1 μm. Niikura et al. at École Polytechnique report a 4.6% efficient cell with an n-i-p structure and a 2 μm thick i-layer grown at 300°C [50]. Rath et al. have fabricated an all-HWCVD n-i-p cell with 3% efficiency [51].

2.5 Outline of the thesis

Empirically, it has been noted that solar cells made from material with the largest grain size have the greatest open circuit voltages, for grain sizes between 1 μm and 1 mm [52]. In this study, we investigate the fabrication of large-grained polycrystalline silicon by HWCVD and its suitability for thin-film photovoltaic applications. We have devised two strategies for the fast, low-temperature growth of thin polycrystalline silicon films on glass substrates. The first is the direct growth of polycrystalline silicon on SiO_2 by HWCVD. Here, we will show that the grain size can be controlled by the addition of hydrogen to the process. Our observations of the nucleation kinetics of Si on SiO_2 can be explained by a rate-equation pair-binding model (Chapter 3). The second strategy uses large-grained ($\sim$100 μm) polycrystalline silicon layers fabricated by selective nucleation and solid-phase epitaxy (SNSPE) on SiO_2 substrates as templates for epitaxial growth by HWCVD. We will discuss the microstructural properties of HWCVD-grown epitaxial films on Si(100) and SNSPE templates (Chapter 4), as well as the minority carrier lifetimes and mobilities of these films (Chapter 5).

Chapter 3

Nucleation on SiO_2

Abstract

We use atomic force microscopy (AFM) to characterize fully continuous polycrystalline silicon films grown by HWCVD on SiO_2, as well as the nucleation density of silicon islands formed in the early stages of HWCVD growth, as a function of temperature and H_2 dilution (H_2:SiH_4). We observe an increase in grain size of continuous films with H_2 dilution, from 40 nm using 100 mTorr of 1% SiH_4 in He to 85 nm with the addition of 20 mTorr H_2. This increase in grain size is attributed to atomic hydrogen etching of Si monomers during the early stages of nucleation, which decreases the nucleation density. The nucleation density increases sublinearly with time at low coverage, implying a fast nucleation rate until a critical density is reached, after which grain growth begins. The nucleation density decreases with increasing H_2 dilution, which is an effect of the etching mechanism, and with increasing temperature, due to enhanced silicon monomer diffusivity on SiO_2.

We apply a rate-equation pair binding model of nucleation kinetics [53] to the nucleation of silicon islands grown by hot wire chemical vapor deposition on SiO_2 substrates. From temperature-dependent nucleation density measurements, we estimate the activation energy for surface diffusion of Si monomers on SiO_2 during HWCVD growth to be 0.47±0.09 eV. Simulations of the temperature-dependent supercritical cluster density lead to an estimated activation energy of 0.42 eV±0.01 eV and an estimated surface diffusion coefficient prefactor of 0.1±0.03 cm^2/s. H_2 dilution-dependent simulations of the supercritical cluster density show an approximately linear relationship between the H_2 dilution and the etch rate of clusters at H_2 dilutions between 20:1 and 60:1. The model can also be used to demonstrate possible strategies for the rapid growth of large-grained polycrystalline films by HWCVD.

3.1 Introduction

A key issue for HWCVD films for large-grained thin-film photovoltaics is to identify growth conditions that enable the largest possible grain size at a given growth temperature with low intragranular defect density. Hydrogen is known to play a critical role in the development of a crystalline microstructure in polycrystalline [42, 54, 55] films grown by HWCVD at low temperatures. Good-quality hydrogenated polycrystalline films are produced by the dilution of SiH_4 in H_2—the hot wire decomposes hydrogen molecules into hydrogen atoms which can etch silicon from strained or thermodynamically unfavorable bonding sites [43, 56], which leads to an amorphous to microcrystalline transition. HWCVD proves more successful in the production of polycrystalline films of high crystalline fraction because the hot wire is a much more effective source for this atomic hydrogen than a glow discharge [57], providing the proper balance of etching and hydrogenation of the silicon surface during growth as well as creating radicals for deposition, which enhances the growth rate.

High-quality poly-Si:H films have recently been produced [55] which possess a high crystalline volume fraction and a low density of defect states. Polycrystalline films grown by HWCVD without hydrogen dilution have been shown to display a thin (<50 nm) amorphous incubation layer, from which crystalline grains nucleate and grow to form a <220>-oriented columnar microstructure [58, 59, 60]. With the addition of H_2 to the gas-phase precursors, this amorphous phase can be completely eliminated, producing larger grains with reconstructed grain boundaries which need a hydrogen concentration of less than 0.5 atomic percent to completely passivate them. This is shown to greatly improve the electrical transport properties of these films [51], although the growth rate is decreased. In our study, the role of atomic hydrogen produced by the wire in the etching of Si and its effect on the resulting film microstructure are investigated through experiments and quantitative modelling of the nucleation kinetics of Si on SiO_2 at low substrate coverage.

3.2 Experiment

All film growth experiments were performed at base pressures of no higher than 1x10^{-6} Torr. Operating pressures were 100 mTorr of a mixture of 1% SiH_4 in He, to which 20-140 mTorr of H_2 was added. A single straight tungsten wire of 12 cm length and 0.25 mm diameter was resistively heated to 2000°C and positioned 2.5 cm from the substrate. The wire radiatively heated substrates consisting of 100 nm SiO_2 on Si to 300°C; higher substrate temperatures were achieved by heating with a resistive substrate heater in combination with the wire. H_2 dilutions are referenced to 1 mTorr of SiH_4 in 99 mTorr He; all gases used are ultrahigh purity. A translatable shutter between the wire and substrate enabled several growth experiments to be performed at low silicon coverage on each substrate under identical gas ambient and wire temperature conditions, and also provided a definite

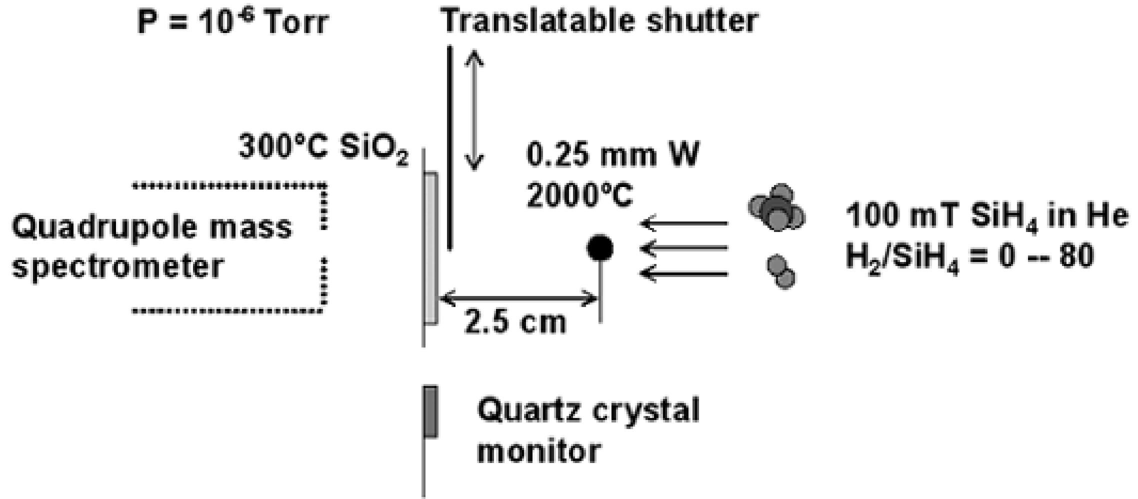

Figure 3.1: Schematic of hot-wire CVD experiments.

starting and ending point for film growth. A schematic of the experimental setup is displayed in Figure 3.1.

In separate experiments, the substrate was replaced by a quartz deposition monitor (Inficon XTC/2), which was used to measure the growth and etch rates of silicon as a function of H_2 dilution from 0-150:1, and by the orifice of a differentially pumped mass spectrometer (Hiden Analytical Ltd., HAL RC201), with which the gas-phase radical species produced by the wire were measured.

Evidence for atomic hydrogen etching of silicon was demonstrated by H_2-dilution-dependent measurements of the net Si growth rate, measured by the quartz crystal deposition monitor at the substrate position, as well as by a separate experiment which measured the flux of SiH_4 using a differentially-pumped quadrupole mass spectrometer with orifice at the substrate position [61]. The results of these experiments can be seen in Figure 3.2. A decrease in growth rate and corresponding increase in SiH_4 flux with increasing H_2 dilution were attributed to atomic hydrogen etching of Si species from the substrate and chamber walls and recombination of these species in the gas phase to form SiH_4. A transition from net growth to net etching of silicon occurs with the addition of approximately 80 mTorr of H_2. Since the silicon grown on the quartz deposition monitor is amorphous, and crystalline silicon has been shown to etch more slowly than amorphous silicon under atomic hydrogen exposure [56], the transition between net growth and net etching for crystalline films likely occurs at a higher H_2 dilution.

In subsequent experiments, the nucleation density at low Si coverage on a 100 nm SiO_2 layer was determined using contact-mode atomic force microscopy (AFM), as illustrated in Figure 3.3(a). This image was taken after a growth time of 90 seconds at 20:1 H_2 dilution. For each sample, 5 scans of 25 μm^2 were performed; the observable nuclei were then counted for each scan and the resulting numbers of nuclei were averaged. As seen in Figure 3.4, which displays the nucleation data as a

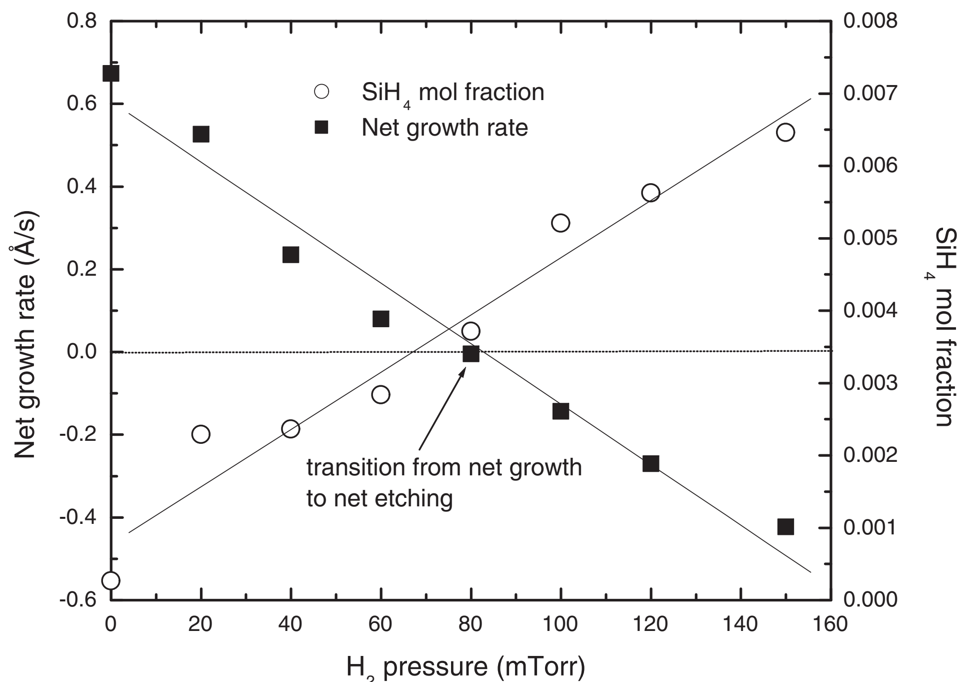

Figure 3.2: Net deposition rate and SiH_4 mole fraction as a function of H_2 partial pressure in 100 mTorr of dilute SiH_4 1% in He.

function of H_2 dilution at 300°C, the nucleation density increases sublinearly with time, implying a nucleation rate which is initially high until a critical density of nuclei is reached, at which time the nucleation rate is sharply reduced and grain growth begins. Exposing the SiO_2 substrates to 60 mTorr H_2 for 10 minutes before growth had no effect on the nucleation density, demonstrating that exposure to H_2 does not appreciably etch or roughen the surface of the SiO_2. The nucleation density was highest for no added H_2 and decreased with H_2 dilution. This result is consistent with the AFM micrographs in Figure 3.3(b) and (c), which indicate an increase in grain size in thick, continuous films (~200 nm) from 40 nm with no H_2 dilution to 85 nm at a H_2 dilution of 20:1. The nucleation density also decreased with increasing temperature due to enhanced diffusivity of Si monomers on SiO_2. From the temperature-dependent nucleation density measurements performed at substrate temperatures of 300-450°C presented in Figure 3.5, we estimate the activation energy for surface diffusion of Si on SiO_2 to be 0.47±0.09 eV.

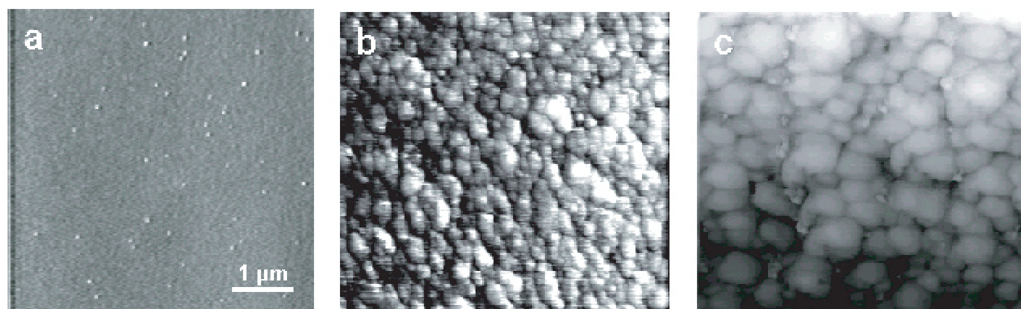

Figure 3.3: (a)AFM of the HWCVD nucleation phase. This image was taken after a growth time of 90 seconds at 20:1 H_2 dilution. Bright features are ≥35 nm in height. (b) Post-coalescence 1 μm^2 image of a continuous poly-Si film grown at zero H_2 dilution; grain size is 40 nm. (c) Post-coalescence 1 μm^2 image of a continuous poly-Si film grown at 20:1 H_2 dilution; grain size is 85 nm.

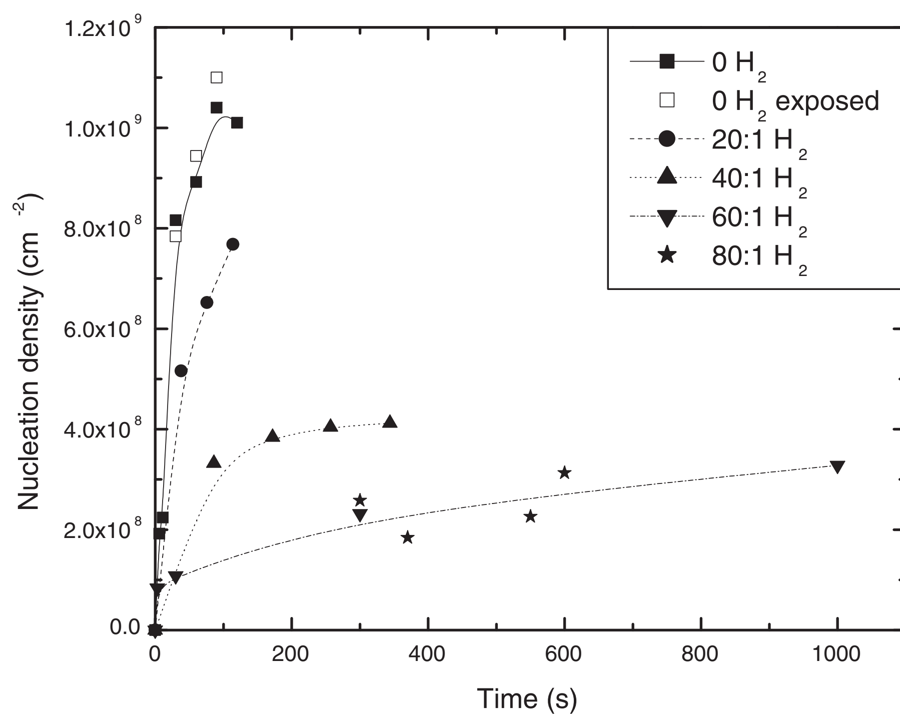

Figure 3.4: Nucleation data as a function of H_2 dilution at 300° C. The lines are a guide to the eye.

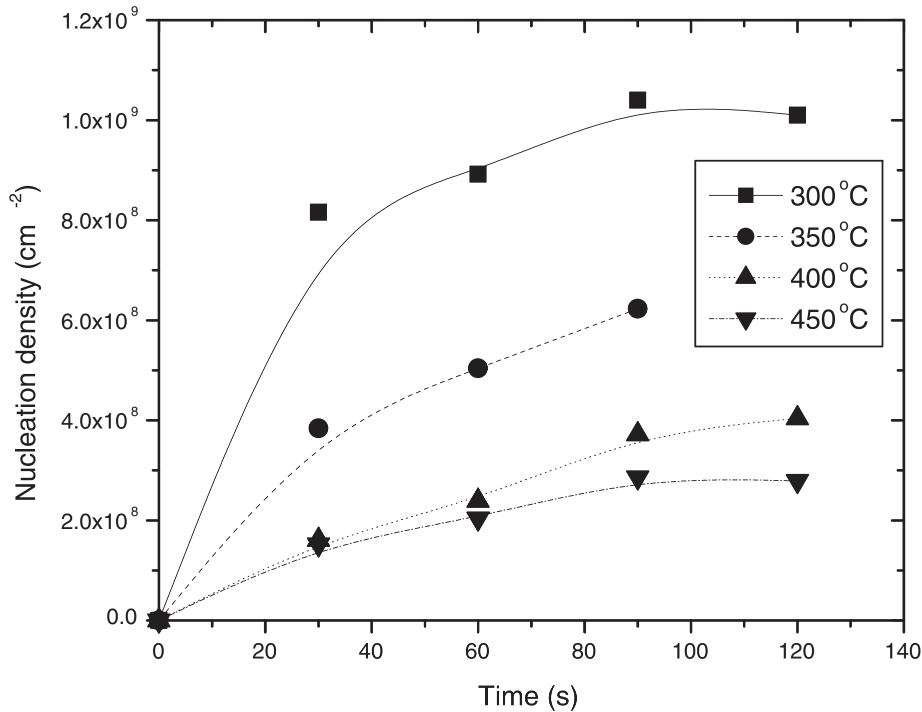

Figure 3.5: Temperature-dependent nucleation measurements. The lines are a guide to the eye. The initial slope of the data were used to estimate the activation energy for surface diffusion of Si on SiO_2.

3.3 Quantitative modelling

We quantitatively model the observed nucleation kinetics of Si on SiO_2 through a rate-equation pair binding framework developed by Venables [53], which assumes that only monomers n_1 (which could be Si adatoms or adsorbed SiH_3 molecules) are mobile on the surface. The equations governing the density n_j of clusters of size j are

$$\frac{dn_1}{dt} = R - \frac{n_1}{\tau_a} - \frac{d(n_x w_x)}{dt}, \tag{3.1}$$

$$\frac{dn_j}{dt} = 0 \, (2 \leq j \leq i) \tag{3.2}$$

$$\frac{dn_x}{dt} = \sigma_i D n_1 n_i - 2 n_x \frac{dZ}{dt} \tag{3.3}$$

Equation 3.1 describes the evolution of the monomer population n_1 due to arrival of atoms from the gas phase at rate R, evaporation with time constant τ_a, and incorporation into existing clusters, where $n_x w_x$ is the total number of atoms in existing clusters. Equation 3.2 gives a thermodynamic

equilibrium between subcritical clusters smaller than the critical size i, and Equation 4.6 gives the supercritical cluster density n_x in terms of a nucleation rate $\sigma D n_1 n_i$ and a coalescence rate proportional to Z, the rate of change of the substrate coverage by stable clusters. Equations 3.1 and 3.3 are coupled by the interaction between nucleation and growth, whereby single adatoms are incorporated into stable clusters by nucleation, diffusion capture, and direct impingement, so that

$$\frac{d(n_x w_x)}{dt} = \frac{n_1}{\tau_n} + \frac{n_1}{\tau_c} + RZ \tag{3.4}$$

where ${\tau_c}^{-1} = \sigma_x D n_x$. The nucleation term τ_n is unimportant numerically and can be ignored; the capture numbers σ [62, 63] and the diffusion coefficient $D = D_0 \exp[E_a/kT]$ are given by the solution of the two-dimensional diffusion equation on the substrate. For complete condensation conditions, the theory can be used to predict the stable cluster density, which depends on the activation energy for surface diffusion (E_a) and lateral binding energy (E_b) [63].

For a critical cluster size i=1, which predicts the lowest monomer density on the surface, a lateral binding energy for silicon clusters E_b=1.55 eV [64] and for a rate R=5x10^{10} cm^{-2}s^{-1} (determined by calculating the total volume of Si deposited on the substrate from AFM images), we estimate the diffusion coefficent prefactor D_0 and the activation energy E_a for Si diffusion on SiO_2 by using the model to fit the temperature-dependent supercritical cluster density measurements, as seen in Figure 3.6, under complete condensation conditions, i.e., assuming that no etching occurs under pure SiH_4 conditions. It should be noted that a critical cluster size i=1 implies that there is no barrier to nucleation. The data are best approximated with values of D_0=0.1 cm^2/s and E_a=0.42 eV. Increasing the activation energy causes the linear regime of the simulated supercritical cluster density curves to persist for longer times, while increasing D_0 causes the family of curves to display an increased supercritical cluster density. The simulated curves fit the experimental data within a factor of two; the simulation parameters were chosen so as to generally overestimate rather than underestimate the experimental cluster densities, as it is reasonable that supercritical clusters exist on the substrate which cannot be resolved with the AFM. The simulated value of E_a is within the error of the least-squares fit used to determine the activation energy experimentally.

To model the effects of H_2 dilution at substrate temperatures of 300°C and 400°C, the adatom stay time τ_a was modified to account for the etching of monomers from the substrate by atomic hydrogen. The results are shown in Figure 3.7. Here, the data at H_2 dilutions from 20:1-60:1 are not overestimated, but are fit as closely as possible in order to determine the relative etch rates for the different H_2 dilutions. The difference in the values of τ_a at identical dilution for the two different temperatures suggests a temperature-dependent reactive etching mechanism for Si monomers by atomic hydrogen. The rate at which adatoms are etched from the substrate by atomic hydrogen should be proportional to the etch yield Y of Si by atomic hydrogen, the flux Φ_H of atomic H at

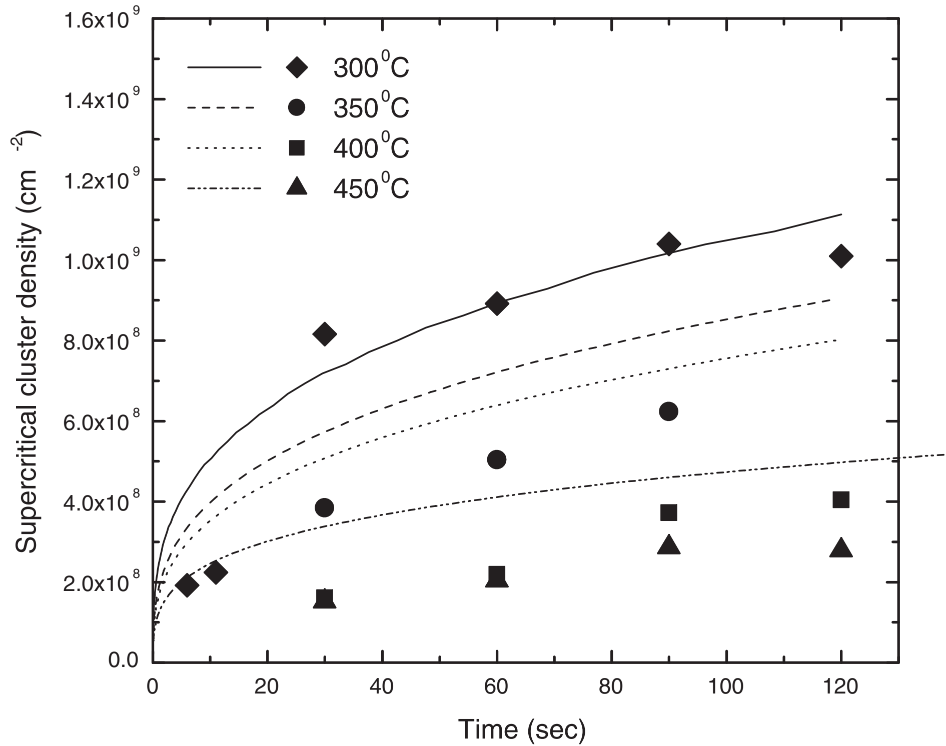

Figure 3.6: Comparison of simulated (lines) and experimental (dots) temperature-dependent cluster density measurements.

the surface, and the fraction f_{n_1} of the substrate covered by monomers, such that

$$\frac{1}{\tau_a} = Y \Phi_H f_{n_1} \tag{3.5}$$

Simulation predicts a maximum monomer concentration on the order of 10^6 cm^{-2} and a value for f_{n_1} of order 10^{-9}. Φ_H is on order 10^{16} cm^{2}s^{-1}. The etch rates (on the order of 10^{-6}) predicted by the simulation in turn predict a reasonable etch yield of Si by atomic hydrogen of Y=0.1. These etch rates show an approximate linear relationship with H_2 dilution, shown in Figure 3.8. This suggests that atomic hydrogen etching of monomers, rather than competitive etching of stable, supercritical amorphous and crystalline nuclei, may be the dominant process governing the nucleation kinetics at low coverage. The etch yield also appears to be temperature-dependent, which, in addition to the difference between the critical cluster size and the observable cluster size, may add to the discrepancy between the predicted and experimental temperature-dependent data.

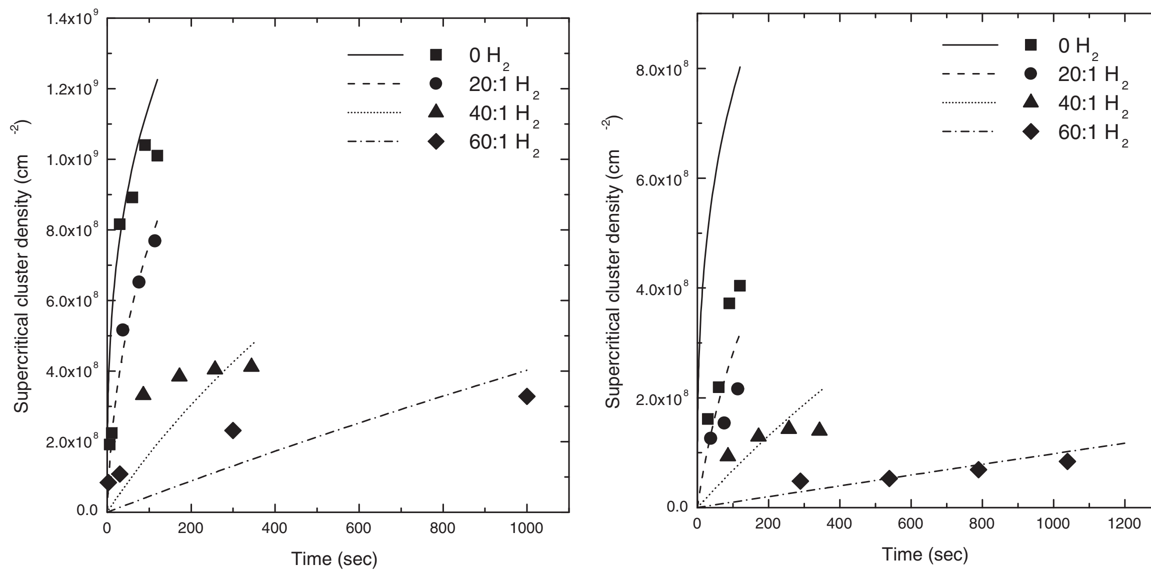

Figure 3.7: Comparison of simulated and experimental H_2 dilution-dependent cluster density measurements at (a) 300°C and (b) 400°C.

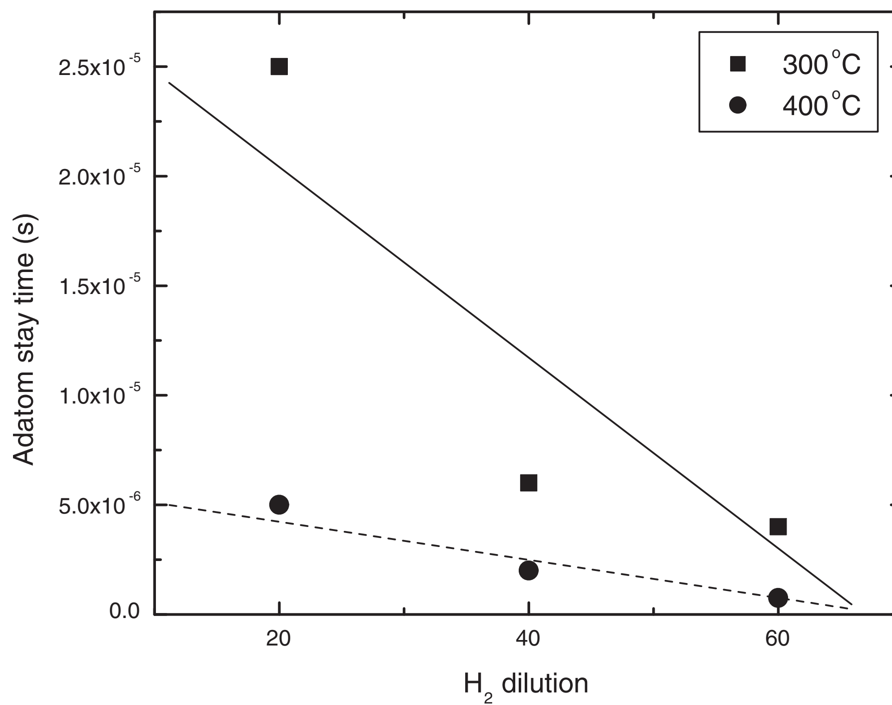

Figure 3.8: Adatom stay time as a function of H_2 dilution.

3.4 Microstructural control

We also investigate strategies for the fast growth of large-grained polycrystalline films by HWCVD. One such strategy is to first grow a low-density layer at high H_2 dilution, which will serve as a seed layer for the fast growth of large grains at low H_2 dilution [65]. To test this strategy experimentally, a low-density seed layer was grown at 300°C at an H_2 dilution of 60:1. After one thousand seconds, the H_2 dilution was reduced to zero, and growth was allowed to proceed for 300 seconds. Although this strategy could have been further optimized, the results, displayed in Figure 3.9, are encouraging – although the nucleation density does increase compared to continued growth at 60:1 H_2 dilution, it is indeed suppressed with respect to growth at 0 H_2 dilution.

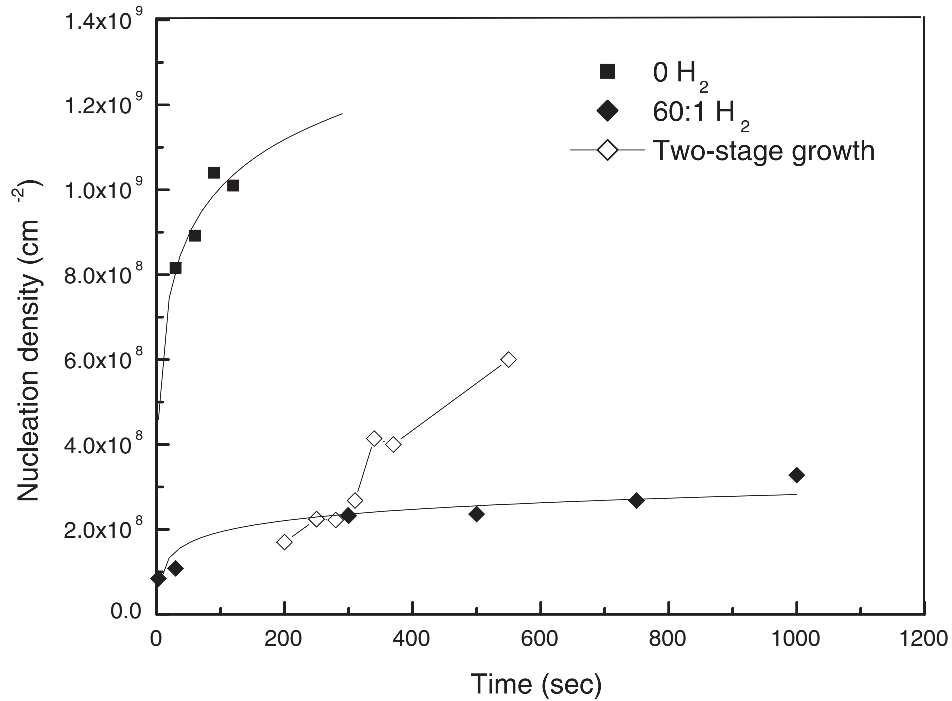

Figure 3.9: Two-stage growth experiment, as compared to undiluted growth and growth at 60:1 H_2. The lines which fit the data at 0 H_2 and 60:1 H_2 are guides to the eye.

The pair-binding model enables us to model this behavior, as well as consider more interesting strategies. As an example, we consider a case similar to an experiment performed by Rath et al.[66], where a seed layer is again grown at 60:1 H_2 dilution, after which the H_2 dilution is gradually ramped down to zero over the next 700 seconds. As seen in Figure 3.10, this strategy proves more effective in suppressing the nucleation density than the two-stage growth strategy. Table 3.1 shows the time necessary for the grains of polycrystalline films to coalesce as well as the grain density of

Table 3.1: Coalescence times and grain densities of continuous films under various H_2 dilution conditions, as predicted by the pair-binding model.

H_2 dilution	Coalescence time (s)	Continuous film grain density (cm^{-2})
60:1	12000	2.3 x 10^9
Two-stage	5000	3.0 x 10^9
Ramp	7500	2.6 x 10^9

the resulting continuous films as predicted by the pair-binding model. The model predicts that films grown under ramped dilution will not only coalesce faster than those grown at 60:1 dilution, but possess a lower grain density than those produced by the two-stage growth condition.

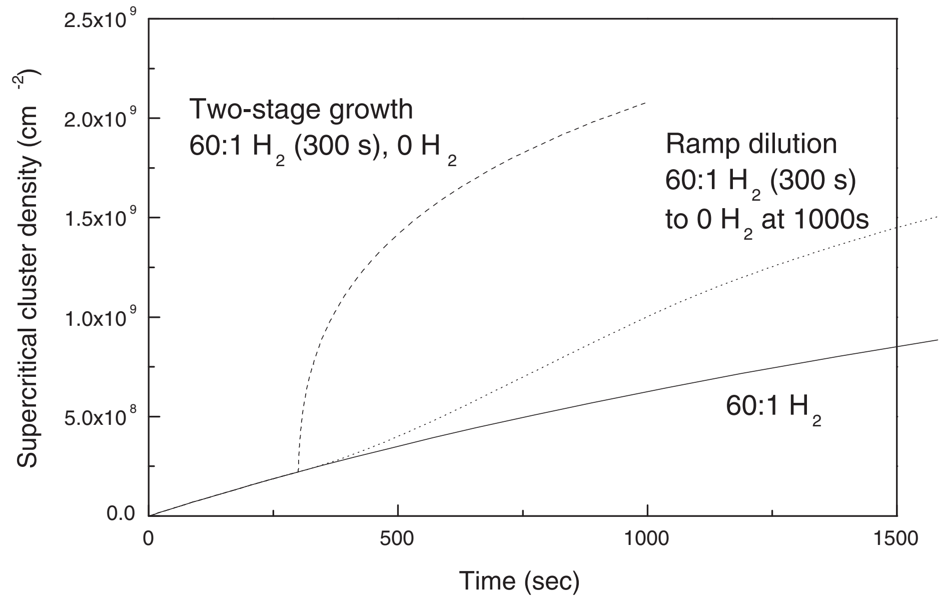

Figure 3.10: Pair-binding model simulations of growth at 60:1 H_2 dilution, two-stage growth, and ramped dilution.

3.5 Conclusions

An increase in grain size of continuous polycrystalline silicon films with H_2 dilution can be attributed to atomic hydrogen etching of silicon monomers, decreasing the nucleation density. Experiments show that the nucleation density increases sublinearly with time at low coverage, implying

a fast nucleation rate until a critical density is reached, after which grain growth begins. Through temperature-dependent nucleation-density measurements, the activation energy for diffusion of Si monomers on SiO_2 during HWCVD growth is estimated to be 0.47±0.09 eV. To our knowledge, this is the first estimate for this activation energy given in the literature.

The experimental nucleation density measurements can be understood within the framework of a rate-equation pair-binding simulation. Modelling of the temperature-dependent cluster density measurements give D_0=0.1±0.03 cm^2/s and E_a=0.42±0.01 eV, which is within the error in the experimentally determined value. Monomer etching by atomic hydrogen is simulated by changing the adatom stay time τ_a, and the simulated etch rates vary approximately linearly with H_2 dilution. The model can also be used to explore possible strategies for the rapid growth of large-grained polycrystalline films by HWCVD.

Chapter 4

Epitaxial Growth by HWCVD

Abstract

We investigate the low-temperature (300–475°C) epitaxial growth of thin silicon films by hot-wire chemical vapor deposition on Si(100) substrates and on large-grained polycrystalline template layers formed by selective nucleation and solid phase epitaxy (SNSPE). Using reflection high energy electron diffraction (RHEED) and transmission electron microscopy (TEM), we have derived a phase diagram for Si on Si(100) consisting of epitaxial, twinned epitaxial, mixed epitaxial/polycrystalline, and polycrystalline phases of growth on Si(100) in the 50 nm–2 μm thickness regime. Evidence is also presented for epitaxial growth on SNSPE templates, which use nickel nanoparticles as nucleation sites for the solid-phase crystallization of phosphorus-doped amorphous silicon on SiO_2.

4.1 Introduction

HWCVD has been shown to be a promising method for fast, low-temperature (<600°C) epitaxy [46, 67, 68]. Previously, we showed that direct deposition by HWCVD on SiO_2 produced small grains (40–80 nm), even with the addition of H_2 to a dilute mixture of 1% SiH_4 in He. Our second strategy for the fabrication of large-grained polycrystalline silicon photovoltaics uses a polycrystalline silicon layer with grain size on the order of 100 μm as a template for epitaxial growth by HWCVD. These layers are formed using nickel nanoparticles as nucleation sites for the solid-phase crystallization of phosphorus-doped amorphous silicon on SiO_2 and have been successfully used as seed layers for epitaxial growth by molecular beam epitaxy (MBE) at temperatures below 600°C [3, 69]. In this chapter, we will discuss the microstructural properties of epitaxial films grown by HWCVD on Si(100) substrates and polycrystalline templates.

4.2 Low-temperature epitaxy

There are several means of growing epitaxial silicon films at low temperature. In one class of processes, which includes MBE and low-pressure chemical vapor deposition (LPCVD), increasing the growth temperature generally leads to an increase in the maximum attainable epitaxial film thickness [70]. A critical bulk concentration of atomic hydrogen leads to the premature breakdown of epitaxy [71], although epitaxial silicon can be deposited by MBE on a surface covered with one monolayer of hydrogen [72]. At low surface coverages, hydrogen atoms act as a diffusion barrier for silicon atoms, thus dramatically increasing the Si island density, accelerating an increase in surface roughness, and causing early epitaxial breakdown by a transition from crystalline to amorphous growth [73].

Other processes, such as plasma-enhanced chemical vapor deposition (PECVD) and HWCVD, involve high gas pressures and deposition sources that are also efficient sources of atomic hydrogen, which can abstract surface hydrogen and etch silicon. In such processes, an increase in growth temperature does not necessarily lead to an increase in epitaxial thickness. Since growth proceeds by abstraction reactions, it is the concentration of hydrogen at the surface rather than the bulk concentration that may affect the limiting thickness of epitaxial growth. A balance between the flux of atomic hydrogen incident on the growth surface and the thermal desorption of hydrogen may be required [74]. Upon the breakdown of epitaxy, films grown by these processes often undergo a transition to polycrystalline growth rather than a transition to amorphous growth [75].

4.3 Epitaxy on Si (100)

4.3.1 Initial experiments

4.3.1.1 Growth conditions

Silicon films of 300 nm thickness were grown on Si(100) substrates by HWCVD at temperatures between 300-450°C using 70 mTorr H_2 at 20 sccm and 100 mTorr dilute SiH_4 in He at 20 sccm. A 0.5 mm diameter tungsten filament was heated to 1850°C and placed 5 cm from the substrate, resulting in a growth rate of 0.15 Å/s. These initial conditions were chosen to produce amorphous silicon films on SiO_2, similar to those investigated by Seitz et al. [67]. Substrates were cleaned with UV-ozone for 10 minutes and dipped in hydrofluoric acid, then heated to 200°C in vacuum to desorb hydrocarbons [76]. Ultra-high purity gas mixtures were used and the base pressure of the growth chamber was below 10^{-6} Torr.

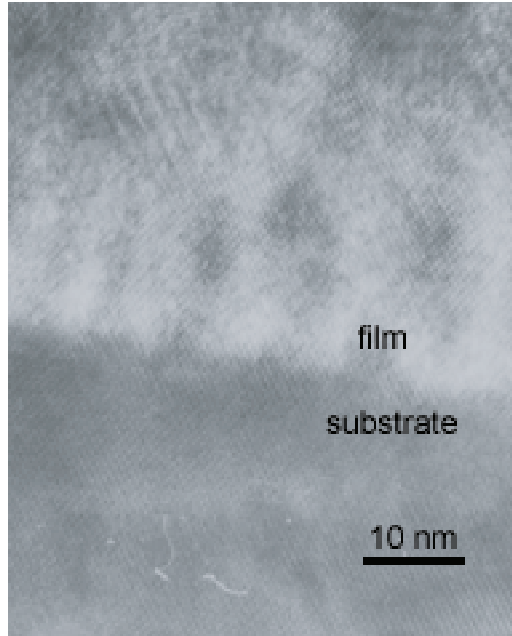

Figure 4.1: Cross-sectional TEM of HWCVD-grown Si on Si (100) at 300°C. The epitaxial films display a periodic array of stacking faults.

4.3.1.2 Results

Cross-sectional TEM of films grown on Si(100) substrates at 300°C confirms the presence of epitaxial growth, as shown in Figure 4.1. The rough film-substrate interface is believed to have been caused by etching of the surface during growth by atomic hydrogen produced by the wire [77]. The roughened appearance of the silicon substrate in cross-section may be due to the presence of hydrogen platelet defects arising from the diffusion of hydrogen into the film during growth, although the exact structure of the defects has yet to be determined. Epitaxy continues to a thickness of approximately 240 nm, after which the film becomes highly twinned, as seen in Figure 4.2 (a). The epitaxial films exhibit a periodic array of stacking faults which gives rise to the higher-order spots seen in the diffraction patterns in Figure 4.2 (b) and (c).

TEM of films grown at 400°C, shown in Figure 4.3, reveals mixed phase growth with some areas of epitaxial growth at the interface and a quick transition to polycrystalline growth as seen in the diffraction pattern. More prominent hydrogen-induced defects are present in the substrate, perhaps due to the enhanced diffusion of hydrogen into the substrate at higher temperatures.

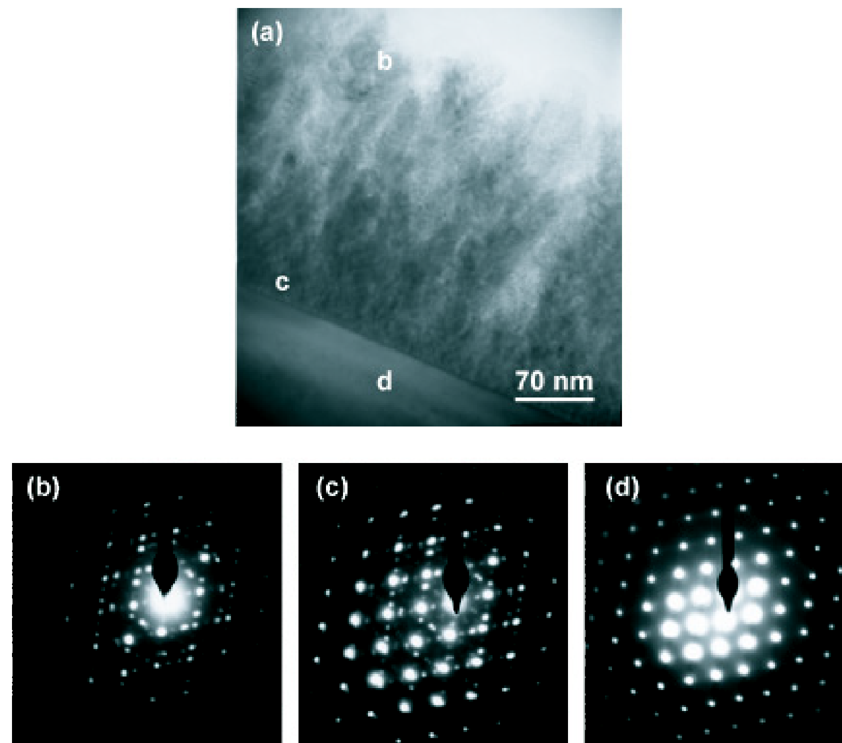

Figure 4.2: (a) Cross-sectional TEM of HWCVD-grown Si on Si (100) at 300°C. The films become highly twinned after a thickness of approximately 240 nm. Labels b, c, and d refer to areas from which selected-area diffraction patterns were obtained. (b) Selected area diffraction from HWCVD film and amorphous glue layer. (c) Selected area diffraction from HWCVD film and Si (100) substrate. (d) Selected area diffraction from Si (100) substrate. Higher-order spots in (b) and (c) are due to the periodic array of stacking faults in the epitaxial film and twinning in the uppermost regions of the film.

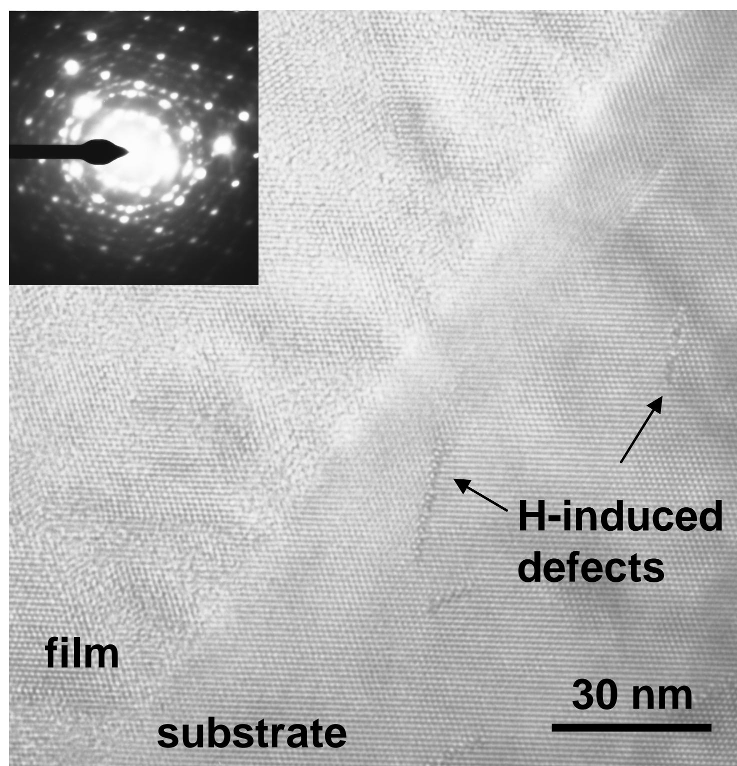

Figure 4.3: Cross-sectional TEM of HWCVD-grown Si on Si (100) at 400C°, which displays mixed epitaxial/polycrystalline growth. Hydrogen-induced defects are present in the substrate.

4.3.2 Further experiments

4.3.2.1 Growth conditions

The epitaxial films discussed in section 4.3.2.2 were grown in a reconfigured reactor using a mixture of 4% SiH_4 in He at a pressure of 25 mTorr and a flow rate of 16 sccm, providing the same amount of SiH_4 in the reactor as in the previous experiments. Under these conditions, the maximum achievable H_2:SiH_4 ratio was 50:1, using 50 mTorr H_2 at a flow rate of 52 sccm. The wire was positioned at a distance of 2.5 cm from the substrate in order to increase the growth rate to 1 Å/s for diluted growth. This required a decrease in wire temperature to 1800°C in order to minimize tungsten incorporation into the films. The wire radiatively heated the substrate to 300°C and, with the addition of a separate resistive heater, substrate temperatures up to 475°C could be achieved. Under these conditions, undiluted growth at all temperatures produced polycrystalline films. Vacuum pressures were kept below 5×10^{-7} Torr and inline gas purifiers (Nanochem MiniSentry) were added to the system to further decrease carbon and oxygen contamination.

Before growth, surfaces were cleaned with UV ozone for 10 minutes, dipped in HF, and heated to 200°C in vacuum to desorb hydrocarbons as before. Since low doses of atomic hydrogen have been

shown to be an effective in-situ method for removing surface carbon and oxygen[78, 79, 80] residual hydrocarbons [81, 82] and submonolayer oxides [83], for these experiments an additional atomic hydrogen cleaning step was added. If the dose is kept below 300-400 Langmuir, no appreciable surface roughening should occur [84]. Samples were cleaned for 5 minutes with atomic hydrogen at an H_2 flow rate of 2.2 sccm, corresponding to a chamber pressure of approximately 10^{-4} Torr. We estimate the total dose of atomic hydrogen to which the substrate is exposed by considering the wire as an effusion source of atomic hydrogen. The relation

$$\Gamma = \frac{P_{eq}}{\sqrt{(2\pi)mkT}} \tag{4.1}$$

where P_{eq} is the chamber pressure, m is the mass of a hydrogen atom, k is Boltzmann's constant and T is the temperature of the wire, can be used to calculate the flux of hydrogen Γ_s at the wire and subsequently at the substrate, assuming a geometry where the wire and substrate are concentric cylinders[85]. Assuming that all hydrogen molecules dissociate on the wire, we calculate that the maximum total dose of atomic hydrogen to which the sample is exposed during the cleaning is 360 L. AFM measurements on an unexposed Si(100) substrate and one exposed to a 360 L atomic H dose showed that no observable roughening of the surface takes place during the atomic hydrogen cleaning. Exposure to doses of atomic hydrogen below this threshold has also been shown not to affect hydrogen surface coverage [75].

Films were grown at an H_2:SiH_4 ratio of 50:1 at substrate temperatures from 300–475°C. Using the translatable shutter described in Chapter 3, we were able to grow films of several different thicknesses under identical growth conditions. The microstructure of the resulting films was characterized by TEM, RHEED and AFM.

4.3.2.2 Results

Transmission electron microscopy Figure 4.4 shows TEM micrographs of a film grown at 300°C to a thickness of 350 nm. Figure 4.4 (a) gives evidence for epitaxial growth to a thickness of approximately 50 nm, followed by the emergence of stacking faults and twin boundaries which give rise to the extra spots in the diffraction pattern. The contrast at the film/substrate interface is likely due to submonolayer contamination, possibly by tungsten. Figure 4.4 (b) shows that the stacking faults and twinning extend from the initial 50 nm epitaxial layer through the full thickness of the epitaxial film.

The 15 μm thick film in Figure 4.5 (a) displays twinned growth directly from the interface, probably due to inadequate surface preparation. A mixed phase of twinned epitaxial and polycrystalline growth is observed (Figure 4.5 (b)), with regions of twinned crystalline growth extending as far as 300 nm into the film. The grain size of the polycrystalline film is on the order of 1 μm. The average

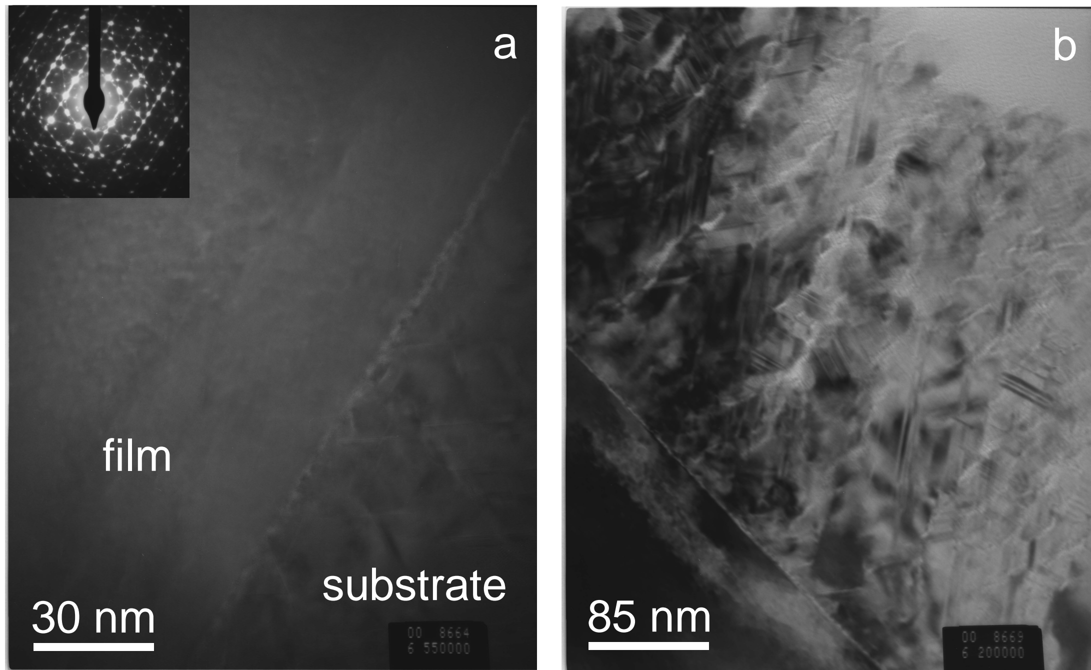

Figure 4.4: Cross-sectional TEM of 350 nm-thick film grown at 300°C. (a) 50 nm-thick epitaxial layer before twinned growth begins. Inset: diffraction pattern from twinned region; (b) Twinning continues throughout film growth.

growth rate for the polycrystalline film was 2.3 Å/s, which is more than twice as large as the growth rate of 1 Å/s calculated for thin epitaxial films. The increased deposition rate for polycrystalline films may be due to an increase in the number of possible growth sites as the film surface roughens.

Reflection high-energy electron diffraction RHEED is a technique which provides information about sample surface morphology. A 25 keV electron beam was incident upon the sample surface at a grazing angle of 1.5°. The resulting elastic scattering features from the surface provide qualitative information about the surface morphology. We found that these features correlate well with the microstructure observed by TEM, eliminating the need for tedious sample preparation and analysis. Although the measurements described here were performed in a separate chamber, RHEED could easily be incorporated into a HWCVD reactor to allow the in situ observation of surface morphology at various stages of growth, although the high growth pressures used in HWCVD would make it necessary to stop growth before each RHEED measurement.

Figure 4.6 shows the RHEED patterns of several films grown at 300°C. At 60 nm [Figure 4.6(a)], double diffraction spots of lesser intensity than the main Si (100) spots first appear, indicating twinned growth. These double diffraction spots correlate with the TEM images in Figure 4.4, in which the onset of twinning is observed at a thickness of approximately 50 nm. The double diffraction

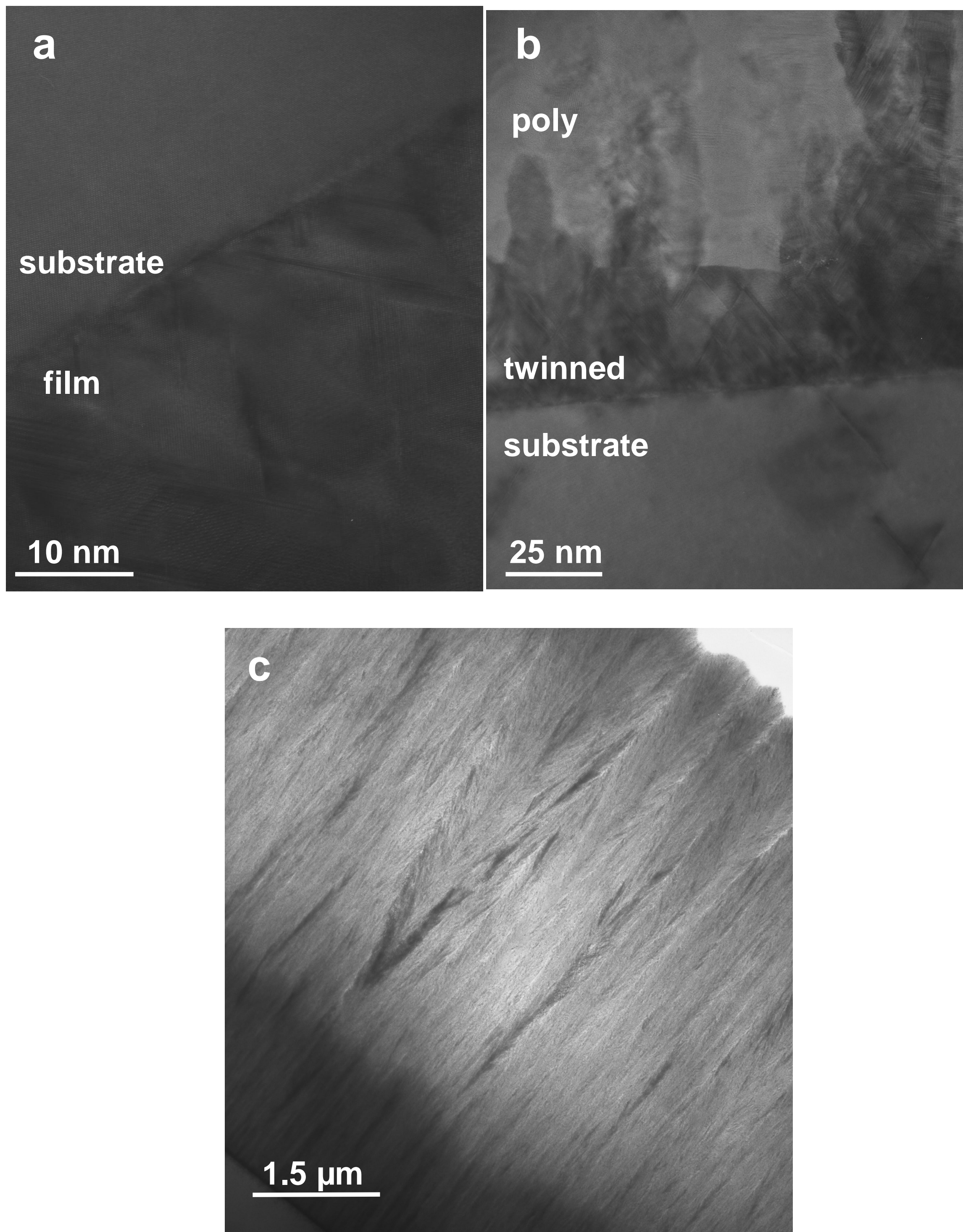

Figure 4.5: Cross-sectional TEM of 15 μm thick film grown at 300°C. (a) Stacking faults and twinning begin at interface. (b) Mixed twinned epitaxial/polycrystalline growth; twinned regions extend as far as 300 nm into film. (c) Grain size of polycrystalline film is on the order of 1 μm.

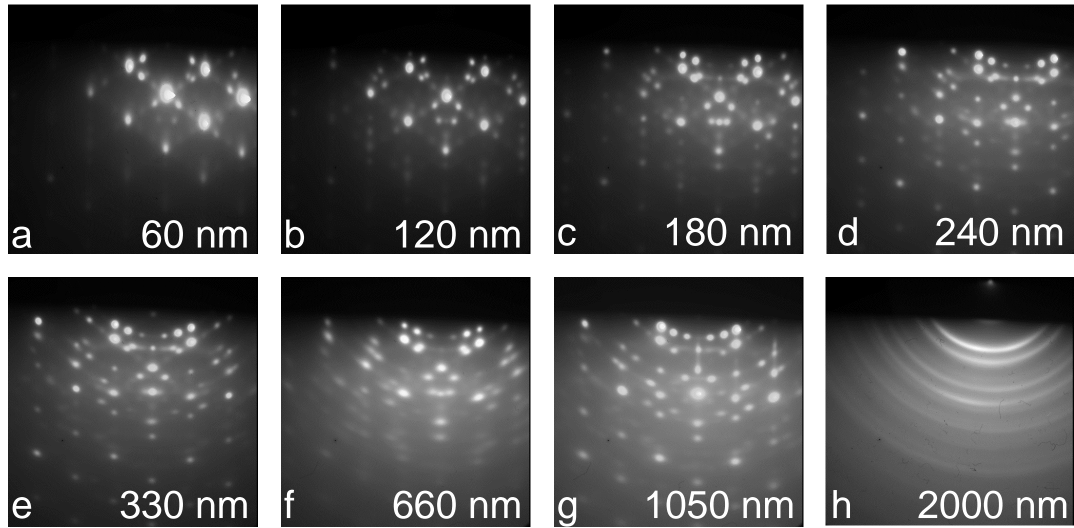

Figure 4.6: RHEED patterns of films of increasing thickness grown at 300°C. The beam is along the <110> direction. Two phases of growth are observed: twinned epitaxial growth [a-g] and polycrystalline growth [h].

spots increase in intensity as the films grow thicker, indicating that twinned epitaxial growth persists to a thickness of 1 μm, and new spots related to surface roughening appear [86]. At a thickness of 2 μm, a ring pattern consistent with a transition to polycrystalline growth is observed [Figure 4.6(h)].

Atomic force microscopy AFM (Park Autoprobe) was used to characterize the surface roughness of a series of films grown at 300°C from 60 nm to 1 μm in thickness. The 4x4 μm topography and error mode images in Figure 4.7 show an increase in surface roughness from 4.1 nm for a 60 nm thick film to 17.6 nm for a 1 μm thick film. Line scans determined that the lateral dimension of the surface features increased from approximately 0.14 μm for the 60 nm thick film to approximately 1 μm for the 1 μm thick film. The size of the secondary surface features on the 1 μm thick film is approximately 0.16 μm. Many of these surface features appear to be aligned with the (001) direction.

Substrate temperature effects We used TEM and RHEED to characterize the crystallinity of films grown at 50:1 hydrogen dilution and temperatures between 300–475°C in the 50 nm–2 μm thickness regime and observed four phases of growth. The epitaxial phase was observable only by TEM at thicknesses below 50 nm (Figure 4.4); the twinned epitaxial, mixed and polycrystalline phases were observable by TEM (Figure 4.5 and RHEED as illustrated in Figure 4.8. From this data, we derived the phase diagram in Figure 4.9. At 300°C, the predominant phases are epitaxial and twinned, with a transition to mixed phase or polycrystalline growth occuring somewhere between 1 and 2 μm of growth. As temperature increases, the epitaxial and twinned phases no longer persist

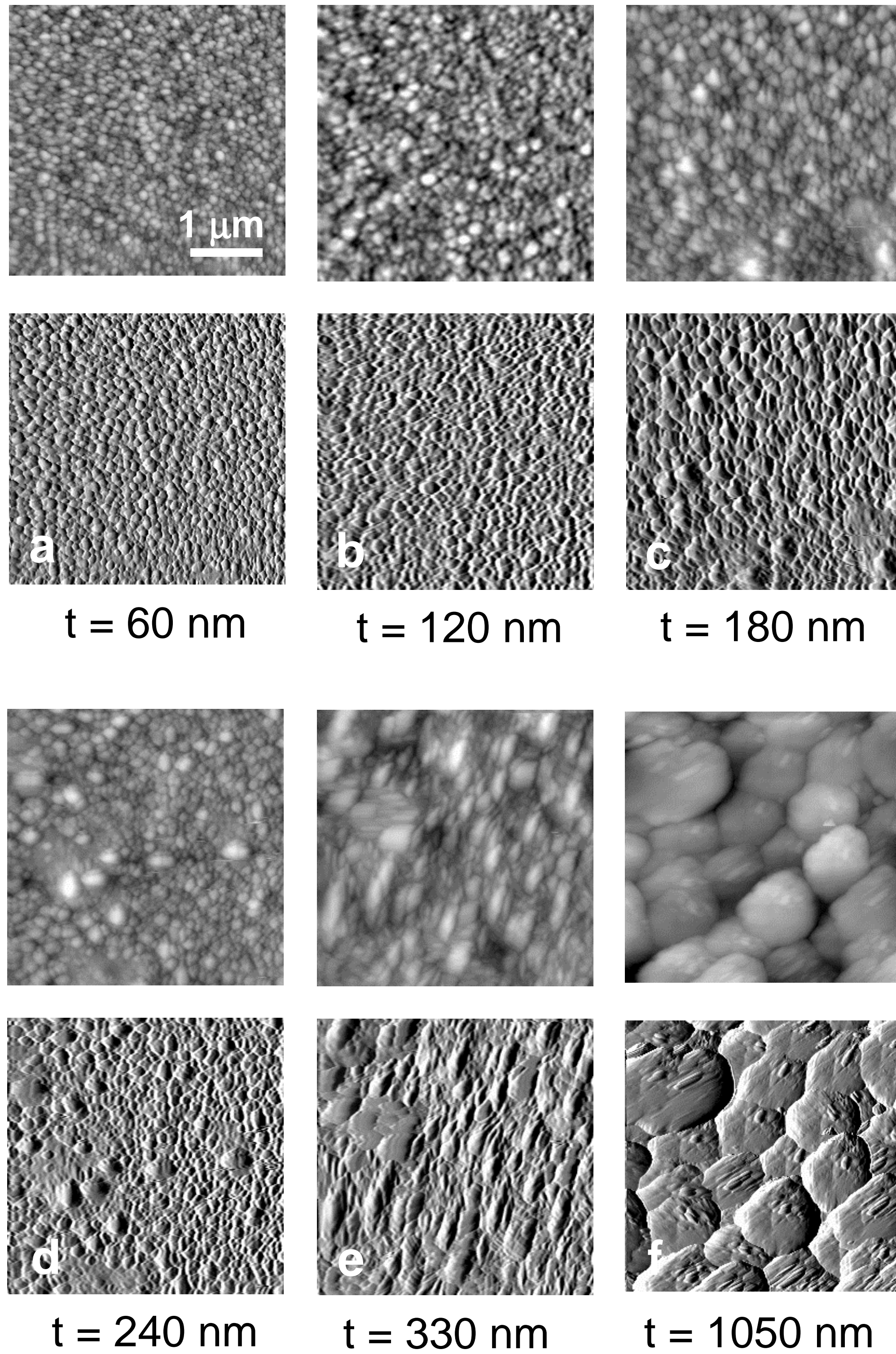

Figure 4.7: 4x4 μm AFM topography (top panels) and error mode (bottom panels) images of films of increasing thickness grown at 300°C.

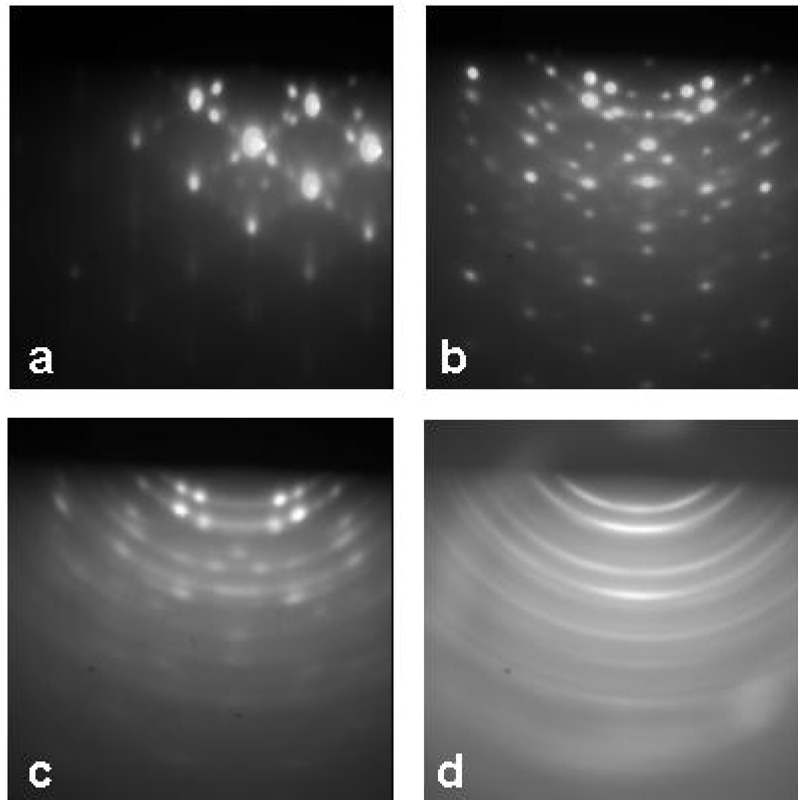

Figure 4.8: Phases of crystalline growth observable by RHEED. (a) 300°C, 60 nm thick twinned epitaxial film. (b) 300°C, 330 nm thick twinned epitaxial film; increased surface roughness is responsible for the differences from (a). (c) 475°C, 60 nm thick film of mixed phase; both spots (corresponding to twinned epitaxial growth) and rings (corresponding to polycrystalline growth) are evident. (d) 475°C, 330 nm thick polycrystalline film.

and the transition to mixed phase or polycrystalline growth occurs at smaller film thicknesses.

4.3.3 Discussion

The results reported here for hydrogen-diluted epitaxial growth on Si(100) are broadly consistent with work reported elsewhere. Theisen et al. observed epitaxial growth with stacking fault defects at temperatures between 195 and 325°C [46], while Seitz and Schröder observed no stacking faults or surface roughening in their epitaxial films grown between 280 and 360°C [67]. Both experiments were done using approximately 10 mTorr of pure SiH_4 and no additional hydrogen. Although Thiesen et al. postulate that the reason that low-temperature epitaxy by HWCVD is possible because the growth species is SiH_3, we believe that for our dilute silane conditions the dominant growth species are silicon atoms [77].

Kitagawa et al. [75] report that, at 430°C, the critical thickness h_{epi} for Si epitaxy by PECVD

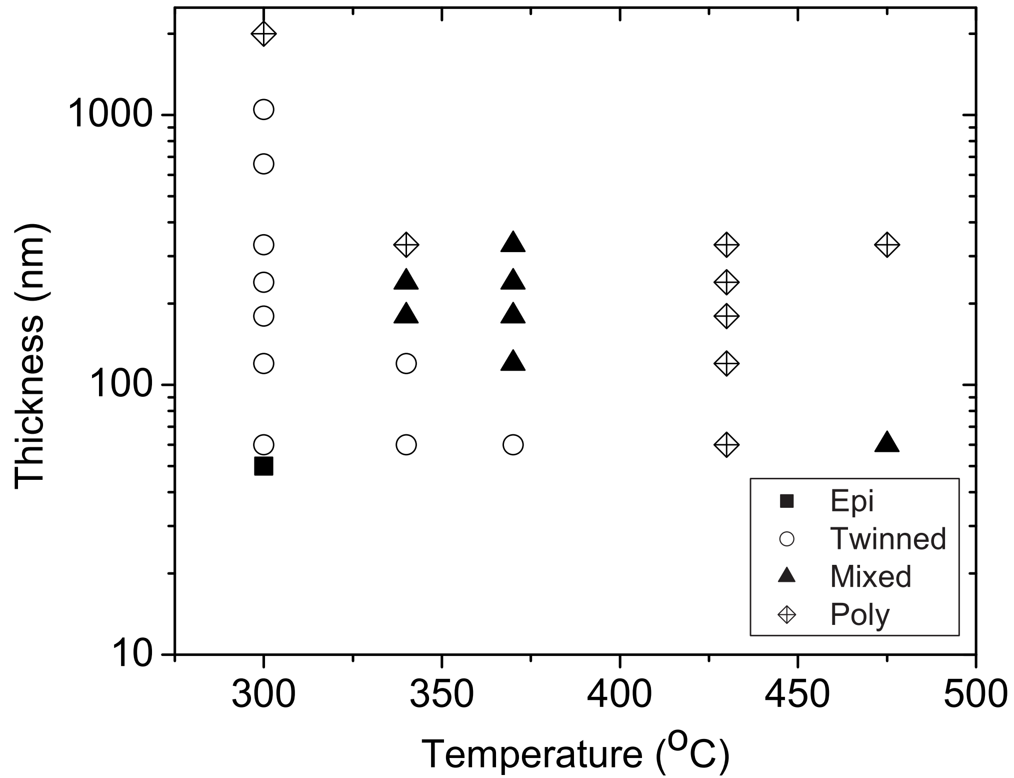

Figure 4.9: Phase diagram of HWCVD films grown at 50:1 hydrogen dilution.

increases monotonically with hydrogen dilution at constant pressure, while at 120°C, there is an optimal hydrogen dilution which produces the greatest value of h_{epi}. Kondo et al. [74] propose a model for epitaxial growth in atomic hydrogen-rich processes in which h_{epi} depends on the homogeneous surface hydrogen coverage of the Si(100) surface. At high temperatures, Si(100) undergoes a 2×1 reconstruction with monohydride coverage [2]. The thermal desorption rate of hydrogen is high, and thus a high flux of atomic hydrogen is required to maintain this hydrogen coverage. At low temperatures, the Si(100) surface displays a 1×1 dihydride reconstruction. Here, it is thought that a flux of atomic hydrogen which is too high may lead to the abstraction of surface hydrogen and the formation of a monohydride surface. Therefore, a balance between the thermal desorption of hydrogen from the surface and the atomic hydrogen flux density is required for the persistence of epitaxial growth.

We consider a model for the thermal desorption of hydrogen proposed by Flowers et al. [87] in which the overall rate of change of the fractional coverage Θ of the Si(100) surface during temperature-programmed desorption can be determined by considering the Si(100) surface as an

ensemble of 1×1 and 2×1 lattice sites which are occupied by indistinguishable hydrogen atoms. θ_{00}, θ_{10}, θ_{11} and θ_2 represent the fractional coverages of unoccupied dimers, singly occupied dimers, doubly occupied dimers, and dihydride species, respectively. It must be true that

$$\theta_{00} + \theta_{10} + \theta_{11} + \theta_2 = 1 \tag{4.2}$$

and

$$\frac{1}{2}\theta_{10} + \theta_{11} + 2\theta_2 = \Theta \tag{4.3}$$

If a quasi equilibrium state for the reactions

$$\text{H-Si-Si-H} + \text{Si=Si} \rightleftharpoons 2\text{H-Si-Si} \tag{4.4}$$

and

$$\frac{3}{2}\text{H-Si-Si-H} \rightleftharpoons \text{H-Si-Si}\cdot + \text{H-Si-H} \tag{4.5}$$

is assumed, the distribution of surface species can be calculated from their vibrational partition functions. If the only significant differences in vibrational partition functions for the surface groups are due to Si-H vibrations then the equilibrium between surface species can be described by

$$\frac{\theta_{10}^2}{\theta_{00}\theta_{11}} = \frac{4Q_{10}^2}{Q_{11}} \exp\left(-\frac{\epsilon_1}{kT}\right) \tag{4.6}$$

$$\frac{\theta_{10}\theta_2}{\theta_{11}^3(1+\theta_2)^{\frac{1}{2}}} = \frac{Q_{10}Q_2}{(Q_{11}^3)^{\frac{1}{2}}} \exp\left(-\frac{\epsilon_2}{kT}\right) \tag{4.7}$$

where the Q's represent the vibrational partition functions for surface species

$$Q = \prod_i \frac{\exp(-\frac{\nu_i}{kT})}{\sum_j \exp-(\frac{\nu_j}{kT})}. \tag{4.8}$$

The Si-H vibrational frequencies can be obtained from published data. By solving Equations 4.2, 4.3, 4.6 and 4.7 for a particular hydrogen coverage and surface temperature, the equilibrium distributions of all surface species on Si (100) can be calculated.

Considering adsorption, abstraction and thermal desorption of hydrogen from the surface, the rate of change of the surface hydrogen coverage on Si(100) during HWCVD growth at a specific temperature is given by

$$\frac{d\Theta}{dt} = \left.\frac{d\Theta}{dt}\right|_{\text{adsorption}} + \left.\frac{d\Theta}{dt}\right|_{\text{abstraction}} + \left.\frac{d\Theta}{dt}\right|_{\text{desorption}} \tag{4.9}$$

Table 4.1: Parameters used in hydrogen surface coverage model.

Parameter	Value	Reference
ν_a	2×10^{1}5 s^{-1}	[89]
E_a	57.2 kcal/mol	[89]
ν_b	3.2×10^{1}3 s^{-1}	[90]
E_b	43 kcal/mol	[87]
ϵ_1	6.0 kcal/mol	[89]
ϵ_2	19 kcal/mol	[87]
H-SiSi stretch	2093 cm^{-1}	[87]
H-SiSi bend	621 cm^{-1}	[91]
H-Si-Si-H sym. stretch	2088 cm^{-1}	[92]
H-Si-Si-H asym. stretch	2099 cm^{-1}	[92]
H-Si-H deformation	637 cm^{-1}	[91]
H-Si-H sym. stretch	2091 cm^{-1}	[93]
H-Si-H asym. stretch	2104 cm^{-1}	[93]
H-Si-H scissors	910 cm^{-1}	[90]
P_{ads}	0.6	[94]
E_{ads}	0.1 kcal/mol	[95]
P_{abs}	0.52	[96]
E_{abs}	2.0 kcal/mol	[97]

where

$$\left.\frac{d\Theta}{dt}\right|_{\text{adsorption}} = \Phi_H P_{ads} \exp\left(-\frac{E_{ads}}{kT}\right)(2-\Theta), \tag{4.10}$$

$$\left.\frac{d\Theta}{dt}\right|_{\text{abstraction}} = \Phi_H P_{abs} \exp\left(-\frac{E_{abs}}{kT}\right)\Theta, \tag{4.11}$$

and

$$\left.\frac{d\Theta}{dt}\right|_{\text{desorption}} = \nu_a \times \theta_{11} \times \exp(-E_a/kT) + \nu_b \times \theta_2^2 \times \exp(-E_b/kT) \tag{4.12}$$

as before.

The reaction constants ν_a and ν_b and activation energies E_a and E_b, as well as parameters for the adsorption probability $P_{ads}\exp(-E_{ads}/kT)$ and abstraction probability $P_{abs}\exp(-E_{abs}/kT)$ are also found in the literature. A comprehensive list of parameters used in the model are listed in Table 4.3.3. The flux of hydrogen at the surface Φ_H can be determined from equation 4.1 as before. The cracking probabilities of SiH_4 and H_2 on the wire are taken as 0.7 and 0.14, respectively [88].

By setting equation 4.9 equal to zero, we can determine the equilibrium surface coverage of Si(100) during HWCVD growth as a function of temperature under various growth conditions. At low temperatures, thermal desorption is negligible and a balance is reached between adsorption and

abstraction of hydrogen. At high temperatures, thermal desorption becomes more significant. The calculated equilibrium surface coverages for our initial and revised growth conditions are plotted in Figure 4.10, with the experimental equilibrium surface coverage data of Gates and Kulkarni [2] for temperature-programmed desorption given for comparison. Under HWCVD growth conditions the equilibrium surface coverage is higher than that which would be reached if thermal desorption were the only mechanism affecting the hydrogen coverage.

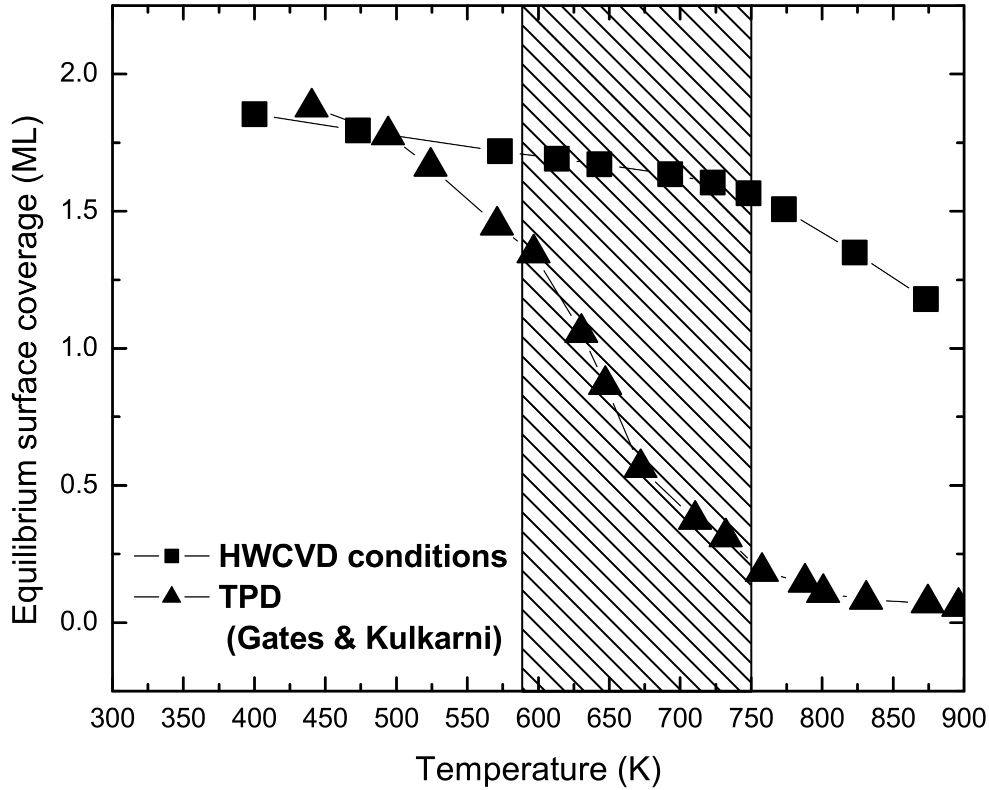

Figure 4.10: Calculated equilibrium surface hydrogen coverages for HWCVD growth conditions (H_2:SiH_4=50:1, 25 mTorr 4% SiH_4 in He, wire 2.5 cm from substrate), with experimental temperature-programmed desorption data [2] for comparison. The shaded area represents the temperature regime in which HWCVD growth experiments were performed.

We hypothesize that the incorporation of contaminants, i.e., oxygen adsorption, contributes to epitaxial breakdown. When the ratio of silicon to oxygen deposition is highest, the greatest h_{epi} may be achieved, although the exact correspondence between h_{epi} and the silicon to oxygen ratio is unknown. The oxygen flux Φ_{O_2} at the substrate can also be determined using equation 4.1 using the mass of molecular oxygen and the substrate temperature; the partial pressure of oxygen in the

chamber is approximately 1×10^{-7} Torr at a base pressure of 5×10^{-7} Torr. The oxidation rate at the equilibrium surface coverage for a given temperature is

$$\left.\frac{d\Theta}{dt}\right|_{\text{oxidation}} = \Phi_{O_2} P_{ox}\left(\theta_{00} + \frac{1}{2}\theta_{10}\right) \tag{4.13}$$

where $P_{ox} = 0.01$ and is roughly temperature-independent [98].

Starting with an initial surface coverage dependent only on the substrate temperature, we use the model to compute the amount of oxygen deposited during the growth of the first monolayer of silicon for a given growth temperature as a function of dilution ratio R ($R=H_2/SiH_4$) at constant pressure, assuming that all silicon atoms incident on the substrate contribute to growth regardless of hydrogen coverage.

Figure 4.11 shows that the silicon to oxygen ratio decreases with temperature for temperatures between 571 K and 711 K. This may explain the decrease in epitaxial thickness with temperature in our experiments (Figure 4.9). At low temperature, the equilibrium surface coverage is high and the fraction of empty sites at which oxidation can occur is low, while at high temperature, the initial equilibrium surface coverage is low, which provides more empty sites for oxidation, although the oxidation rate decreases slightly with temperature. At each temperature, there also appears to be an optimal dilution at which the ratio of silicon to oxygen deposition is a maximum. At low dilution, a monolayer of silicon is deposited more rapidly, but at the same time, there is less atomic hydrogen to fill the empty sites on the surface. At high dilution, the empty sites are filled more quickly by atomic hydrogen, but silicon deposition is slow, leading to a smaller silicon to oxygen ratio.

The model does not take into account gas-phase reactions in the chamber, nor does it include the effects of etching. Including detailed gas phase reactions would likely decrease the flux of atomic hydrogen, since atomic hydrogen may react with atomic hydrogen or SiH_x to form H_2, and increase the flux of Si by reacting with SiH_x to form Si. This effect is similar to a decrease in dilution ratio R and would shift the optimum dilution ratio to higher R. Including an etching mechanism would decrease the flux of Si at high R. This effect would be similar to increasing R and the optimum dilution ratio would shift to smaller R.

Although the model does not yet quantitatively predict the behavior of our reactor, it may provide a qualitative insight into the data of Kitagawa et al. Based on the results of the model, it is likely that at 430°C there does exist an optimal dilution at which the greatest epitaxial thickness could be reached; it only lies beyond the limits of their experimental data. It is possible that the maximum at 430°C may lie in the etching regime and thus can never be reached.

The dependence of the epitaxial thickness on the silicon to oxygen ratio is difficult to quantify. However, it is known that, during MBE crystal growth, impurities at the growing interface can lead to surface roughening and subsequent epitaxial breakdown through the formation of voids which may

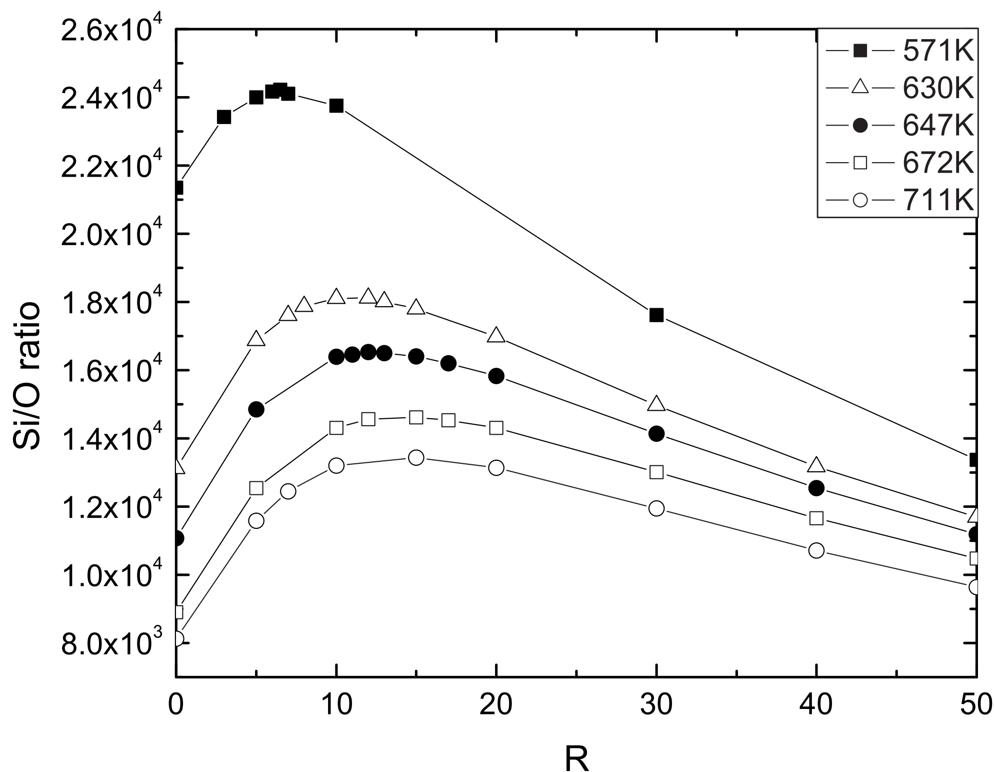

Figure 4.11: Silicon to oxygen ratio in the first monolayer of growth as a function of dilution ratio R (H_2/SiH_4 at temperatures from 571 to 711 K. Pressure is held constant at 75 mTorr of a gas mixture of H_2 and 4% SiH_4 in He.

lead to twinning and surface facets [99]. Although SIMS analysis performed by Evans Analytical, seen in Figure 4.12, indicates that the oxygen content in our films is <1%, we have observed both the formation of twin boundaries in our films and an increase in surface roughness with film thickness, which point to oxygen incorporation as a possible contributory mechanism for epitaxial breakdown in our films.

For our experiments, a decrease in the silicon to oxygen deposition ratio with temperature, as predicted by the model, may explain the observed decrease in epitaxial thickness with temperature. In addition, an increase in substrate temperature and corresponding decrease in hydrogen surface coverage may lower adspecies diffusivity [100], promoting an earlier transition to polycrystalline growth. Further dilution-dependent epitaxial growth experiments would be necessary to completely develop a predictive model of epitaxial growth.

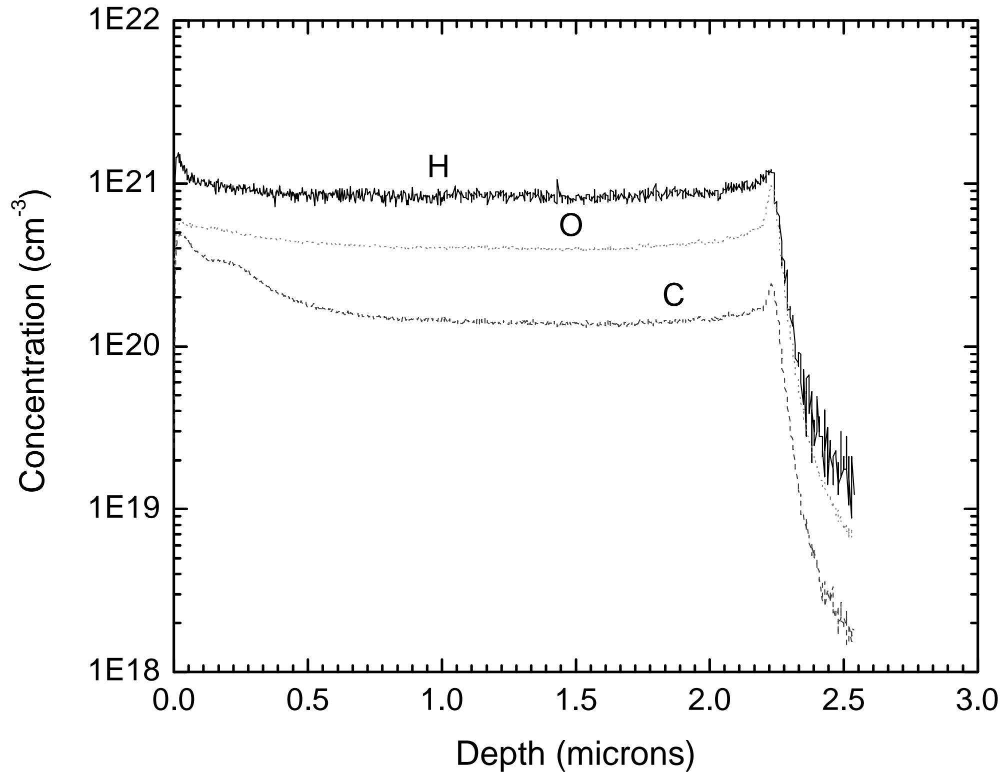

Figure 4.12: Carbon, hydrogen, and oxygen concentrations in 2.2 μm thick film grown at 300°C, as determined by SIMS analysis.

4.4 Epitaxy on large-grained polycrystalline templates

4.4.1 Selective nucleation and solid phase epitaxy

Large-grained polycrystalline layers formed by the selective nucleation and solid-phase epitaxy (SNSPE) process were used as templates for epitaxial growth. To fabricate SNSPE templates, 60 μL of a colloidal "ink" containing 20 μg nickel nanoparticles in 1 mL isopropanol was spun for 20 seconds at 1500 rpm onto a 1000 Åthick phosphorus-doped amorphous Si layer on SiO_2, leaving a randomly distributed array of nanoparticles. During a subsequent vacuum anneal at 600°C, the nanoparticles serve as heterogeneous nucleation sites for grain growth. The resulting polycrystalline films have grain sizes on the order of 100 μm with low-angle grain boundaries. A schematic of the SNSPE process is shown in Figure 4.13. More details can be found in reference [3]. Optical micrographs of the crystallization process over a period of 10 hours are shown in Figure 4.14.

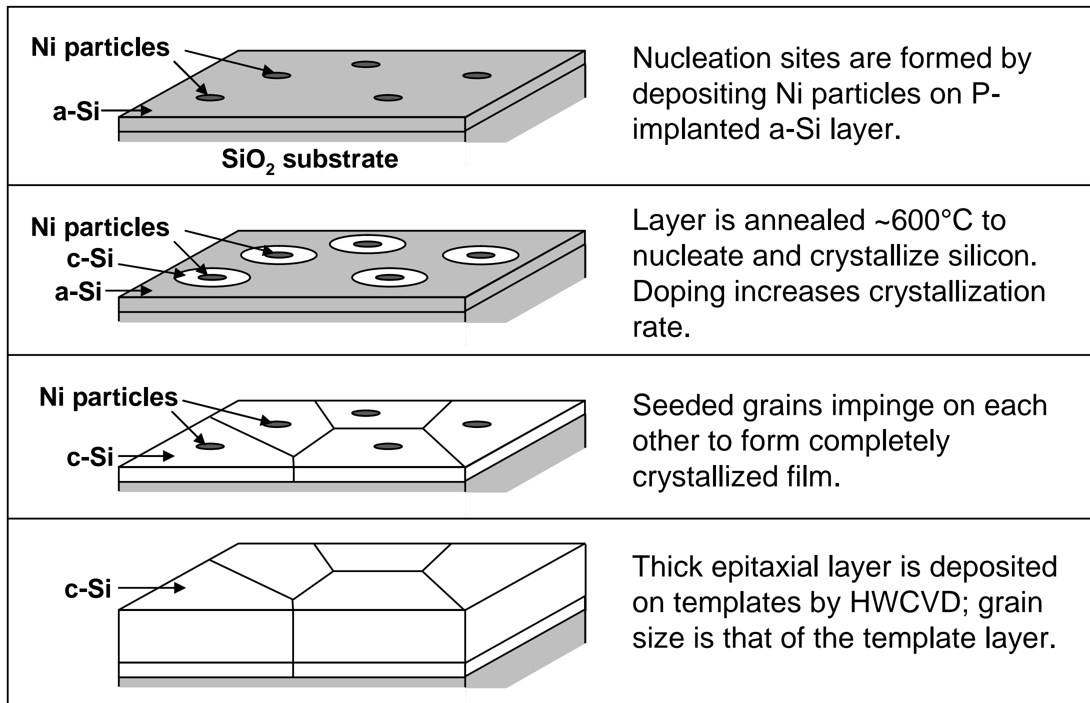

Figure 4.13: The SNSPE template fabrication process.

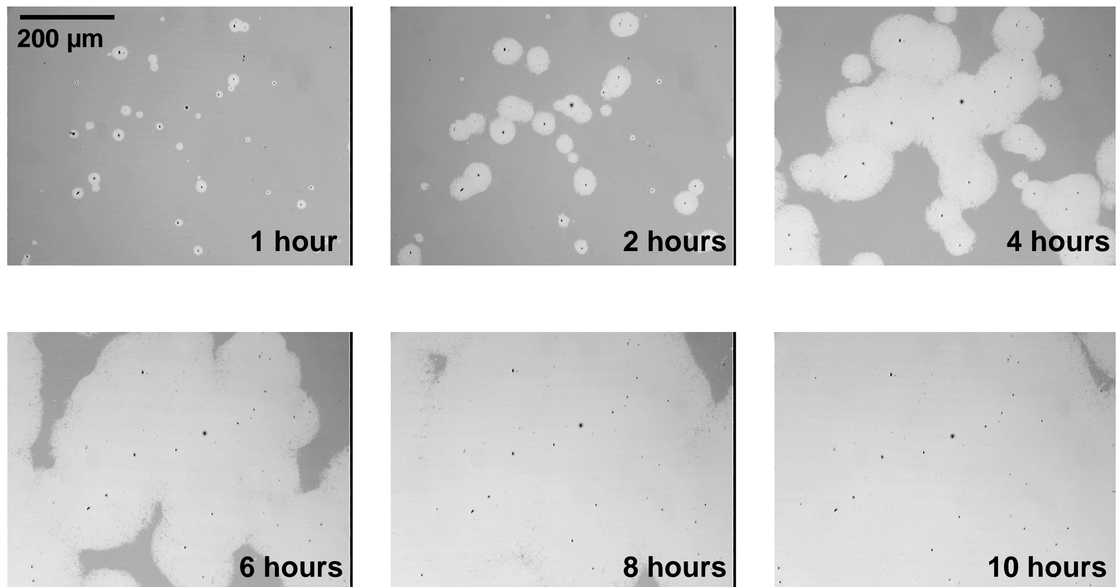

Figure 4.14: Crystallization of SNSPE template layer [3]. The black dots are the nickel nanoparticles; the white areas are grains of crystalline silicon and the grey areas are amorphous silicon regions.

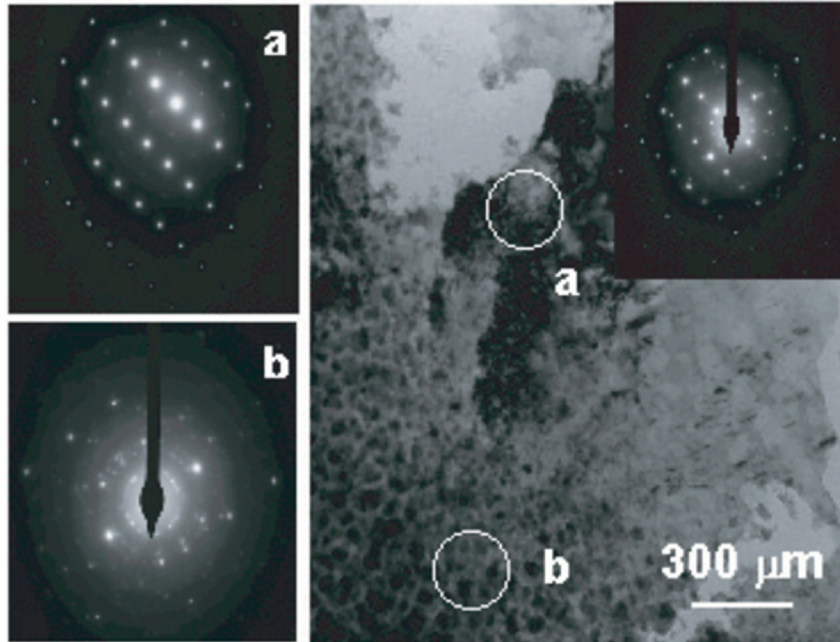

Figure 4.15: Plan-view TEM of HWCVD epitaxial film (T=300°C) on SNSPE template. (a) Selected area diffraction pattern from underlying SNSPE template. (b) Selected area diffraction pattern from HWCVD film on SNSPE template. (c) Bright-field image indicating selected area diffraction regions. Inset: diffraction from entire area.

4.4.2 Results

Silicon films 300 nm thick grown on SNSPE templates under the initial growth conditions were investigated through plan-view TEM. The results, shown in Figures 4.15 and 4.16, are consistent with low-temperature epitaxy on the scale of the 100-μm grains of the SNSPE templates. Epitaxial breakdown is observed in the diffraction pattern of the HWCVD film, but some of the underlying low-order diffraction spots are visible. The underlying film therefore likely has a morphology similar to that of the HWCVD films on Si(100) [Figures 4.1 and 4.2]. The effect of the orientation of the underlying grain structure of the SNSPE template on the morphology of the HWCVD film is shown in Figure 4.16.

Cross-sectional analysis of these films reveals some areas of epitaxial growth as well as some areas of columnar growth. Before HWCVD growth, the SNSPE templates were cleaned in a solution of 3:7 HNO_3:H_2O, which has been shown by Auger spectroscopy to remove elemental nickel from the template surface[69]. The lack of epitaxy in some areas is thus more likely to have been caused by the presence of ordinary surface contaminants, such as carbon and oxygen, than by the nickel nanoparticles.

Cross-sectional analysis of 3.5 μm thick films grown on SNSPE templates under the revised growth conditions also revealed some areas of epitaxy, as seen in Figure 4.17 (a) and (b). Because

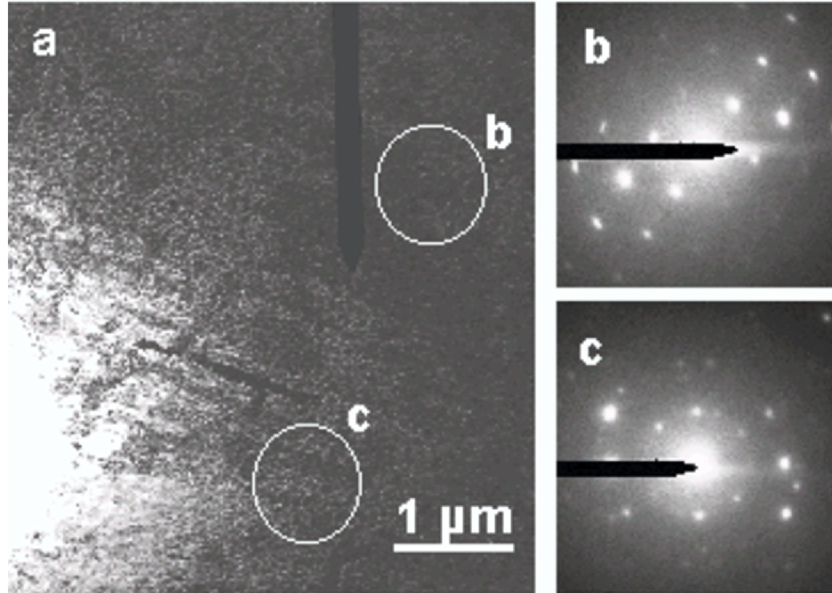

Figure 4.16: (a) Bright-field image of HWCVD film (T=300°C) on SNSPE template showing selected area diffraction regions. (b) Selected area diffraction from HWCVD film on (100)-oriented grain. (c) Selected area diffraction from HWCVD film on a grain of different orientation.

the grains of the SNSPE template are large compared to the TEM viewing region and possess a high intragranular defect density also observable in the films (Figure 4.17 (c) and (d)), it is difficult to determine what constitutes a grain of the template. The diffraction pattern in the inset of Figure 4.17(a) was taken using a 0.5 μm selected area diffraction aperture, which allowed for diffraction from the film, template layer, oxide, and a small region of the substrate. The high-intensity spotty rings indicate large-grained polycrystalline growth in the first 100-150 nm of the film, which is also consistent with some areas of epitaxy on the template grains. Further plan-view analysis, such as orientation imaging microscopy, may be able to determine the size of regions which inherit the orientation of the template grains.

4.5 Conclusions

Using TEM and RHEED, we have derived a phase diagram for HWCVD growth of Si on Si(100) at temperatures between 300 and 475°C consisting of epitaxial, twinned epitaxial, mixed twinned epitaxial/polycrystalline and polycrystalline phases in films between 50 nm and 2 μm thick. This phase diagram can be understood within the context of a model in which a balance must be reached between the thermal desorption rate of hydrogen from the surface and the adsorption and abstraction rates of surface hydrogen by atomic hydrogen from the wire; this surface coverage limits the rate of oxidation, which in turn affects the epitaxial thickness. This model can qualitatively explain

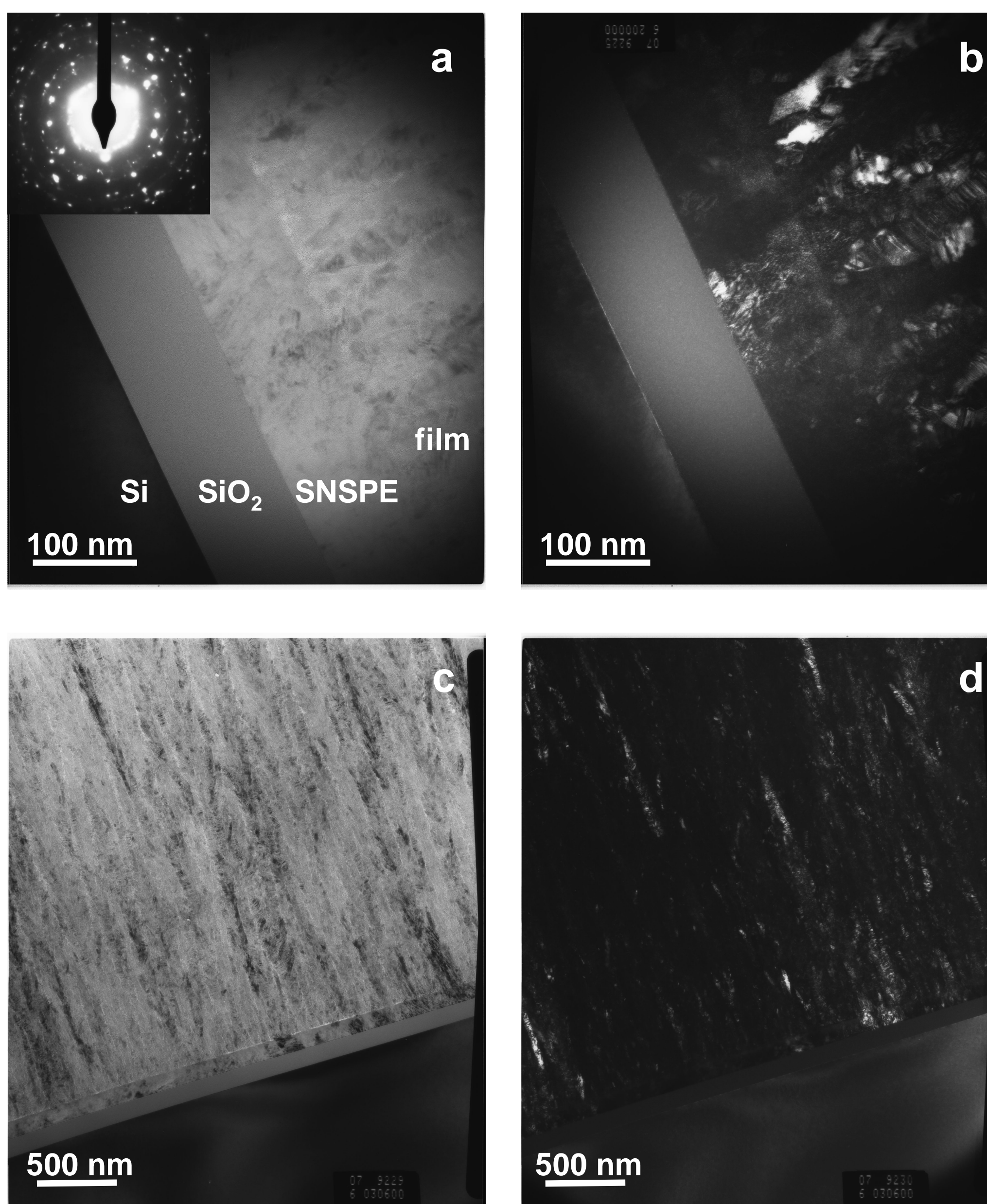

Figure 4.17: (a) Bright-field image of HWCVD film (T=300°C) on SNSPE template showing selected area diffraction region. Inset: selected area diffraction pattern showing areas of large-grained polcrystalline growth. (b) Dark-field image corresponding to region in (a). (c) Bright-field image of 3.5 μm thick film with high intragranular defect density. (d) Dark-field image corresponding to region in (b).

the optimal dilution for the greatest epitaxial thickness at low temperature as well as the increase in epitaxial thickness with dilution at high temperature. Results consistent with epitaxial growth on large-grained SNSPE templates have also been presented, although further analysis, such as orientation imaging microscopy, may be necessary to determine the size of regions which inherit the orientation of the SNSPE template grains.

Chapter 5

Minority Carrier Lifetimes of HWCVD Films

Abstract

We determine the minority carrier lifetimes of nearly-intrinsic films 1.5-15 μm thick grown by HWCVD at 300°C on Si(100) and SNSPE templates through resonant-coupled photoconductive decay (RCPCD) measurements. Although the microstructure of these films is mostly microcrystalline, the lifetimes for films on Si(100) range from 5.7 to 14.8 μs while those for films on SNSPE templates range from 5.9 to 19.3 μs. Residual nickel present in the SNSPE templates does not significantly affect the lifetime of films grown on SNSPE templates, making the growth of epitaxial layers by HWCVD on SNSPE templates a viable strategy for the fabrication of thin-film photovoltaics. Ongoing work includes time-of-flight measurements of the minority-carrier mobility in these films.

5.1 Introduction

A requirement for the design of thin-film photovoltaics is that the minority carrier diffusion length be greater than the thickness of the active layer. This diffusion length L_d is related to the minority carrier lifetime τ such that $L_d = \sqrt{D\tau}$, where D is the minority carrier diffusion coefficient in the material. Another means of quantifying the electrical performance of photovoltaic materials is the measurement of the mobility-lifetime product $\mu\tau$, which for a given electric field E measures the distance traveled by a free carrier before recombining ($d = \mu\tau E$). Table 5.1 lists values of the electrical properties of intrinsic films grown by HWCVD and PECVD on glass substrates (unless listed otherwise) as reported in the literature.

Table 5.1: Reported electrical properties of intrinsic films.

Material	$\mu\tau$ (cm^2/V)	L_d (μm)	μ (cm^2/V·s)	τ (μs)	Comments	Ref.
HWCVD a-Si	10^{-7}	-	-	-	After light-induced degradation	[101]
HWCVD a-Si on c-Si	-	-	-	16	Surface-passivated	[102]
HWCVD μc-Si	-	-	2.8	.002-.003	-	[103]
HWCVD μc-Si	-	0.334	-	-	-	[104]
HWCVD μc-Si	10^{-7}	-	-	-	-	[105]
HWCVD μc-Si	10^{-8}	-	10-15	-	Hall mobility	[106]
PECVD μc-Si	-	1.2	-	-	Pulsed PECVD	[107]
PECVD μc-Si	5×10^{-7}	-	-	-	VHF-PECVD	[108]

5.2 Recombination in semiconductors

We seek to measure a lifetime for minority carrier recombination in the HWCVD films. For a p-type semiconductor in which we wish to investigate the behavior of the minority electrons, the bulk recombination rate U for excess carriers Δn and Δp created by an excitation source can be written [109]

$$U = A(n - n_0) + B(pn - p_0 n_0) + C_p(p^2 n - {p_0}^2 n_0) + C_n(pn^2 - p_0 {n_0}^2) \tag{5.1}$$

where $n = n_0 + \Delta n$ and $p = p_0 + \Delta p$. Since in a p-type material $n_0 \ll p_0$, and if there is no trapping, $\Delta n = \Delta p$, we can simplify equation 5.1 as follows:

$$U = A\Delta n + B(p_0 + n_0 + \Delta n)\Delta n + C_p({p_0}^2 + 2p_0\Delta n + \Delta n^2)\Delta n + C_n({n_0}^2 + 2n_0\Delta n + \Delta n^2)\Delta n. \tag{5.2}$$

The recombination lifetime is then given by

$$\tau = \frac{\Delta n}{U} = [A + B(p_0 + n_0 + \Delta n) + C_p({p_0}^2 + 2p_0\Delta n + \Delta n^2) + C_n({n_0}^2 + 2n_0\Delta n + \Delta n^2)]^{-1}. \tag{5.3}$$

The second term in equation 5.3 represents band to band radiative recombination, for which the lifetime is inversely proportional to the carrier concentration because both electrons and holes must be present for recombination to occur. Since silicon has an indirect bandgap, radiative recombination is weak. The third and fourth terms represent Auger recombination, a three-carrier process for which the lifetime is inversely proportional to the square of the carrier concentration. It becomes significant only when either the majority carrier or excess minority carrier concentration is very high.

The first term in equation 5.3 represents Shockley-Read-Hall (SRH) recombination[109, 110], which takes place through a two-step transition through a deep level recombination center in the middle of the band gap. This mechanism is always active since there are always impurities or defects in semiconductor materials. For a material with an impurity concentration N_T of energy level E_T, the SRH lifetime is

$$\tau_{SRH} = \frac{\tau_p(n_0 + n_1 + \Delta n) + \tau_n(p_0 + p_1 + \Delta n)}{p_0 + n_0 + \Delta n} \tag{5.4}$$

where τ_n and τ_p are the electron and hole lifetimes, respectively. These can be written in terms of the defect concentration, the thermal carrier velocity and the electron and hole capture cross-sections:

$$\tau_n = \frac{1}{\sigma_n v_{th} N_t} \tag{5.5}$$

$$\tau_p = \frac{1}{\sigma_p v_{th} N_t} \tag{5.6}$$

n_1 and p_1 are defined as

$$n_1 = n_i \exp\left(\frac{E_T - E_i}{kT}\right) \tag{5.7}$$

and

$$p_1 = n_i \exp\left(-\frac{E_T - E_i}{kT}\right). \tag{5.8}$$

Low-level injection (LLI) conditions are present when the excess minority carrier concentration is small compared to the equilibrium majority carrier concentration, $\Delta n \ll p_0$. The lifetime $\tau_{SRH} = \tau_n$ in this case. Under high-level injection (HLI) conditions, $\Delta n \gg p_0$ and the lifetime $\tau_{SRH} = \tau_n + \tau_p$.

5.3 Resonant-coupled photoconductive decay

The resonant-coupled photoconductive decay (RCPCD) technique is a contactless method for measuring minority carrier lifetime developed by Richard Ahrenkiel and Stephen Johnston of NREL in 1998[111]. In this technique, the sample is placed on a movable insulating platform which is positioned at variable distances from a small antenna such that the sample becomes part of a coupled antenna array. The antenna is part of a high-Q tuned circuit, and when the sample is placed near the antenna, the mutual impedance modifies the input impedance of the antenna. This assembly is placed at the center of a highly conducting box reflector. The entire apparatus is enclosed in a larger enclosure that is a resonant cavity at the resonance frequency of the sensor such that the walls of the enclosure become nodes of the rf standing waves and the sample lies at an antinode. Figure 5.1 shows a schematic of the apparatus.

A microwave generator in the 400–900 MHz range is used as a probe; the resulting electromagnetic waves are reflected by free carriers in the semiconductor sample. The sample absorbs and reradiates these primary electromagnetic waves in phase with the driving antenna. The intensity of the reradiated electromagnetic waves depends on the carrier concentration in the sample. A pulsed light source is then used to generate excess carriers, which change the reflection coefficient of the microwave signal. The driving antenna then absorbs the photogenerated electromagnetic waves and transfers the energy into an ac voltage, which is recorded on a digital oscilloscope. This corresponds to the decay in the free carrier concentration in the sample such that

$$V(t) = AZ_{12}^2\Delta_s(t) \tag{5.9}$$

where A is the system gain, Z_{12} is the mutual impedance between the sample and antenna, and $\Delta_s(t)$ is the transient photoconductivity of the sample. When recombination can be written in terms of a single lifetime, the change in photoconductivity is given by

$$\Delta\sigma = q(\mu_n + \mu_p)\Delta n \exp(-t/\tau) \tag{5.10}$$

where τ is the minority carrier lifetime.

The surface recombination velocity S at unpassivated surfaces is also an important consideration. The effective lifetime measured by RCPCD is given by[112]

$$\frac{1}{\tau_{eff}} = \frac{1}{\tau_{SRH}} + \frac{2S}{d} \tag{5.11}$$

where d is the sample thickness. The surface recombination velocity is generally unknown and so the lifetime measured by RCPCD is a lower bound on the true lifetime in the material.

5.4 Experiment

HWCVD films of 1.5, 3.5, 11.5 and 15 μm thicknesses were grown at 300°C on Si(100) and SNSPE templates. Growth of a given film thickness on Si(100) and SNSPE templates was performed in the same experiment. The Si(100) substrates were p-type with resistivity 100 Ω·cm; the SNSPE templates were degenerately doped n-type (n=10^{20}). Films were nearly intrinsic (p=10^{12}) as determined by spreading resistance analysis (performed by Solecon Labs). As we saw in Chapter 4, epitaxial growth at 300°C persists to a thickness of between 1 and 2 μm, so the microstructure of thick films was primarily microcrystalline.

A lower wire temperature of 1750°C was used to minimize W incorporation into the films. SIMS analysis performed by Evans Analytical Group, seen in Figure 5.2, showed bulk W levels of $<1\times10^{17}$ in films grown at 1800°C and $<1\times10^{16}$ in films grown at 1750°C. (In each case, the W concentration

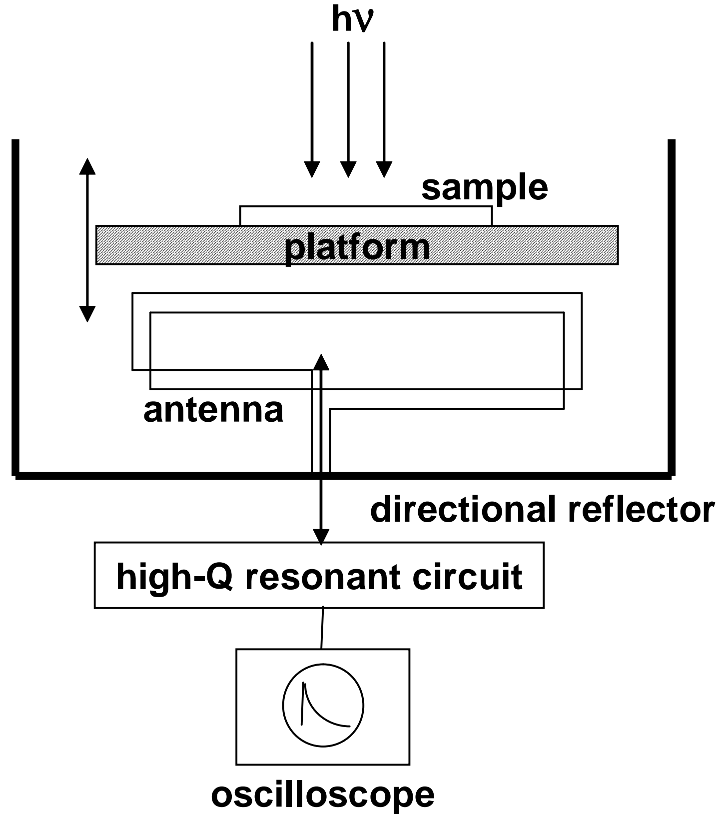

Figure 5.1: Basic schematic of the RCPCD apparatus.

at the surface was an order of magnitude higher than that in the bulk, since exposure to the W wire was necessary to heat the sample to 300°C.)

The minority carrier lifetimes of these films were measured by RCPCD, using a 532 nm laser as the excitation source. The lowest possible excitation power was used and was too low to be measured; an upper limit on the power is 1 μW which corresponds to approximately 1/10 mJ per 10 ms pulse in a 5 mm spot size. Based on these estimates we can estimate an upper bound on Δp of approximately $1{\times}10^{15}$ cm^{-2}. No effort was made to passivate the film surfaces.

The absorption coefficient of Si at 532 nm is approximately $9{\times}10^{-3}$ cm^{-1}, which gives a penetration depth of approximately 1.1 μm [113], so we can be sure that carrier generation occurs in the films and not in the Si(100) substrate. The lifetime of a Si(100) wafer with no film was also measured for comparison. Because the SNSPE templates are only 100 nm thick, the lifetime of the template layer alone cannot be reliably measured by RCPCD at 532 nm.

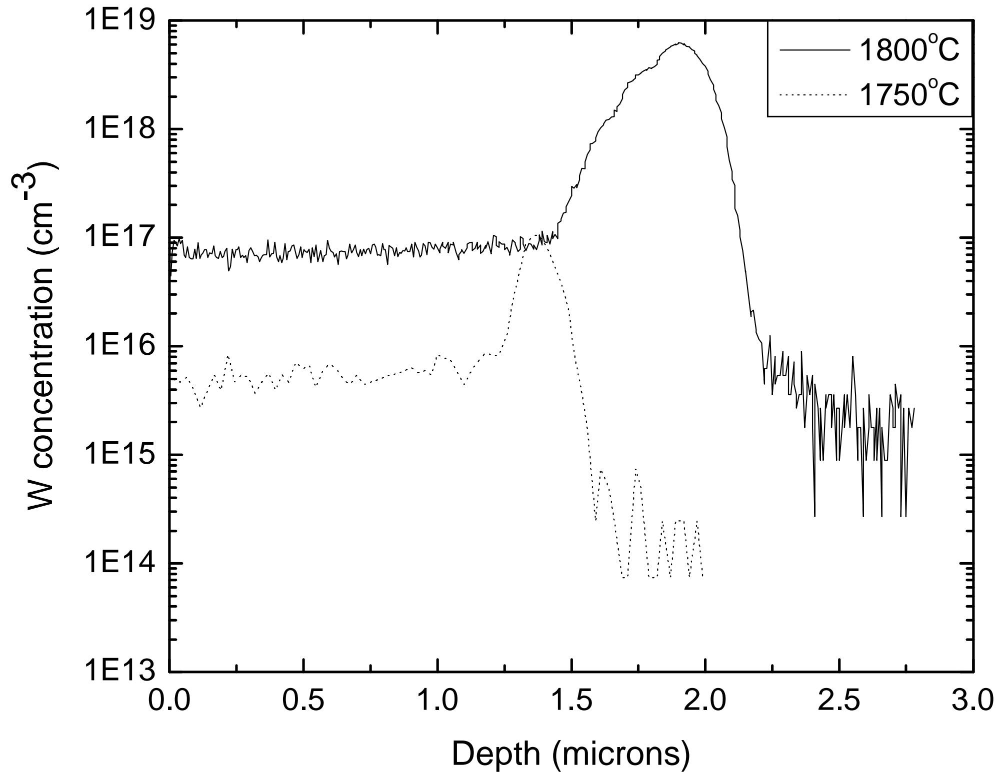

Figure 5.2: W concentration, as determined by SIMS analysis, in 300°C HWCVD silicon films grown on Si(100) at wire temperatures of 1800°C and 1750°C. The higher W concentration at the surface of both films is due to exposure to the W wire before growth, which was necessary to heat the samples to 300°C.

5.5 Results

The RCPCD voltage signal as a function of time for each film can be found in Figures 5.3 and 5.4. One or more exponential decays were fit to the curves from which the minority carrier lifetimes for each sample under HLI and LLI conditions were derived. The measured minority carrier lifetime is actually an effective lifetime; because the surface recombination velocity is not known, this effective lifetime is a lower bound on the true minority carrier lifetime in the material. The curvature of the data indicates the dominant type of recombination center in each film.

In Figure 5.3(a), the RCPCD data for a 1.5 μm HWCVD film on Si is typical of that for bulk Si, with the HLI lifetime greater than the LLI lifetime. This is consistent with an epitaxial film on Si(100). Under illumination, the charged midgap recombination centers fill up quickly and the rest of the excess carriers fill neutral centers, so that under HLI conditions the dominant process is hole

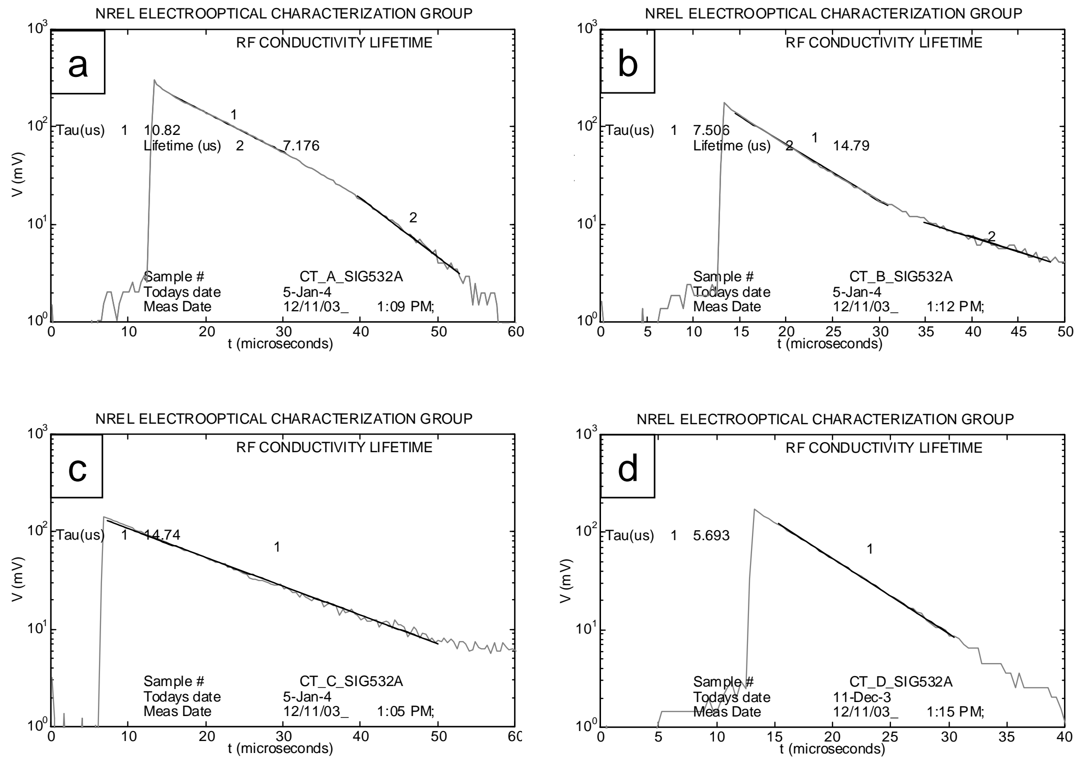

Figure 5.3: RCPCD voltage vs. time curves for HWCVD films of various thicknesses on Si(100). (a) 1.5 μm, (b) 3.5 μm, (c) 11.5 μm, (d) 15 μm. Straight lines indicate exponential decay fits to the data.

capture, which is slower than electron capture. The LLI lifetime then reflects the release of carriers from the midgap recombination centers in the material [114].

In 3.5 μm and 11.5μm thick films on Si(100) (Figure 5.3 (b) and (c)), the HLI lifetime is lower than the LLI lifetime. Such a decay pattern is indicative of a shallow recombination center[114]. Since the microstructure of these thicker films is mostly polycrystalline, hydrogen-passivated grain boundaries may be responsible. For a 15 μm thick film on Si(100) (Figure 5.3(d)), a single decay is observed, corresponding to the LLI lifetime.

The decay patterns of HWCVD films on SNSPE templates, seen in Figure 5.4, have a fast component at the beginning of the illumination. This is likely due to a surface roughness effect; for samples with very rough surfaces, the surface recombination velocity component of the minority carrier lifetime is dominant in the early stages of illumination before the carriers diffuse into the bulk. This feature is less pronounced for the thicker films, which may indicate a decrease in roughness with film thickness.

The decay for the 1.5 μm thick film (Figure 5.4 (a)) indicates a single lifetime, while the decays for 3.5μm and 11.5μm thick films (Figure 5.4 (b) and (c))are characteristic of a deep-level recombination

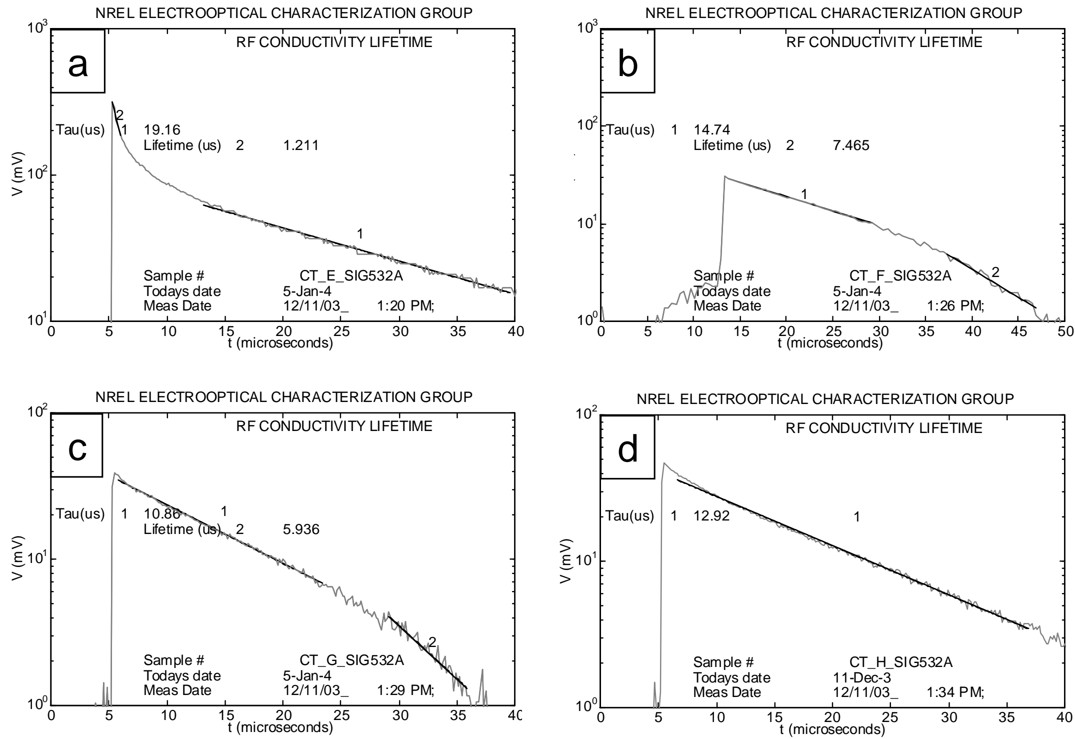

Figure 5.4: RCPCD voltage vs time curves for HWCVD films of various thicknesses on SNSPE templates. (a) 1.5 μm, (b) 3.5 μm, (c) 11.5 μm, (d) 15 μm. Straight lines indicate exponential decay fits to the data.

center. This center may arise from the diffusion of residual nickel from the SNSPE templates into the films. The 15 μm thick film on SNSPE templates is also characterized by a single lifetime. The factor of two discrepancy in lifetime values may be due to nonuniformity in the films, i.e., it may depend on whether a "good" or "bad" region of each film was illuminated. Although nickel is a known lifetime killer even in small concentrations [115], the lifetimes of films on SNSPE templates are comparable to the lifetimes of films on Si(100).

The minority carrier results are summarized in Figures 5.5 and 5.6 for films on Si(100) and SNSPE templates, respectively. Under LLI conditions, the minority carrier lifetimes for films on Si(100) range from 5.7 to 7.5 μs, and the minority carrier lifetimes for films on SNSPE templates range from 5.9 to 19.3 μs.

Polycrystalline films grown by HWCVD have been used in the fabrication of 1.5 μm-thick thin-film transistors with channel mobilities of 4.7 cm^2/V·s on glass substrates [116]. Using the Einstein relation, we can determine that, if the mobilities in our films were comparable, the minority carrier diffusion coefficient would be 0.1175 cm^2/s. From this value and the minority carrier lifetime of $\sim$7 μs measured by RCPCD in a 1.5 μm thick film on Si(100), we obtain a value for the minority carrier

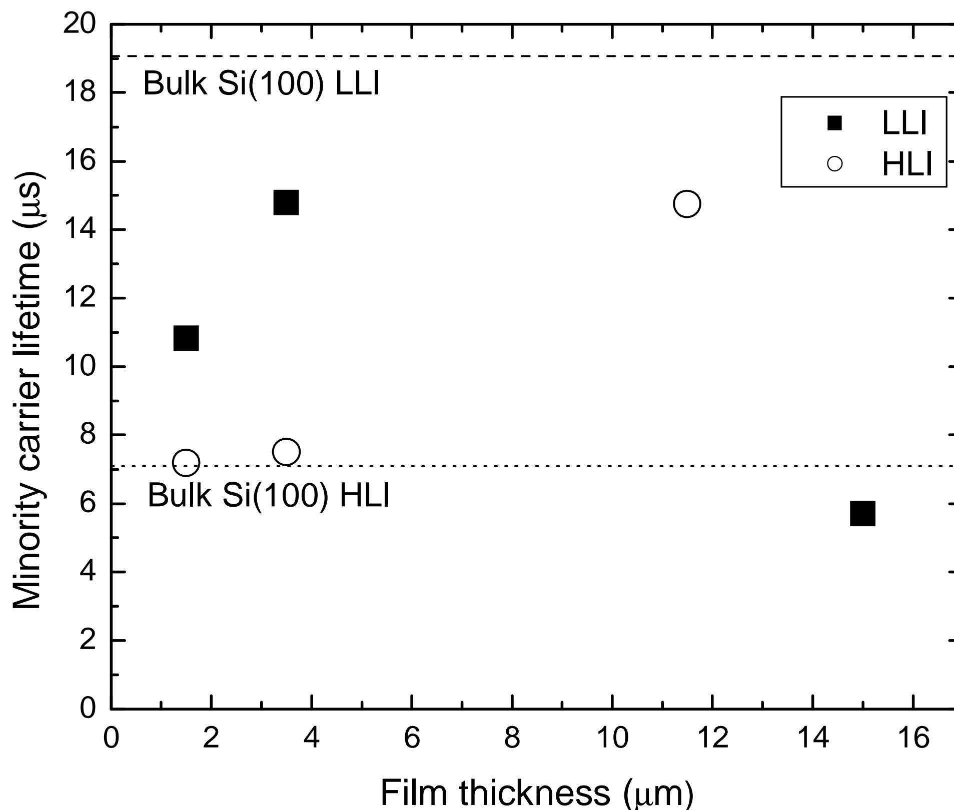

Figure 5.5: LLI and HLI minority carrier lifetimes of HWCVD films on Si(100) as measured by RCPCD. The dashed and dotted lines represent the LLI and HLI lifetimes, respectively, of the bulk Si(100) substrate.

diffusion length of approximately 9 μm, which is comparable to the thicknesses of the active layers for thin-film photovoltaics (1–30 μm). The minority carrier lifetimes of films on SNSPE templates are comparable, making it possible that the growth of epitaxial films by HWCVD on large-grained SNSPE templates is a viable strategy for the fabrication of thin-film photovoltaics.

5.6 Conclusions

The minority carrier lifetimes of nearly-intrinsic epitaxial/microcrystalline films grown on Si(100) by HWCVD range from 5.7 to 7.5 μs. The lifetimes of films grown under the same conditions on SNSPE templates range from 5.9 to 19.3 μs, making them suitable for incorporation into photovoltaic devices. In particular, residual nickel from the SNSPE templates does not appear to be significantly detrimental to the lifetime of films grown on these templates. If the mobilities in these films are

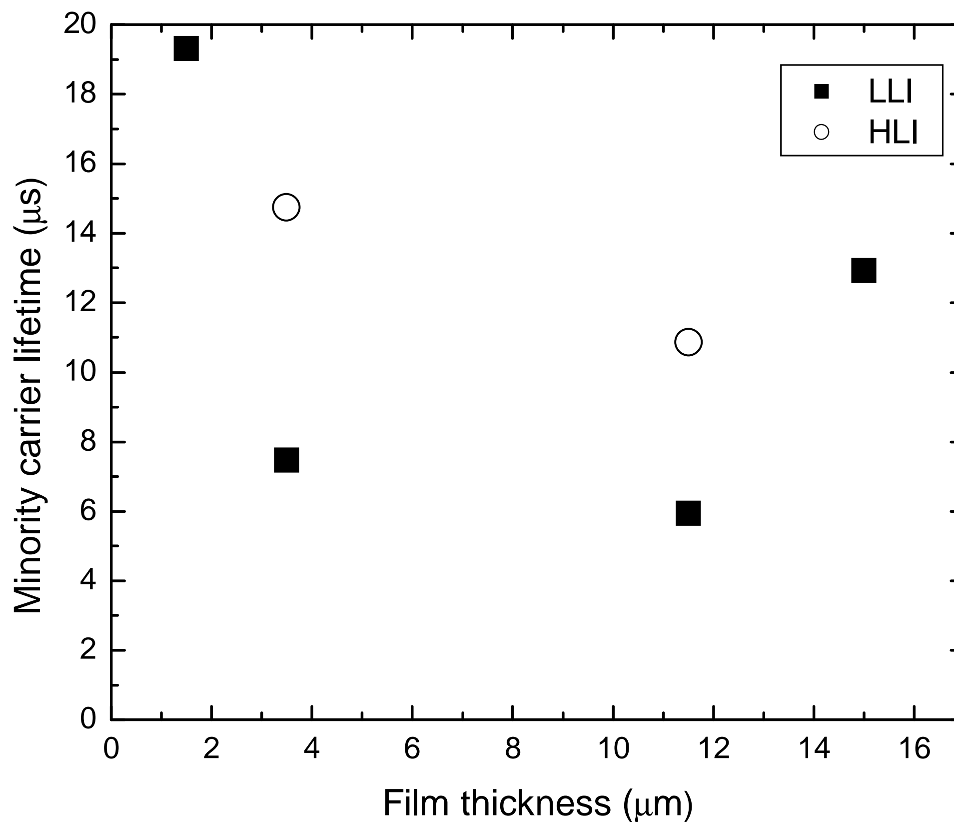

Figure 5.6: LLI and HLI minority carrier lifetimes of HWCVD films on SNSPE templates as measured by RCPCD.

also high, it is possible that HWCVD epitaxy on large-grained SNSPE templates could be a viable strategy for the fabrication of thin-film photovoltaics.

The mobility is an important factor in the determination of material quality for the i-layers of photovoltaic devices. Many experimental data suggest that improvements in the $\mu\tau$ product come from improvements in the mobility [106]. Ongoing work involves time-of-flight measurements of the mobilities in identical films on Si(100) and SNSPE templates to be performed by Eric Schiff and Steluta Dinca at Syracuse University.

Chapter 6

Conclusions and Future Work

We have explored the viability of two strategies for the growth of large-grained polycrystalline films on glass substrates for thin-film photovoltaic applications. First, we consider direct growth on SiO_2. Here, an increase in grain size of continuous polycrystalline silicon films with hydrogen dilution can be attributed to atomic hydrogen etching of silicon monomers, decreasing the nucleation density. Experiments show that the nucleation density increases sublinearly with time at low coverage, implying a fast nucleation rate until a critical density is reached, after which grain growth begins. Through temperature-dependent nucleation-density measurements, the activation energy for diffusion of Si monomers on SiO_2 during HWCVD growth is estimated to be 0.47±0.09 eV. To our knowledge, this is the first estimate for this activation energy given in the literature.

The experimental nucleation density measurements can be understood within the framework of a rate-equation pair-binding simulation. Modelling of the temperature-dependent cluster density measurements give D_0=0.1±0.03 cm^2/s and E_a=0.42±0.01 eV, which is within the error in the experimentally determined value. Monomer etching by atomic hydrogen is simulated by changing the adatom stay time τ_a, and the simulated etch rates vary approximately linearly with H_2 dilution. The model can also be used to explore possible strategies for the rapid growth of large-grained polycrystalline films by HWCVD.

The second strategy involves the use of large-grained polycrystalline layers fabricated on SiO_2 by selective nucleation and solid-phase epitaxy as templates for epitaxial growth by HWCVD. Using TEM and RHEED, we have derived a phase diagram for HWCVD growth of Si on Si(100) at temperatures between 300–475°C consisting of epitaxial, twinned epitaxial, mixed twinned epitaxial/polycrystalline and polycrystalline phases in films between 50 nm and 2 μm thick. This phase diagram can be understood within the context of a model in which a balance must be reached between the thermal desorption rate of hydrogen from the surface and the adsorption and abstraction rates of surface hydrogen by atomic hydrogen from the wire; this surface coverage limits the rate of oxidation, which in turn affects the epitaxial thickness. This model can qualitatively explain the optimal dilution for the greatest epitaxial thickness at low temperature as well as the increase in

epitaxial thickness with dilution at high temperature, although dilution-dependent epitaxial growth experiments must be performed in order to completely develop a truly predictive model for epitaxial growth. Results consistent with epitaxial growth on large-grained SNSPE templates have also been presented, although further analysis, such as orientation imaging microscopy, may be necessary to determine the size of regions which inherit the orientation of the SNSPE template grains.

The minority carrier lifetimes of nearly-intrinsic epitaxial/microcrystalline films grown on Si(100) by HWCVD range from 5.7 to 14.8 μm. The lifetimes of films grown under the same conditions on SNSPE templates range from 5.9 to 19.3 μs, making them suitable for incorporation into photovoltaic devices. In particular, nickel from the SNSPE templates does not appear to be significantly detrimental to the lifetime of films grown on these templates. If the mobilities in these films are also high, it is possible that HWCVD epitaxy on large-grained SNSPE templates could be a viable strategy for the fabrication of thin-film photovoltaics.

Ongoing work involves time-of-flight measurements of the mobilities in identical films on Si(100) and SNSPE templates to be performed by Eric Schiff and Steluta Dinca at Syracuse University. Since the high degree of grain-boundary passivation is thought to enhance the electrical properties of HWCVD films, further experiments may determine a correlation between the lifetimes and mobilities of HWCVD films and grain boundary hydrogen content as determined by fourier-transform infrared spectroscopy (FTIR). The incorporation of these layers into photovoltaic devices is, of course, the ultimate goal.

Bibliography

[1] S.M. Sze. *Physics of Semiconductor Devices.* John Wiley and Sons, 1981.

[2] S. M. Gates and S. K. Kulkarni. *Appl. Phys. Lett.*, 60:53, 1992.

[3] C. M. Chen. PhD thesis, California Institute of Technology, 2001.

[4] E. A. Alsema. Environmental aspects of solar cell modules. Technical Report 96074, Netherlands Agency for Energy and the Environment, Utrecht, The Netherlands, 1996.

[5] DOE/EIA-0219. International energy annual 2000. Technical report, 2002.

[6] E. Becquerel. *Comptes Rendues*, 9:561, 1839.

[7] W. G. Adams and R. E. Day. *Proceedings of the Royal Society*, A25:113, 1877.

[8] Werner von Siemens. *Van Nostrand's Engineering Magazine*, 32:515, 1885.

[9] D. M. Chapin, C. S. Fuller, and G. L. Pearson. *J. Appl. Phys.*, 25:676, 1954.

[10] Vast power is tapped by battery using sand ingredient. *New York Times*, 26 April, 1954.

[11] Sun's energy: Fuel unlimited. *U.S. News and World Report*, 36:18, 1954.

[12] G. Raisbeck. *Scientific American*, 193:102, 1955.

[13] John Perlin. *From Space to Earth: The Story of Solar Electricity.* Harvard University Press, 1999.

[14] D. L. Staebler and C. R. Wronski. *Appl. Phys. Lett.*, 31:292, 1977.

[15] Mary D. Archer and Robert Hill, editors. *Clean Electricity from Photovoltaics.* World Scientific, 2001.

[16] J. Zhao, A. Wang, P. Altermatt, and M. A. Green. *Appl. Phys. Lett.*, 66:3636, 1995.

[17] http://www.sunpower.com.

[18] http://www.bpsolar.com.

[19] W. Warta, J. Sutter, B. F. Wagner, and R. Schindler. In *Proceedings of the 2nd World Conference on Photovoltaic Solar Energy Conference, Ispra*, page 1650, 1998.

[20] M. J. McCann, K. R. Catchpole, K. J. Weber, and A. W. Blakers. *Sol. Energy Mater. Sol. Cells*, 68:135, 2001.

[21] J. H. Werner, S. Kolodinski, U. Rau, J. K. Arch, and E. Bauser. *Appl. Phys. Lett.*, 62:2998, 1993.

[22] J. H. Werner, J. K. Arch, R. Brendel, G. Langguth, M. Konuma, E. Bauser, G. Wagner, B. Steiner, and W. Appel. In *12th European PV Solar Energy Conference, Amsterdam*, 1994.

[23] A. Rohatgi, V. Yelundur, J. Jeong, A. Ebong, M. D. Rosenblum, and J. I. Hanoka. *Sol. Energy Mat. Sol. Cells*, 74:117, 2002.

[24] A. Shah, P. Torres, R. Tscharner, N. Wyrsch, and H. Keppner. *Science*, 25:692, 1999.

[25] http://www.solarbuzz.com.

[26] K. Zweibel. *Prog. Photovolt.*, 3:279, 1995.

[27] Y. Bai, D. H. Ford, J. A. Rand, R. B.Hall, and A. M. Barnett. In *Conf. Record 26th IEEE Photovoltaic Specialists Conf., Anaheim*, page 35, 1997.

[28] K. Yamamoto, M. Yoshimi, Y. Tawada, T. Okamoto, A. Nakajima, and S. Igari. *Appl. Phys. A*, 69:179, 1999.

[29] J. Meier, R. Fluckiger, H. Keppner, and A. Shah. *Appl. Phys. Lett.*, 65:860, 1994.

[30] B. Nelson, E. Iwaniczko, A. H. Mahan, Q. Wang, Y. Xu, and R. S. Crandall. In *Extended Abstract of First International Conference on Cat-CVD (Hot-Wire CVD)*, page 291, 2000.

[31] A. R. Middya, A. Lloret, J. Perrin, J. Huc, J. L. Moncel, J. Y. Parey, and G. Rose. *Mat. Res. Soc. Symp. Proc.*, 377:119, 1995.

[32] A. Ledermann, U. Weber, C. Mukherjee, and B. Schröder. In *Extended Abstract of First International Conference on Cat-CVD (Hot-Wire CVD)*, page 51, 2000.

[33] K. Ishibashi. In *Extended Abstract of First International Conference on Cat-CVD (Hot-Wire CVD)*, page 45, 2000.

[34] C. Voz, D. Peiro, J. Bertomeu, D. Soler, M. Fonrodona, and J. Andreu. *Mat. Sci. Eng. B*, 69:278, 2000.

[35] J. H. Werner, R. Dassow, T. J. Rinke, J. R. Köhler, and R. B. Bergmann. *Thin Solid Films*, 383:95, 2001.

[36] H. Wiesmann, A. K. Ghosh, T. McMahon, and M. Strongin. *J. Appl. Phys.*, 50:3752, 1979.

[37] H. Matsumura and H. Tachibana. *Appl. Phys. Lett.*, 47:833, 1985.

[38] H. Matsumura. *Jpn. J. Appl. Phys.*, 25:949, 1986.

[39] J. Doyle, R. Robertson, G. H. Lin, M. Z. He, and A. Gallagher. *J. Appl. Phys.*, 64:3215, 1988.

[40] A. H. Mahan, J. Carapella, B. P. Nelson, R. S. Crandall, and I. Balberg. *J. Appl. Phys.*, 69:6728, 1991.

[41] W. Jackson and J. Kakalios. *Phys. Rev. B*, 37:1023, 1988.

[42] H. Matsumura. *Jpn. J. Appl. Phys.*, 30:1522, 1991.

[43] M. Heintze, R. Zedlitz, H. N. Wanka, and M. B. Schubert. *J. Appl. Phys.*, 79:2699, 1995.

[44] Akira Heya, Akira Izumi, Atsushi Masuda, and Hideki Matsumura. *Jpn. J. Appl. Phys.*, 39:344, 2000.

[45] C. Niikura, J. Guillet, R. Brenot, B. Equer, J. E. Bourée, C. Voz, D. Peiro, J. M. Asensi, J. Bertomeu, and J.Andreu. *J. Non-Cryst. Sol.*, 266:385, 2000.

[46] J. Thiesen, E. Iwaniczko, K. M. Jones, A. Mahan, and R. Crandall. *Appl. Phys. Lett.*, 79:992, 1999.

[47] S. Bauer, B. Schröder, W. Herbst, and M. Lill. In *Proceedings of the Second World Conference on Photovoltaic Solar Energy Conversion*, page 363, 1998.

[48] U. Weber, M. Koob, R. O. Dusane, C. Mukherjee, H. Seitz, and B. Schröder. In *Proceedings of the European Photovoltaic Solar Energy Conference, Glasgow*, page 286, 2000.

[49] J. Meier, E. Vallat-Sauvain, U. Kroll, S. Dubail, S. Golay, L. Feitknecht, P. Tores, S. Fay, D. Fischer, and A. Shah. *Sol. Energy Mater. Sol. Cells*, 66:73, 2001.

[50] C. Niikura, Y. Poissant, M. E. Gueunier, J. P. Kleider, and J. E. Bouree. *J. Non-Cryst. Sol.*, 299:1179, 2002.

[51] J. K. Rath, A. Barbon, and R. E. I. Schropp. *J. Non-Cryst. Sol.*, 227:1277, 1998.

[52] R. B. Bergmann. *Appl. Phys. A*, 69:187, 1999.

[53] J. A. Venables. *Philos. Mag.*, 27:699, 1973.

[54] H. N. Wanka, R. Zedlitz, M. Heintze, and M. B. Schubert. *Proc. 13th EC PVSEC, Nice*, 428:1753, 1995.

[55] U. Das, S. Morrison, E. Centurioni, and A. Madan. *IEE Proc. Circ. Dev. Sys.*, 150:282, 2002.

[56] H. N. Wanka, R. Zedlitz, M. Heintze, and M. B. Schubert. *Mat. Res. Soc. Symp. Proc.*, 420:915, 1996.

[57] F. Jansen, I. Chen, and M. A. Machonkin. *J. Appl. Phys.*, 66:5749, 1989.

[58] P. Brogueira, V. Chu, and J. P. Conde. *Mat. Res. Soc. Symp. Proc.*, 1997.

[59] M. C. Polo, F. Peiró, J. Cifre, J. Bertomeu, J. Puigdollers, and J. Andreu. *Microsc. Semicond. Mater. Conf. Oxford, Inst. Phys. Conf. Ser.*, 146:503, 1995.

[60] J. Guillet, C. Niikura, J. E. Bourée, J. P. Kleider, C. Longeaud, and R. Bruggemann. *Mat. Sci. Eng. B*, 69:284, 2000.

[61] M. Swiatek, J. K. Holt, D. G. Goodwin, and H. A. Atwater. *Mat. Res. Soc. Symp. Proc.*, 609, 2000.

[62] M. J. Stowell. *Philos. Mag.*, 26:349, 1972.

[63] J. A. Venables. *Phys. Rev. B*, 36:4153, 1987.

[64] W. L. Brown, R. R. Freeman, K. Raghavachari, and M. Schluter. *Science*, 252:1085, 1991.

[65] J. K. Rath, K. F. Feenstra, C. H. M. van der Werf, Z. Hartman, and R. E. I. Schropp. *2nd Intl. PVSEC, Vienna*, 1998.

[66] J. K. Rath, F. D. Tichelaar, H. Meiling, and R. E. I. Schropp. *Mat. Res. Soc. Symp. Proc. Spring 1998*, 1998.

[67] H. Seitz and B. Schröder. *Sol. State Comm.*, 116:205, 2000.

[68] X. Cao. Master's thesis, University of Stuttgart, 2001.

[69] R. A. Puglisi, H. Tanabe, C. M. Chen, and H. A. Atwater. *Mat. Sci. Eng. B*, 73:212, 2000.

[70] D. J. Eaglesham, H. J. Gossmann, and M. Cerullo. *Phys. Rev. Lett.*, 65:1227, 1990.

[71] D. P. Adams, S. M. Yalisove, and D. J. Eaglesham. *Appl. Phys. Lett.*, 63:3571, 1993.

[72] D. J. Eaglesham, G. S. Higashi, and M. Cerullo. *Appl. Phys. Lett*, 59:685, 1991.

[73] J. E. Vasek, Z. Y.Zhang, C. T. Salling, and M. G. Lagally. *Phys. Rev. B*, 51:17207, 1995.

[74] M. Kondo, H. Fujiwara, and A. Matsuda. *Thin Solid Films*, 430:130, 2003.

[75] T. Kitagawa, M. Kondo, and A. Matsuda. *Appl. Surf. Sci.*, 159:30, 2000.

[76] S. Nikzad, S. S. Wong, C. C. Ahn, A. L. Smith, and H. A. Atwater. *Appl. Phys. Lett.*, 63:1414, 1993.

[77] J. K.Holt, M. Swiatek, D. G. Goodwin, R. P. Muller, W. A. Goddard III, and H. A. Atwater. *Thin Solid Films*, 395, 2001.

[78] B. Anthony, L. Breaux, T. Hsu, S. Banerjee, and A. Tasch. *J. Vac. Sci. Technol. B*, 7:621, 1989.

[79] R. E. Thomas, M. J. Mantini, R. A. Rudder, D. P. Malta, S. V. Hattengady, and R. J. Markunas. *J. Vac. Sci. Technol. A*, 10:817, 1992.

[80] Y.-B. Park and S.-W. Rhee. *Appl. Phys. Lett.*, 68:2219, 1996.

[81] A. Izumi and H. Matsumura. *Jpn. J. Appl. Phys.*, 41:4639, 2002.

[82] C. Hopf, A. von Keudell, and W. Jacob. *J. Appl. Phys.*, 94:2373, 2003.

[83] S. Ritchie, S. R. Johnson, C. Lavoie, J. A. Mackenzie, T. Tiedje, and R. Streater. *Surf. Sci.*, 374:418, 1997.

[84] H. Noda, T. Urisu, Y. Kobayashi, and T. Ogino. *Jpn. J. Appl. Phys.*, 39:6985, 2000.

[85] J. F. O'Hanlon. *A User's Guide to Vacuum Technology.* John Wiley and Sons, 1989.

[86] O. P. Karpenko, S. M. Yalisove, and D. J. Eaglesham. *J. Appl. Phys.*, 82:1157, 1997.

[87] M. C. Flowers, N. B. H. Jonathan, Y. Liu, and A. Morris. *J. Chem. Phys.*, 99:7038, 1993.

[88] J. K. Holt, M. Swiatek, D. G. Goodwin, R. P. Muller, W. A. Goddard III, and H. A. Atwater. In *Mat. Res. Soc. Symp Proc. Vol. 664*, 2000.

[89] U. Hofer, L. Li, and T. F. Heinz. *Phys. Rev. B*, 45:9485, 1992.

[90] P. Gupta, V. L. Colven, and S. M. George. *Phys. Rev. B*, 37:8234, 1988.

[91] H. Froitzheim, U. Koler, and H. Lammering. *Surf. Sci.*, 149:537, 1985.

[92] Y. J. Chabal and K. Raghavachari. *Phys. Rev. Lett.*, 53:282, 1984.

[93] Y. J. Chabal and K. Raghavachari. *Phys. Rev. Lett.*, 54:1055, 1985.

[94] U. Hansen and P. Vogl. *Phys. Rev. B*, 57:13295, 1998.

[95] D. D. Koleske, S. M. Gates, and B. Jackson. *J. Chem. Phys.*, 101:3301, 1994.

[96] A. Kutana, B. Makarenko, and J. W. Rabalais. *J. Chem. Phys.*, 119:11906, 2003.

[97] M. C. Flowers, N. B. H. Jonathan, Alan Morris, and Steven Wright. *Surf. Sci.*, 396:227, 1998.

[98] Y. Enta, Y. Takegawa, M. Suemitsu, and N. Miyamoto. *Appl. Surf. Sci.*, 100:449, 1995.

[99] D. J. Eaglesham. *J. Appl. Phys*, 77:3597, 1995.

[100] J. E. Gerbi and J. R. Abelson. *J. Appl. Phys.*, 89:1463, 2001.

[101] E. Morgado. *J. Non-Cryst. Sol.*, 299:471, 2002.

[102] M. R. Page, Q. Wang, T. H. Wang, Y. Yan, S. W. Johnston, and T. F. Ciszek. In *13th Workshop on Crystalline Silicon Solar Cell Materials and Processes*, 2003.

[103] T. J. Savenije, P. A. T. T. van Veenendaal, M. P. de Haas, J. M. Warman, J. K. Rath, and R. E. I. Schropp. *J. Appl. Phys.*, 91:5671, 2002.

[104] J. K. Rath, H. Meiling, and R. E. I. Schropp. *Sol. Energy Mat. Sol. Cells*, page 269, 1997.

[105] R. Bruggemann, J. P. Kleider, C. Longeaud, D. Mencaraglia, J. Guillet, J. E. Bouree, and C. Niikura. *J. Non-Cryst. Sol.*, 266:258, 2000.

[106] A. R. Middya, J. Guillet, J. E. Bouree, J. Perrin, C. Longeaud, and J. P. Kleider. volume 467, page 271, 1997.

[107] J. Cifre, J. Bertomeu, J. Puigdollers, M. C. Polo, J. Andreu, and A. Lloret. *Appl. Phys. A*, 59:645, 1994.

[108] C. Droz, E. Vallat-Sauvain, J. Bailat, L. Feitknecht, J. Maier, X. Niquille, and A. Shah. In *Proceedings of the Third World Conference on Photovoltaic Solar Energy Conversion*, 2003.

[109] W. Shockley and Jr. W. T. Read. *Phys. Rev.*, 87:835, 1952.

[110] R. N. Hall. *Phys. Rev.*, 87:387, 1952.

[111] R. K. Ahrenkiel and S. Johnston. *Sol. Energy Mat. Sol. Cells*, 55:59, 1998.

[112] R. K. Ahrenkiel. *Sol. Energy Mat. Sol. Cells*, 76:243, 2003.

[113] G. E. Jellison and F. A. Modine. *Appl. Phys. Lett.*, 41:180, 1982.

[114] R. K. Ahrenkiel, B. M. Keyes, and S. Johnston. *Surf. Eng.*, 16:1, 2000.

[115] P. Raichoudhury, P. D. Blais, J. R. Davis, R. H. Hopkins, and J. R. McCormick. *J. Elec. Mat.*, 5:435, 1976.

[116] B. Stannowski, J. K. Rath, and R. E. I. Schropp. *Thin Solid Films*, 430:220, 2003.

[117] J. K. Holt. PhD thesis, California Institute of Technology, 2002.

Appendix A

The HWCVD Reactor

This appendix gives further details of the design and construction of the HWCVD reactor used in our experiments.

A detailed diagram of the HWCVD reactor can be seen in Figure A.1, and photographs of the reactor from two different angles can be seen in Figure A.2. The precursor gases (1–4% SiH_4 in He and H_2) are introduced through separate mass flow controllers and mix in a short length of 0.25 inch stainless steel tubing before entering the chamber. The gas pressures are measured with a capacitance manometer which functions in the range from 1 mTorr to 20 Torr. The gas pressures can be varied by controlling the effective pumping speed with a butterfly valve (later replaced by a manual gate valve) at the bottom of the chamber. An ionization gauge measures the base pressure of the chamber, which is typically on the order of 10^{-7} Torr.

For growth over a small sample area, a single tungsten wire is resistively heated with a DC power supply capable of 30 V and 25 A. A tungsten wire of 0.5 mm diameter reaches a temperature of 1850°C at approximately 8 V and 16 A. Large area growth is also possible with a wire array [117]. A linear feedthrough allows precise control of the distance from the wire to the substrate. This feedthrough is not normally mounted on the port where it is shown in Figure A.2 (b), but is located directly opposite the substrate heater, as indicated in Figure A.1.

Figure A.3 shows a top view of the inside of the HWCVD reactor, with the wire and substrate heater visible. The wire is supported by a stainless steel bracket and separated from the bracket by ceramic standoffs. Since copper wire can be corroded by silane, power is delivered through stainless steel wires encased in ceramic beads and terminated in stainless steel compression sleeves which attach to a small set screw around which the wire is wound. A second set of ceramic standoffs are used to keep the wire and power leads in place.

The substrate heater uses a tungsten ribbon filament and is capable of delivering substrate temperatures of up to 500°C. The sample block attaches to the outer ring through a locking pin mechanism. The gear assembly seen in Figure A.3 enables 360 degree rotation of the outer ring and sample block while the heater itself remains stationary. The translatable shutter described in

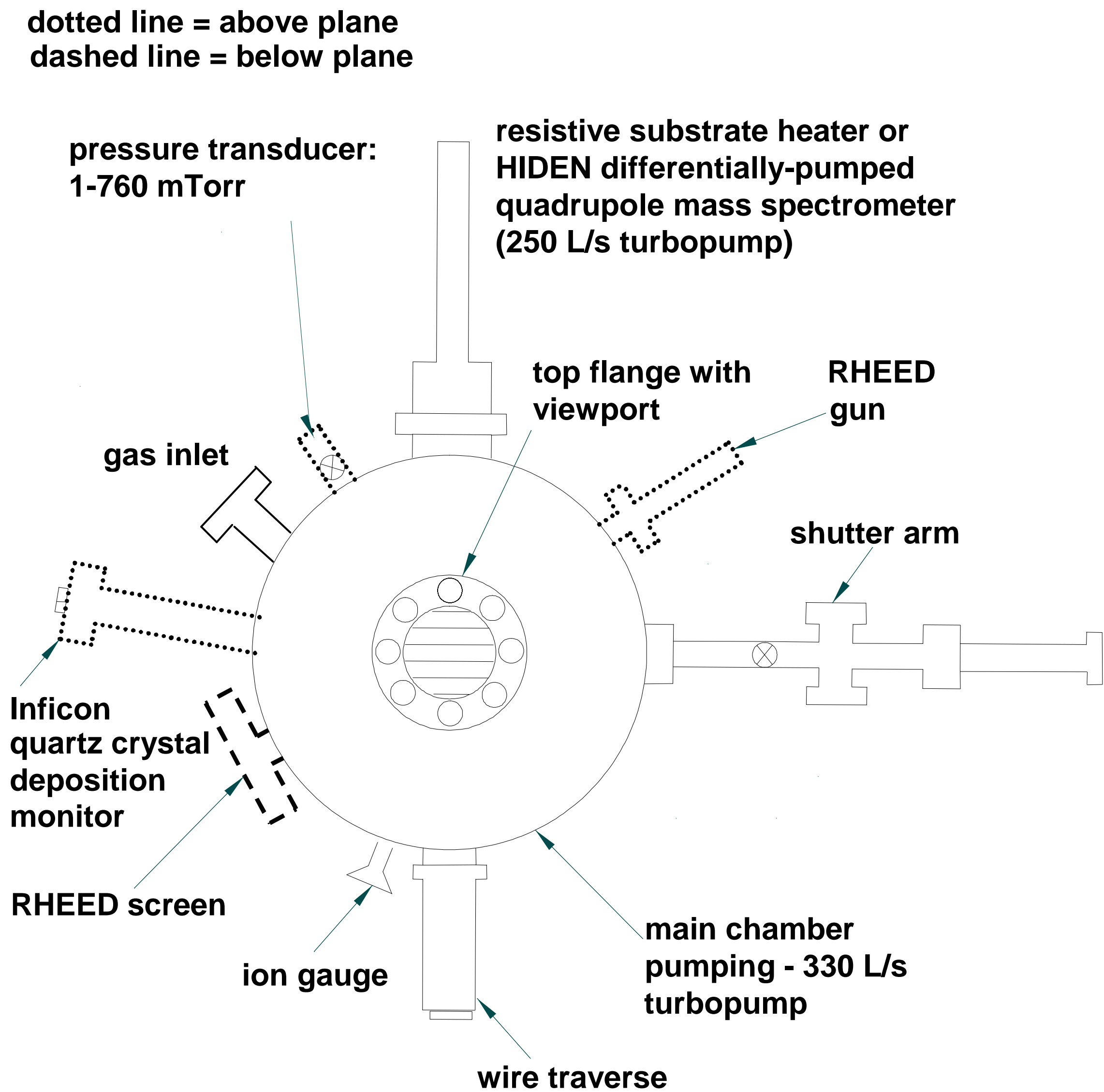

Figure A.1: Schematic of the HWCVD reactor.

Chapter 3 is a thin tantalum plate attached to the load lock transfer arm. Figure A.4 illustrates the wire, substrate and shutter geometry used for all growth experiments.

In principle, with the use of a bellows, the position of the heater can also be translated with respect to the wire. This would enable transfer of samples into the chamber using the load lock and transfer arm; in our experiments, the sample block was manually placed onto the heater assembly through the top viewport. Lateral translation of the heater would also enable in situ RHEED measurements using the electron gun visible in Figures A.1 and A.2, as this translation is necessary to properly align the sample with the electron beam.

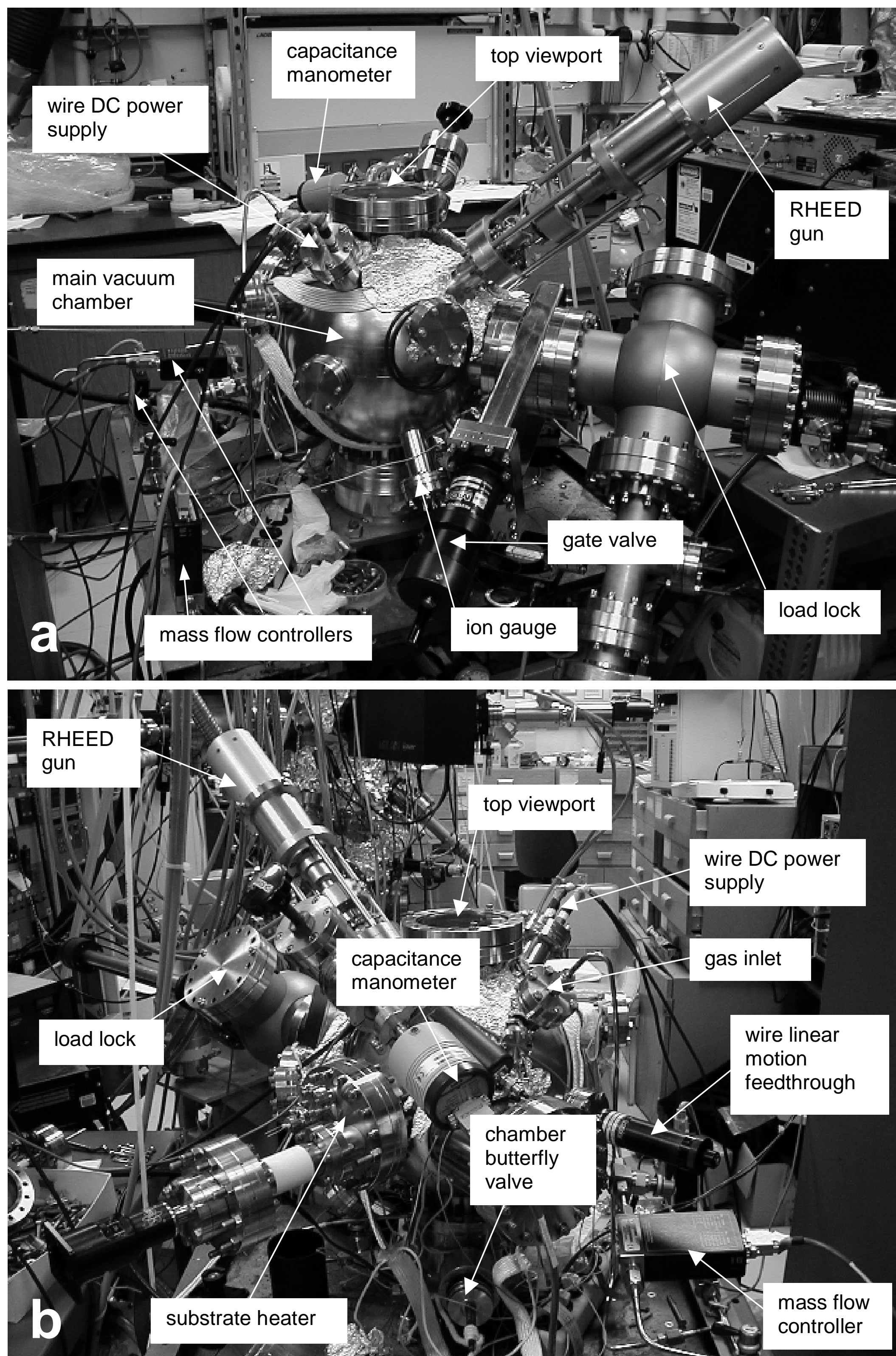

Figure A.2: Photographs of the HWCVD reactor. (a) Front view. (b) Side view.

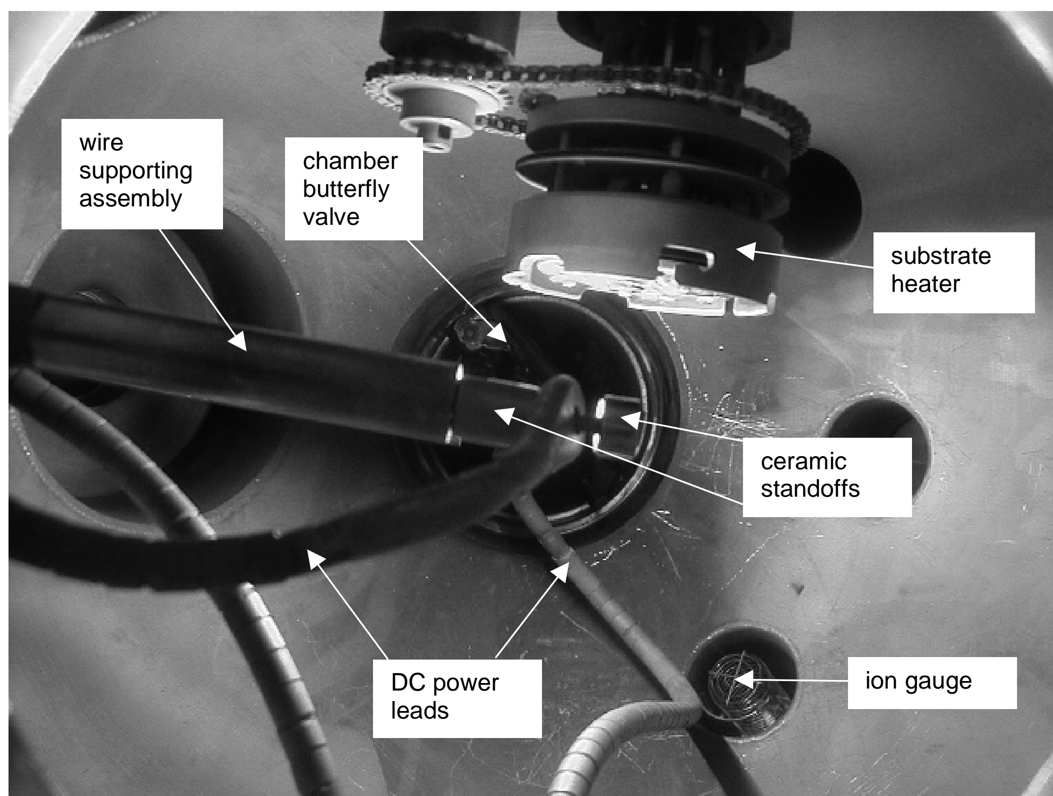

Figure A.3: Top view of the inside of the HWCVD reactor. The wire is on and is normal to the plane of the photograph.

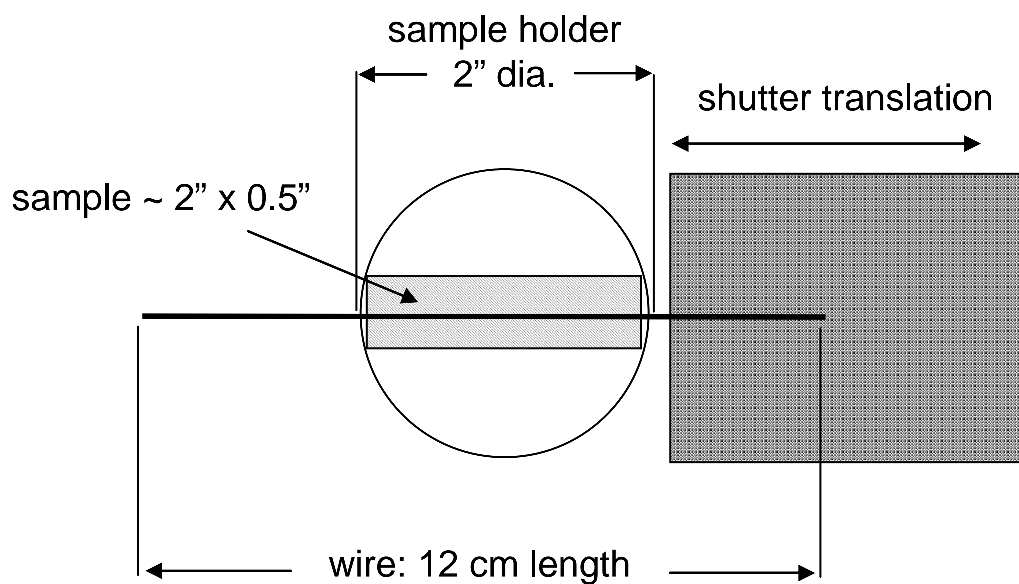

Figure A.4: Schematic of the inside of the HWCVD reactor during growth experiments.

Appendix B

Nucleation Model Code

The following MATLAB functions were used for the nucleation model in Chapter 3.

Function “mysimB” is the main program for solving the system of coupled differential equations. It calls function “myodeB” which finds the time derivative of the system state given by the number of monomers n_1, critical clusters n_x and fractional surface coverage Z. By guessing values for D_0 and E_a and plotting the results against the data the best fit for the family of curves can be found. Relative stay times under various etching conditions can be found by changing the value of τ_a and looking for the best fit to the data.

```
global R ta tn k T D sigma_x Na N0 C_i beta E_i sigma_i i;

bj_values = [0 1 3 5 7 9 12 14 16 18];
C_values = [1 3 2 3 6 6 1];

i=1;
%R=6*10^13; too high
R=5*10^(10);
ta=2.5e-5;
% tn = 3.9486*10^(-8); eliminate this term from model
k = 8.62*10^(-5); %ev/K boltzmann constant
T = 573;% T in K
D0 = 1*10^(-1); %diffusion prefactor Si on Si = 10^(-3)
D = D0*exp(-0.42/(k*T)); %diffusion constant
sigma_x = 5;
sigma_i = 2;
Na = 10^15;
N0 = 10^15;
B_i = bj_values(i);
E_b = 1.55; %ev bond energy

if i<8
   C_i = C_values(i);
else
   C_i = 1;   % don't know what C_i should be for high values of i
end;

E_i = B_i*E_b;
beta = 1/(k*T);
gamma_i = C_i*(N0^(1-i))*exp(beta*E_i);

ta2 = 10^(4);   % time for a 2-cluster to break apart

[t,state]=ode23t('myodeB',[0 10000],[0 0 0 0]');

n1 = state(:,1);
nx = state(:,2);
Z = state(:,3);
```

```
nxwx = state(:,4);

figure(1);
plot(t,n1);
xlabel('t');
ylabel('n_1');

figure(2);
plot(t,nx);
xlabel('t');
ylabel('n_x');

figure(3);
plot(t,Z);
xlabel('t');
ylabel('Z');

figure(4);
plot(t,nxwx);
xlabel('t');
ylabel('nxwx');
```

```
function [dstate] = myode(t,state);

global R ta tn D sigma_x Na N0 C_i beta k T E_i sigma_i i;

%if t < 200
  ta = 2.5e-5;
  %elseif t > 250
  %ta = 2500;
  %else
  %ta = (2.5e-5) + (2500 - 2.5e-5)*(t - 200)/50;
  %end;

n1 = state(1);

nx = state(2);

Z = state(3);

nxwx = state(4);

Z = min(Z,1);  % can't have Z>1

dnxwxdt = (n1.*sigma_i.*D.*n1) + (n1.*sigma_x.*D.*nx) + R.*Z;

dn1dt = R - n1./ta - 2.*(n1.*sigma_i.*D.*n1) - (n1.*sigma_x.*D.*nx) - (R.*Z);

dZdt = (1./Na) .* dnxwxdt;

dnxdt = (n1.*sigma_i.*D.*n1) - 2.*nx.*dZdt;

dstate = [dn1dt dnxdt dZdt dnxwxdt]';
```

Appendix C

Hydrogen Surface Coverage Model Code

The following Mathematica function was used to model the hydrogen surface coverage under HWCVD conditions using the equations in Chapter 4. It finds the equilibrium surface coverage under HWCVD conditions considering absorption, abstraction and thermal desorption rates, and determines the number of oxygen atoms per monolayer of silicon deposition by starting the hydrogen coverage at its equilibrium value when no hydrogen flux is present and finding the subsequent surface coverage, silicon deposited and oxygen deposited as a function of time.

```
Tsub = 711;
Twire = 2073;
theta0 = 0.3744;

R = 70;

Ptot = 75 * 10^(-3);

PSiH4 = Ptot / (R+25);

PSiH4inHe = 25 * PSiH4;

PHe = PSiH4 * 24;

PH2 = Ptot - PSiH4inHe;

O2flux = 2.558 * 10^(13) * N[Sqrt[573/Tsub]];

NN = 6.8*10^14;

PstickH = 0.6 * Exp[-6.94 * 10^(-22) / (k * Tsub)];
Pabs = 0.52 * Exp [-1.39 * 10^(-20) / (k * Tsub)];
PstickO = 0.01;

h = 6.626 * 10^(-34);
c = 3 * 10^10;
k = 1.38 * 10^(-23);
epsilon1 = 6.0 * 4184 / (6.022 * 10^23);
epsilon2 = 19 * 4184 / (6.022 * 10^23);
nua = 2 * 10^(15);
Ea = 57.2 * 4184 / (6.022 * 10^23);
nub = 3.2 * 10^(13);
Eb = 43 * 4184 / (6.022 * 10^23);

mh = 1.7 * 10^(-27);
dh = 1.06 * 10^(-10);
dHe = 0.62 * 10^(-10);
mHe = 4 * 1.7 * 10^(-27);
```

```
dsi = 2.2 * 10^(-10);

rwire = .025;
dwsub = 2.5;

Fluxatwire = (PH2 * 133 * 0.14) / (100^2 * Sqrt [2 * Pi * mh * k * Twire]);

Fluxnocoll = Fluxatwire * rwire / dwsub;

fluxin = Fluxnocoll;

FluxSiH4wire = (PSiH4 * 133 * 0.7) / (100^2 * Sqrt [2 * Pi * 28 * mh * k *
Twire]);

FluxncSiH4 = FluxSiH4wire * rwire / dwsub;

fluxinSi = FluxncSiH4;

Fluxratio = (fluxin + fluxinSi) / fluxinSi;

T = Tsub;

Print["T = ",Tsub];
Print["Ptot = ",Ptot];
Print["R = ",R];
Print["PSiH4 in He = ",PSiH4inHe];
Print["PSiH4 = ",PSiH4];
Print["PH2 = ",PH2];
Print["fluxin = ", fluxin];
Print["flux silicon in = ",fluxinSi];

Print["flux ratio = ", Fluxratio];

Q10 = Exp[-h*c*(2093)/2/k/T] * Exp[-h*c*(621)/2/k/T] / (1 - Exp[-h*c*(2093)/k/T]
) / (1 - Exp[-h*c*(621)/k/T]);
Q11 = Exp[-h*c*(2088)/2/k/T] * Exp[-h*c*(2099)/2/k/T] / (1 - Exp[-h*c*(2088)/k/T
]) / (1 - Exp[-h*c* (2099)/k/T]);
Q2  = Exp[-h*c*(637)/2/k/T] * Exp[-h*c*(2091)/2/k/T] * \
      Exp[-h*c*(2104)/2/k/T] * Exp[-h*c*(910)/2/k/T] / (1 - Exp[-h*c*(637)/k/T])
```

```
 / (1 - Exp[-h*c*(2091)/k/T]) / (1 - Exp[-h*c*(2104)/k/T]) / (1 - Exp[-h*c* (910
)/k/T]);


VerboseDthetadt[Theta_] :=Module[{theta00,theta10,theta11,theta2,eqn3,sol3,theta
11A,theta11B,eqn4,eqn4A,eqn4B,sol4A,sol4B,sols,solns,realsolns,n,t10,t11,t00,t2,
dThetadtdes,dThetadtads,dThetadtabs,dThetadt},
theta00 = 1 - theta10 - theta11 - theta2;
theta10 = 2 (Theta - theta11 - 2 theta2);
eqn3 = {theta10^2 / theta00 / theta11 == 4 Q10^2 / \
             Q11 * Exp[-epsilon1/k/T]};
sol3 = Solve[eqn3,theta11];
theta11A = Expand[theta11 /. sol3[[1]]];
theta11B = Expand[theta11 /. sol3[[2]]];
eqn4 = {theta10^2 theta2^2 / theta11^3 / (1 + theta2) == \
   Q10^2 Q2^2 / Q11^3 Exp[- 2 epsilon2 / (2 k T)]};
eqn4A = eqn4 /. {theta11 -> theta11A};
eqn4B = eqn4 /. {theta11 -> theta11B};
sol4A = Solve[eqn4A,theta2];
sol4B = Solve[eqn4B,theta2];
sols={};
For[n=1, n<=Length[sol4A], n++,sols= Append[sols, Union[sol3[[1]] /. sol4A[[n]],
sol4A[[n]]]]];
For[n=1, n<=Length[sol4B], n++,sols= Append[sols, Union[sol3[[2]] /. sol4B[[n]],
sol4B[[n]]]]];
solns = {theta00, theta10, theta11, theta2} /. sols;
realsolns = solns;
realsolns = Select[realsolns, Im[#[[1]]]==0 & ];
realsolns = Select[realsolns, Im[#[[2]]]==0 & ];
realsolns = Select[realsolns, Im[#[[3]]]==0 & ];
realsolns = Select[realsolns, Im[#[[4]]]==0 & ];
realsolns = Select[realsolns, Re[#[[1]]]>0 & ];
realsolns = Select[realsolns, Re[#[[2]]]>0 & ];
realsolns = Select[realsolns, Re[#[[3]]]>0 & ];
realsolns = Select[realsolns, Re[#[[4]]]>0 & ];
Print["Theta = ",Theta];
Print[realsolns];
If[Length[realsolns]>0,
        t00 = realsolns[[1]][[1]];
```

```
        t10 = realsolns[[1]][[2]];
        t11 = realsolns[[1]][[3]];
        t2 = realsolns[[1]][[4]];
        dThetadtdes = (-nua*t11*Exp[-Ea/k/T] - nub*t2^2*Exp[-Eb/k/T]);
        Print["dTheta/dt (desorption) = ",dThetadtdes];
        dThetadtads = fluxin * PstickH * (2 - Theta) / 2 / NN;
        Print["dTheta/dt (adsorption) = ",dThetadtads];
        dThetadtabs = - fluxin * Pabs * (Theta) / 2 / NN;
        Print["dTheta/dt (abstraction) = ",dThetadtabs];
        dThetadt = dThetadtdes + dThetadtads + dThetadtabs;
        Print["dTheta/dt = ",dThetadt];
        dThetadt,0]];

Dthetadt[Theta_] :=Module[{theta00,theta10,theta11,theta2,eqn3,sol3,theta11A,the
ta11B,eqn4,eqn4A,eqn4B,sol4A,sol4B,sols,solns,realsolns,n,t10,t11,t00,t2,dThetad
tdes,dThetadtads,dThetadtabs,dThetadt},
theta00 = 1 - theta10 - theta11 - theta2;
theta10 = 2 (Theta - theta11 - 2 theta2);
eqn3 = {theta10^2 / theta00 / theta11 == 4 Q10^2 / \
             Q11 * Exp[-epsilon1/k/T]};
sol3 = Solve[eqn3,theta11];
theta11A = Expand[theta11 /. sol3[[1]]];
theta11B = Expand[theta11 /. sol3[[2]]];
eqn4 = {theta10^2 theta2^2 / theta11^3 / (1 + theta2) == \
   Q10^2 Q2^2 / Q11^3 Exp[- 2 epsilon2 / (2 k T)]};
eqn4A = eqn4 /. {theta11 -> theta11A};
eqn4B = eqn4 /. {theta11 -> theta11B};
sol4A = Solve[eqn4A,theta2];
sol4B = Solve[eqn4B,theta2];
sols={};
For[n=1, n<=Length[sol4A], n++,sols= Append[sols, Union[sol3[[1]] /. sol4A[[n]],
sol4A[[n]]]]];
For[n=1, n<=Length[sol4B], n++,sols= Append[sols, Union[sol3[[2]] /. sol4B[[n]],
sol4B[[n]]]]];
solns = {theta00, theta10, theta11, theta2} /. sols;
realsolns = solns;
realsolns = Select[realsolns, Im[#[[1]]]==0 & ];
realsolns = Select[realsolns, Im[#[[2]]]==0 & ];
realsolns = Select[realsolns, Im[#[[3]]]==0 & ];
```

```
realsolns = Select[realsolns, Im[#[[4]]]==0 & ];
realsolns = Select[realsolns, Re[#[[1]]]>0 & ];
realsolns = Select[realsolns, Re[#[[2]]]>0 & ];
realsolns = Select[realsolns, Re[#[[3]]]>0 & ];
realsolns = Select[realsolns, Re[#[[4]]]>0 & ];
If[Length[realsolns]>0,
        t00 = realsolns[[1]][[1]];
        t10 = realsolns[[1]][[2]];
        t11 = realsolns[[1]][[3]];
        t2 = realsolns[[1]][[4]];
        dThetadtdes = (-nua*t11*Exp[-Ea/k/T] - nub*t2^2*Exp[-Eb/k/T]);
        dThetadtads = fluxin * PstickH * (2 - Theta) / 2 / NN;
        dThetadtabs = - fluxin * Pabs * (Theta) / 2 / NN;
        dThetadt = dThetadtdes + dThetadtads + dThetadtabs;
        dThetadt = N[dThetadt];
        ClearAll[theta00,theta10,theta11,theta2];
        dThetadt,0]];

ClearAll[theta];
theta = theta0;
Odeposit = 0;
Sideposit = 0;
stepsize = 0.002;
dthdt = 9999;
n = 0;
While[Sideposit<6.8*10^14,
    t = n*stepsize;
    Print["t = ",n*stepsize];
    Print["theta = ",theta];
    Print["deposited Oxygen atoms = ",Odeposit];
    Print["deposited Silicon atoms = ",Sideposit];
    If[Abs[dthdt]>10^(-7),dthdt = Dthetadt[theta],dthdt=0];
    Print["Dtheta/Dt = ",dthdt];
    Print[];
    theta = theta + dthdt * stepsize;
    Odeposit = Odeposit + O2flux * (2 - theta) * PstickO * stepsize;
    Sideposit = Sideposit + fluxinSi * stepsize;
    n=n+1];
```